APPLICATION OF X-RAY ABSORPTION

SPECTROSCOPY AND MOLECULAR SIMULATION TO

STUDY THE SOLVATION STRUCTURE OF

POLYMER:KSCN ELECTROLYTES

Jittima Chaodamrongsakul

A Thesis Submitted in Partial Fulfillment of the Requirements for the

Degree of Doctor of Philosophy in Chemistry

Suranaree University of Technology

Academic Year 2011

การประยุกต์สเปกโตรสโกปีการดูดกลืนรังสีเอ็กซ์และการจำลองโมเลกุลเพื่อศึกษาโครงสร้างการจัดเรียงตัวระบบพอลิเมอร์:
โพแทสเซียมไทโอไซยาเนตอิเล็กโทรไลต์

นางสาวจิตติมา เชาว์ดำรงสกุล

วิทยานิพนธ์นี้เป็นส่วนหนึ่งของการศึกษาตามหลักสูตรปริญญาวิทยาศาสตรดุษฎีบัณฑิต
สาขาวิชาเคมี
มหาวิทยาลัยเทคโนโลยีสุรนารี
ปีการศึกษา 2554

APPLICATION OF X-RAY ABSORPTION

SPECTROSCOPY AND MOLECULAR SIMULATION TO

STUDY THE SOLVATION STRUCTURE OF

POLYMER:KSCN ELECTROLYTES

Suranaree University of Technology has approved this thesis submitted in partial fulfillment of the requirements for the Degree of Doctor of Philosophy.

Thesis Examining Committee

_____

(Asst. Prof. Dr. Kunwadee Rangsriwatananon)

Chairperson

_____

(Asst. Prof. Dr. Visit Vao-Soongnern)

Member (Thesis Advisor)

_____
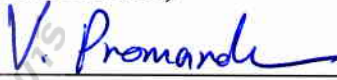
(Assoc. Prof. Dr. Vinich Promarak)

Member

_____
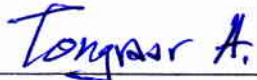
(Assoc. Prof. Dr. Anan Tongraar)

Member

_____

(Dr. Wantana Klysubun)

Member

_____

_____

(Prof. Dr. Sukit Limpijumnong)　　(Assoc. Prof. Dr. Prapun Manyum)

Vice Rector for Academic Affairs　　Dean of Institute of Science

จิตติมา เชาว์ดำรงสกุล : การประยุกต์สเปกโตรสโกปีการดูดกลืนรังสีเอ็กซ์และการจำลอง
โมเลกุลเพื่อศึกษาโครงสร้างการจัดเรียงตัวระบบพอลิเมอร์:โพแทสเซียมไทโอไซยาเนต
อิเล็กโทรไลต์ (APPLICATION OF X-RAY ABSORPTION SPECTROSCOPY AND
MOLECULAR SIMULATION TO STUDY THE SOLVATION STRUCTURE OF
POLYMER:KSCN ELECTROLYTES) อาจารย์ที่ปรึกษา : ผู้ช่วยศาสตราจารย์ ดร.วิสิษฐ์
แววสูงเนิน, 199 หน้า.

วัตถุประสงค์ของวิทยานิพนธ์นี้คือการศึกษาผลของชนิดโฮสต์พอลิเมอร์ที่มีต่อโครงสร้าง
การจัดเรียงตัวของไอออน K^+ ในสารประกอบเชิงซ้อน TET:KSCN PPG:KSCN และ PVA:KSCN
ด้วยเทคนิคทางการทดลองและโมเลกูลาร์ไดนามิกส์ (MD) การจำลองด้วยเทคนิค MD โดยใช้
COMPASS forcefield เพื่อคำนวณ Radial Distribution Function (RDF) และโครงสร้างระดับ
อะตอมที่ 300 เคลวิน สมบัติทางโครงสร้างที่ได้จากการจำลองด้วยเทคนิค MD พบว่าสอดคล้องเป็น
อย่างดีกับผลการศึกษาที่มีรายงานไว้แล้ว โครงสร้างการจัดเรียงตัวที่จำลองได้นำมาใช้คำนวณสเปก
ตรา MD-EXAFS สำหรับระบบ K^+ ในน้ำ PVA TET และ PPG สเปกตรา MD-EXAFS ที่คำนวณ
ได้นำมาเปรียบเทียบกับสเปกตราที่ได้จากการทดลอง โดยการเปรียบเทียบสเปกตราดังกล่าวพบว่าส
เปกตราจากการจำลองแบบโมเลกูลาร์ไดนามิกส์สอดคล้องกับสเปกตราที่ได้จากการทดลอง ดังนั้น
สามารถเสนอได้ว่าการจำลองแบบโมเลกูลาร์ไดนามิกส์ด้วย empirical forcefield เป็นเทคนิคที่เป็น
ประโยชน์ในการศึกษาโครงสร้างระดับอะตอมของสารละลายน้ำไอออนิก และสารประกอบที่เป็น
ตัวแทนของพอลิเมอร์อิเล็กโทรไลต์

การศึกษาสมบัติเชิงโครงสร้าง และเชิงพลวัตของระบบ bidisperse พอลิเอทิลีนออกไซด์
(PEO) ด้วยเทคนิค Monte Carlo (MC) โดยใช้แบบจำลองโมเลกุลพอลิเมอร์บนโครงผลึกที่มีเลขโค
ออร์ดิเนชันสูงที่ 373 เคลวิน พบว่า PEO สอดคล้องกับ universal scaling law และการเติมสายโซ่
ขนาดเล็กทำให้การเคลื่อนที่ของพอลิเมอร์เพิ่มขึ้น เนื่องจากสายโซ่ขนาดเล็กลดข้อจำกัดเชิงพลวัตที่
มีต่อสายโซ่ขนาดใหญ่ ทำให้สายโซ่ขนาดใหญ่เคลื่อนที่และคลายตัวเร็วขึ้น

สาขาวิชาเคมี	ลายมือชื่อนักศึกษา _____
ปีการศึกษา 2554	ลายมือชื่ออาจารย์ที่ปรึกษา _____
	ลายมือชื่ออาจารย์ที่ปรึกษาร่วม _____
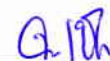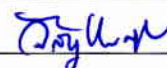
JITTIMA CHAODAMRONGSAKUL : APPLICATION OF X-RAY
ABSORPTION SPECTROSCOPY AND MOLECULAR SIMULATION TO
STUDY THE SOLVATION STRUCTURE OF POLYMER:KSCN
ELECTROLYTES THESIS ADVISOR : ASST. PROF. VISIT
VAO-SOONGNERN, Ph.D. 199 PP.

POLYMER ELECTROLYTES/PEG/PPG/PVA/EXAFS/MOLECULAR
DYNAMICS SIMULATIONS

The objective of this thesis is to study the effect of host polymer type on the
solvation structure of K^+ ion in Tetraglyme:KSCN (TET:KSCN), Poly(propylene
glycol):KSCN (PPG:KSCN) and Poly(vinyl alcohol):KSCN (PVA:KSCN) complexes
by experimental and Molecular Dynamics (MD) simulation technique. The MD
simulations with COMPASS forcefield were used to calculate the Radial Distribution
Function (RDF) and local atomistic structure at 300 K. Those structural properties
obtained from the MD simulations are found to be in very good agreement with other
previous work. The simulated solvation structures were used to compute the MD-
EXAFS spectra for K^+ ions in water, PVA, TET and PPG. MD-EXAFS spectra
generated from MD simulations were then compared with the measured spectra.
Comparison shows the consistence between the EXAFS spectra from MD simulations
and those from the experiments. Thus, we suggest that MD simulation with empirical
forcefield is a useful technique to study the local solvation structures of ionic aqueous
solutions and model compounds representing polymer electrolytes.

The static and dynamics properties of bidisperse PEO were investigated by a Monte Carlo (MC) method of a coarse-grained polymer model on a high coordination lattice at 373 K. In all systems, PEO were satisfied with a universal scaling law. The results revealed that insertion of short chains (bidisperse) cause the mobility of the polymer chain to increase, due to the short chains reducing the dynamic constraint on the long chain and inducing the long chain to move and relax faster.
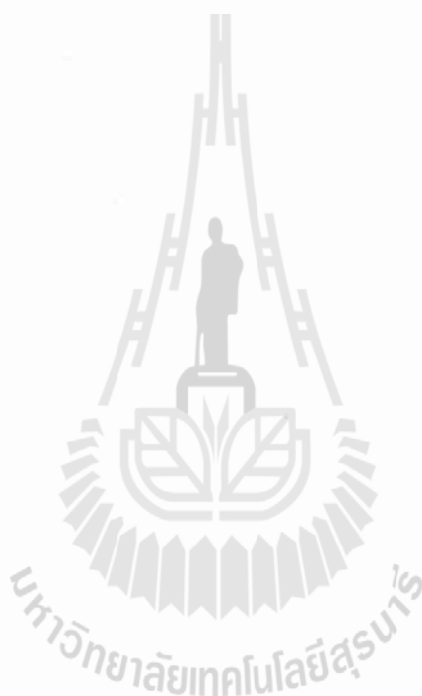
School of Chemistry

Academic Year 2011

Student's Signature _____

Advisor's Signature _____

Co-Advisor's Signature _____

ACKNOWLEDGMENTS

CONTENTS

CONTENTS (Continued)

CONTENTS (Continued)

LIST OF TABLES

LIST OF TABLES (Continued)

LIST OF FIGURES

LIST OF FIGURES (Continued)

LIST OF FIGURES (Continued)

LIST OF FIGURES (Continued)

LIST OF FIGURES (Continued)

LIST OF FIGURES (Continued)

LIST OF ABBREVIATIONS

Å	Angstrom
Å^{-1}	per Angstrom
COMPASS	Condensed-phase Optimized Molecular Potentials for Atomistic Simulation Studies
CPU	Central Processing Unit
℃	Degree Celcius
D	diffusion coefficient
E	Potential energy
eV	Electron volt
EXAFS	Extended X-ray Absorption Fine Structure
et al.	et alia (and other)
g/mol	gram per mole
g(r)	Pair Distribution Function
KSCN	Potassium thiocyanate
K^{+}	Potassium ion
K	Degree Kelvin
kJ/mol	kiloJoule per mole
LJ	Lennard-Jones
MW	Molecular Weight
MD	Molecular Dynamics
MM	Molecular Mechanics

LIST OF ABBREVIATIONS (Continued)

MSD	Mean Square Displacement
MC	Monte Carlo
N	Coordination number
nm	nanometer
PEG	Poly(ethylene glycol)
PPG	Poly(propylene glycol)
PVA	Poly(vinyl alcohol)
RIS	Rotation isomeric state
RDF, g(r)	Radial Distribution Function
S/cm	Siemen per centimeter
SNND, 2nnd	Second Nearest Neighbor Diamond
SCN^-	Thiocyanate ion
TET	tetraethylene glycol dimethly ether
XRD	X-ray diffraction
μ	Absorption Coefficient
σ^2	Debye-Waller Factors

CHAPTER I

INTRODUCTION

Energy is crucial to many aspects of our life. Energy generation and storage are growing topics in the field of academic research and industrial applications due to the rapidly growing energy demand of the modern world. There are many different forms of energy sources which can be classified to the following categories:

- **Fossil fuels**: defined as fuel formed from the organic remains of prehistoric plants and animals, such as coal, natural gas and oil.

- **Renewable energy**: given that fossil fuels are not renewable sources of energy, there is increasing interest in the generation of energy from renewable resources, such as solar, water, wind and wave power or from renewable bio-materials.

- **Nuclear power**: a type of nuclear technology used to generate energy through nuclear fission.

Many renewable energy sources (e.g., solar and wind) are characterized by periods of production (e.g., daylight and blowing winds, respectively) followed by non-production (e.g., night and no wind, respectively). Hence, *energy storage* is a key to making energy continuously available, as well as in many cases making energy portable (e.g., for electric or hybrid vehicles). A battery is a device used to store energy in an electrochemical form. Every battery has a positive electrode (cathode) and a negative electrode (anode), which are immersed in a solid or liquid electrolyte.

and a negative electrode (anode), which are immersed in a solid or liquid electrolyte. All materials are enclosed in a container with a separator between the electrodes to keep them apart. Batteries are usually divided into two main classes: Primary batteries (disposable batteries which are intended to be used once and discarded) and secondary batteries (rechargeable batteries which can be recharged by applying electrical current).

Polymers are widely studied due to their significant potential as Solid Polymer Electrolytes (SPEs) for an application as a medium in rechargeable batteries. In 1975, Wright (Bruce, 1995) first reported that SPEs exhibit significant ionic conductivity. The potential use of SPEs in batteries applications was first suggested by Armand *et al.* (Preechatiwong and Schultz, 1996) in 1979. SPEs consist of salts dissolved in solid high molecular weight polymer. These compounds are solid state coordination compounds and as such sit between coordination chemistry and conventional solid state chemistry. Polymer, which can dissolve salt must be comprised of O, N or S atoms because these atoms can interact with cation, and make decompositive salt to have a better ionic conductivity. A considerable scientific effort has been dedicated to exploring and understanding the characteristics of these electrolyte systems. Many investigations have focused on developing SPEs with high ionic conductivities (10^{-3} S/cm or higher) at ambient temperature (Chintapalli, 1996). In majority of reported system, an alkaline metal salt is solubilized in polymer, generally through complex formation with the ion-chelating monomer unit or with pendant moieties of the macromolecule.

The important criteria for a polymer to act as a host for complex formation include: (Mendolia, 1995)

(i)   Having atom or groups of atom with sufficient donor ability to coordinate cation.

(ii)   Low bond rotation energy barriers to facilitate polymers segmental motion.

(iii)   A suitable distance between coordinating heteroatoms allowing interaction with the ions.

Poly(ethylene oxide) (PEO) is the most interesting base material because of its high chemical and thermal stability. The chemical structure of PEO consists of series of polyethers ($[-(OCH_2CH_2)_n-]$). PEO is a semicrystalline polymer, possesing both an amorphous and a crystalline phase at room temperature. It can also solvate a wide variety of salts, even at very high salt concentration (Bruce, 1995; Preechatiwong and Schultz, 1996; Chintapalli, 1996; Mendolia, 1995; Johansson; Quartarone *et al.*, 1998; Song *et al.*, 1999; Dias *et al.*, 2000; Chandra and Chandra, 1994; Bernson *et al.*, 1995; Xu *et al.*, 1996; Rhodes and Frech, 2001). The solvation of salt occurs through the association of the metallic cation with the oxygen atom in the backbone (Figure 1.1). Because pure PEO is a semicrystalline polymer, significant ionic transport occurs only within the amorphous phase. This feature explains the dramatic decrease in ionic conductivity seen in many PEO-based systems for temperature below the melting point of pure crystalline PEO ($T_m \sim 66$ °C); the crystalline PEO regions are non-conductive and serve to hinder bulk ionic transport. Clearly, the inherent crystallinity of PEO is not very attractive for applications in solid electrolytes.
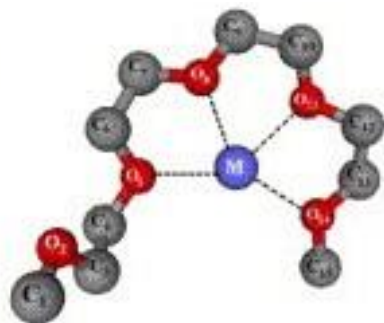
Figure 1.1 Solvation of M (M=Na$^+$ and K$^+$) by CH$_3$O(CH$_2$CH$_2$O)$_4$CH$_3$ chain. Hydrogens are omitted for clarity (Dhumal and Gejji, 2006).

Low molecular weight oligomers analogous to PEO have also been widely used to model PEO-salt complex in experimental and simulation studies. Oligomers more easily adopt a fully amorphous state at accessible temperatures, so single phase systems can be more easily prepared and analyzed. Among those, glymes (define as CH$_3$O(CH$_2$CH$_2$O)$_n$CH$_3$, n = 2-4) have been extensively used in spectroscopic studies by Frech and Huang (1994) and Rhodes and Frech (1999). A detailed spectroscopic study of CH$_2$ rocking region of glyme complex with salt suggests that the interaction of the cation with the ether oxygens occurs with the glyme adopting a conformation which is energetically unfavorable in the pure glyme. For the first step to understanding the local structures, glyme-salt complex can be used as the model of PEO-salt complex.

Many investigations have focused primarily on an enhancement of the room temperature conductivity via various approaches such as using blends, copolymers, comb branch polymers and cross-linked "network". All these enhancements have been done reducing the crystalline order, trying to create an amorphous phase or decreasing the glass-transition temperature (Chintapalli, 1996; Quartarone *et al.*,

1998; Dias *et al.*, 2000). Poly(propylene oxide), PPO would, in theory, appear to be an ideal candidate as a stable, amorphous host polymer. The random arrangement of methyl groups along the chain (Figure 1.2) prevents the polymer from crystallizing (Rhodes and Frech, 1999; Acosta and Morales, 1996). Acosta and Morales (1996) improved the ionic conductivity by synthesizing different polymer electrolytes based on PEO/PPO blends. They analyzed the effect of lithium salt on the microstructure and electrical conductivity. It was found that the conductivity was lower for the highest salt concentration than for the minimum salt concentration. Decha (2002) improved the ionic conductivity of PEO based electrolytes by adding PPO to increase the fraction of the conductive amorphous phase. The results from XRD, DSC, FTIR and high resistance meter suggested that PPO was able to decrease the crystallinity of PEO and improve the ionic conductivity of PEO-salts (LiCF$_3$SO$_3$ or KSCN) electrolytes.
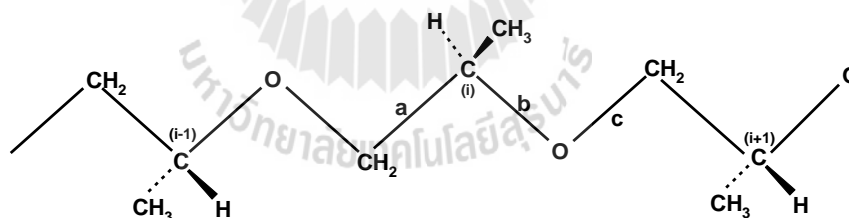
Figure 1.2 Schematic diagram of the isotactic poly(propylene oxide) chain in its planar, all-trans conformation.

In the recent years, extensive research efforts have been devoted to the development of amorphous polymeric materials with high ionic conductivity at room temperature as well as good mechanical, optical and thermal properties. The electrical and optical properties of the polymers can be suitably modified by the addition of

dopants depending on their reactivity with the host matrix. Although a PEO-based electrolyte can form a dimensionally stable film, its ambient temperature conductivity is only in the range of 10^{-7} to 10^{-8} S cm^{-1}. This is too low for application in electrochemical devices. Poly(vinyl alcohol) (PVA) is one of the most important polymeric materials as it has many applications in industry and is of relatively low cost. Most of the commercial PVA samples have been prepared by hydrolyzing the poly(vinyl acetate). Due to the presence of hydroxyl group, the hydrogen bond between the interchains of the PVA has been developed. This causes the high melting point and good mechanical stability of PVA. The electrical conductivity of the PVA blend with inorganic acids and water has been already reported by Vargas *et al.* (Vargas *et al.*, 2001). It is reported that the water content in the PVA based electrolyte enhanced the conductivity while preserving the dimensional stability of the electrolyte. In PVA-KOH systems (Mohamad *et al.*, 2003; Yang, 2004) possessing a conductivity level of 10^{-2} - 10^{-4} Scm^{-1} at room temperature, which highly depends on the composition of the electrolyte, has been prepared. XRD analysis reveals that KOH disrupts the crystalline nature of PVA-based polymer electrolytes and converts them to an amorphous phase, which enhances the ionic conductivity of PVA electrolyte.

It is clear that PEO is able to solvate a wide range of metal salts, including alkali metals, alkaline earth metals and transition metals. The different of salt influence the electrolyte properties. For most polymer-salt complexes, cations should bind to the polymer chain instead of other ions. Also, to freely move in the polymer matrix, anions should have minimal interaction with the polymer and the cations. For satisfy weak anion-cation interaction and strong cation-polymer bonding, it is better to use salt with a small univalent cation and a large anion such as potassium thiocyanate

(KSCN). In this work, KSCN salt is more interesting because SCN^- has two possible donor atoms (S and N) to interaction with K^+ cation and PEO ether oxygen.

Various methods have been employed to determine the structure of PEO-salt electrolytes. These include differential scanning calorimetry (DSC), X-ray diffraction spectroscopy and X-ray absorption fine structure spectroscopy (XAFS) and vibrational spectroscopic methods such as infrared and Raman spectroscopy. Ultimately, the objective is to understand how the structure (macroscopic and molecular) of polymer electrolytes is related to its behavior particularly in terms of ionic conductivity.

Thermal behavior of PEO-salt complexes can be better understood by characterization of the crystalline and amorphous phase present in the complexes by using differential scanning calorimeter (DSC). The DSC thermograms of the PEO-salt complex give information on melting temperature (T_m), enthalpy of melting (ΔH) and percentage of crystallinity. From our previous work (Chaodamrongsakul, 2003) on PEO:KSCN complex, it is indicated that when salt concentration increases, the percentage of crystallinity decrease and the ionic conductivity increase.

When salt is dissolved into PEO and dissociated to ions, it generates carrier ions. The ionic conductivity should increase with salt concentration, if all dissolved species carry charge at the same rate as at lower concentrations. However, this is not true in SPEs as increasing the charge species may result in the presence of ion pair, triplets, or even higher degrees of association. The ionic transport in SPEs is strongly related to the cation-ether oxygen coordination bonds (the stronger are these interactions, the lower is the cation mobility) and to the freedom of polymer chains movements and to their rearrangements. Local relaxation and sequential motions of

polymer host chains become essential to high ionic conductivity. Supporting evidence for ion association has been provided by vibrational spectroscopy studies. Different ionic species have been spectroscopically distinguished in polymer-salt system. For example, Rhodes and Frech (2001) used Raman and infrared spectroscopy to monitor ion association in $P(EO)_6:LiAsF_6$. Zhang *et al.* (2003) used FTIR to investigate ion association in PEO:MSCN (M = Na, K) system. They found that the complex of K^+ and PEO seems to cause the transformation of PEO from crystalline to amorphous phase. Additionally, IR and Raman have aided understanding of the polymer structure, interaction of the ions with the polymer, as well as ion-ion interactions. Based on the vibrational spectroscopic study on the *gauche* and *trans* forms and its application to PEO by Davison (Davison, 1955) and Shriver *et al.* (Papke *et al.*, 1981). They were able to assign *gauche* configuration for the $O-CH_2CH_2-O$ group in PEO-alkali metal salt complexes. This was arrived at by the assignment of bands in the 800-1000 cm^{-1} region. Further, evidence for cation-ether oxygen coordination was obtained by the broadening of the C-O-C stretch (1150 cm^{-1}) observed in PEO and its movement to lower frequencies upon complexation. Also, Raman vibrational band at 865 cm^{-1} for PEO:NaSCN complex (and related compounds) in view of its relationship with Raman spectra for number of crown-ether complexes (Sato, 1978) was taken as evidence for a metal-oxygen stretching and it was suggested that PEO helix wraps around the metal ion.

Early attempts at determining the X-ray structures of some PEO-metal salt complexes have been hampered because of the difficulty of the single crystal method. However, these efforts have results in the elucidation of X-ray structures, of $PEO_3:NaClO_4$ (Lightfoot *et al.*, 1992), $PEO_3:LiCF_3SO_3$ (Lightfoot *et al.*, 1993),

PEO$_4$:KSCN and PEO$_4$:NH$_4$SCN (Lightfoot *et al.*, 1994) available from high resolution powder X-ray diffraction data. Contrary to the expectations of Armand (Vashishta, 1979), effective anion-cation separation is not achieved in any of PEO-metal salt complexes in which X-ray structures have been solved. This includes structures with bulky anions such as I$^-$ as in PEO:NaI (Chatani and Okamura, 1987) or structures with bulky and "non-coordinating" anions such as CF$_3$SO$_3^-$ in PEO$_3$:LiCF$_3$SO$_3$ (Lightfoot *et al.*, 1993) or ClO$_4^-$ in PEO$_3$:NaClO$_4$ (Lightfoot *et al.*, 1992). In the PEO:NaI structure, a tight zig-zag chain around cation and anion is seen with a coordination number of two for each ionic species. This chain is wrapped around by the helical PEO structure (Chatani and Okamura, 1987). The oxygen atoms are located in the inner surface of the tunnel cavity so as to provide appropriate coordination environment for the cation inside PEO helix (Figure 1.3).
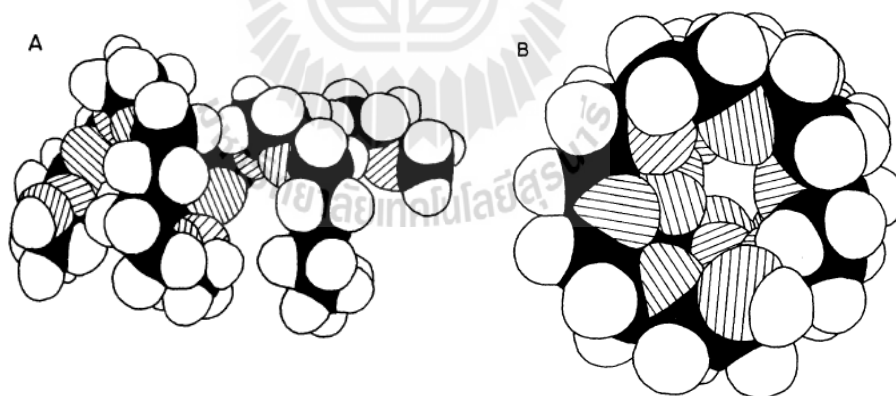
Figure 1.3 Molecular models of poly(ethylene oxide) conformation as proposed for complexation to sodium and lithium cations, (A) side view, (B) end view. Hydrogen atoms are not shaded, carbon atoms are black and oxygen atoms are crosshatched (Chatani and Okamura, 1987).

The X-ray structures of $(PEO)_3:LiCF_3SO_3$ and $(PEO)_4:MSCN$ ($M=K^+$ or NH_4^+) have been determined to a very good degree of accuracy and consequently allow a closer inspection of bond parameters around the cation. In $(PEO)_3:LiCF_3SO_3$ complex, lithium ion is coordinated to five oxygens in an approximate trigonal bipyramidal arrangement. The two axial positions and one equatorial position are taken by oxygens from the PEO chain, while two other equatorial positions are taken by oxygens derived from $CF_3SO_3^-$ anion. The thiocyanide metal salt complexes, $(PEO)_4:KSCN$ and $(PEO)_4:NH_4SCN$ are isostructural (Lightfoot *et al.*, 1994). The coordination number around cation is seven. In these complexes, PEO repeating distance along the axis of helix is shortened leading to eight ethylene oxy units within a shorter fiber axis compared to six found in $(PEO)_3:LiCF_3SO_3$. This probably accounts for the availability of five ether oxygens for coordination to metal ion. Two other coordination positions are taken by nitrogen atoms of the anion. In fact, one nitrogen and two ether oxygens are involved in simultaneous coordination to two cations and act as bridging units (Figure 1.4).
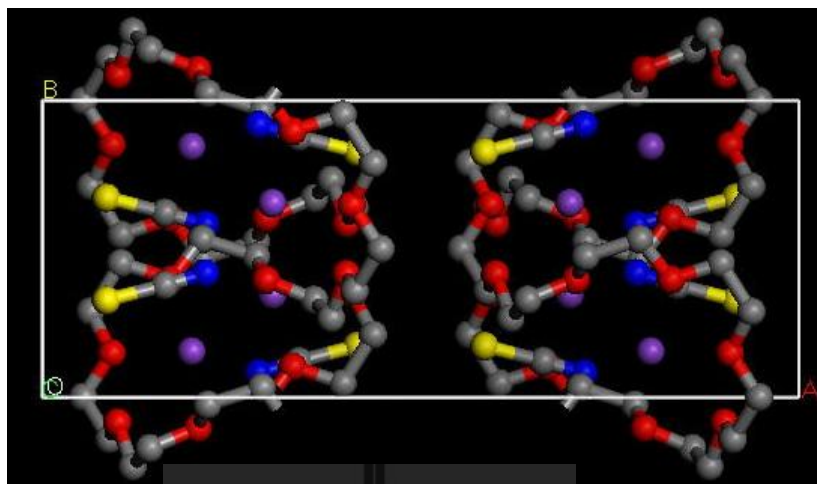
Figure 1.4 View of the structure of the PEO$_4$:KSCN complex. Violet sphere, potassium; dark blue, nitrogen; yellow, sulfur; gray, carbon; red, oxygen (Lightfoot *et al.*, 1994).

Extended X-ray Absorption Fine Structure (EXAFS) and X-ray Absorption Near Edge Structure (XANES) spectroscopy have been used to probe the structure of polymer electrolytes. Unlike X-ray diffraction methods which yield information on crystalline materials, EXAFS can also be used to obtain structural characteristics of amorphous materials. EXAFS data can be interpreted to obtain information about the nearest neighbour atoms around the target element and the distances from the target element to these neighbours, *i.e.* the immediate local environment around the target element. From studies on PEO-divalent metal salt complexes, it is found that the M-O distance is nearly invariant at about 2.1 Å for Co, Ni, Cu and Zn, but is slightly larger for Ca (2.4 Å) (Linford, 1995; Schlindwein *et al.*, 1995; Latham *et al.*, 1993; Bandara *et al.*, 1994; Latham *et al.*, 1989). For high ratios of PEO-metal salt, large coordination numbers for the metal ion are seen. For example, Co^{2+} has a coordination number of six (4 oxygens and 2 Br$^-$) in the PEO$_4$:CoBr$_2$ complex,

whereas, in the analogous $PEO_{15}:CoBr_2$, the coordination reduces to ~ 3. It can be said that increase in tight coordination by neighbours will lead to low ionic conductivity. Thus, the $PEO_n:CaBr_2$ complex which shows high coordination numbers has a low ionic conductivity. Even for most PEO:LiX complexes, high ionic conductivities are observed only at high O/Li ratios. In the complexes $PEO_n:ZnX_2$, when $X = I^-$ or Br^-, the coordination to Zn^{2+} is through four oxygens while when $X = Cl^-$ the coordination number is reduced, showing the effect the anion on the coordination. Thus EXAFS can provide useful information on the local structure around the metal ion even in the amorphous region.

Recently, many papers present an advance in the use of the atomistic molecular dynamic simulations (MD) and EXAFS spectroscopy, which enable us to understand the solvated ions in solution (Dang *et al.*, 2006). A molecular-level is essential to understanding the chemical and physical properties and transport mechanism of ions in solutions. Molecular dynamics (MD) and Monte Carlo (MC) simulation techniques provide a powerful approach to probing such processes in condensed phase environments (Allen, 1987). MD simulations provide a detailed picture of structure and dynamics for complex systems that may not be tractable by other methods. Due to the advance of modern EXAFS algorithms and the availability of more accurate ion and solvent potential models, the number of studies that combine MD with EXAFS has increased considerably (Roccatano *et al.*, 1998; Hoffmann *et al.*, 1999; D'Angelo *et al.*, 1994; D'Angelo *et al.*, 1995; D'Angelo *et al.*, 1996; D'Angelo and Pavel, 1999; Filipponi and Di Cicco, 1995). The accuracy of the existing theoretical models for the interatomic potential in solid and liquid ionic systems was discussed in through direct comparison of EXAFS and MD results

(Andrea Di, 1996; Di Cicco *et al.*, 1997). Moreover, MD simulations can be used to investigate the segmental motion resulting in conformational changes in polymer electrolytes based on PEO.

The physics of polymeric materials has been a problem of considerable interest in recent years (de Gennes, 1979; Doi, 1986; Ferry, 1980; Bird, 1977), In contrast to small molecules, polymeric materials display a rich and unusual viscoelastic behavior for time and distance scales, where ordinary small molecules are still Newtonian (Doi, 1986; Ferry, 1980; Bird, 1977). The reason for this unusual behavior of polymeric materials is that the motion of a polymer is subject to complicated topological constraints. Unlike simple atomic or molecular systems, long chain polymers have to move in specific ways which are limited by the fact that they are connected to other monomers and they cannot cut through each other. It is the main concern of the present work to investigate this motion in detail. Although experiments have been very important in elucidating many of the interesting properties of these complex systems, there remain many unanswered questions. In particular, there has been no experiment up to now which is able to study directly the microscopic origin of the macroscopic effects which are observed. For this reason, computer simulations of bidisperse polymers can play an important role in our understanding of dense polymer dynamics. The aim of such a simulation should be to bridge the gap between experimental and analytical investigations and to provide a direct connection from a microscopic model of the motion to experimentally observable quantities.

Monte Carlo (MC) simulations may provide an alternative choice for the simulation of realistic polymers. Compared with MD, MC is usually a more flexible

algorithm. One can argue that faster motions, such as bond stretching and bending, only serve as the heat bath for the slower motions, such as torsions, which make the torsion dynamics a category of random motion without memory of its past history. Thus, this slower motion can be modeled by a Markovian master equation, which virtually opens the door for the dynamic simulation of realistic polymers via MC algorithms. Indeed, in MD simulations, at the length and time scale where a monomer starts feeling the environment, its motion will be eventually averaged by various encounters with surrounding monomers. This "averaging" process leads to the stochastic nature of chain dynamics, which serves as one of the most important bases of the Rouse theory. The dynamic MC itself is usually built upon this stochastic nature of moves according to the Metropolis criterion, naturally containing the detailed balance principle. As a result, including the bond stretching and bending into MC algorithms is no longer necessary, which greatly saves computing time. Furthermore, excluding bond stretching and bending results in fixed bond length and bond angle, which, combined with the symmetrical torsion angle of many realistic polymers, enables a lattice MC algorithm to use the fast integer computation. The elemental moves of MC can be very flexible for the sake of computing speed.

In 1995, Roland and Mattice (1995) first introduced a new simulation technique for amorphous polymer that employed the modified RIS models of the coarse-grained chains which were mapped onto the *second nearest neighbor diamond* (2nnd) lattice at the bulk density. 2nnd lattice in combination with the short- and long-range interactions is used to simulate high molecular weight polymers at their bulk density. Lin *et al.* (2006) studies chain dynamics of bidisperse (1K/4.5K) polyethylene (PE) melts using 2nnd lattice. They founded that no systematic change

of mean-square radius of gyration as the concentration varies in the mixture and the diffusion coefficients increase with increasing short-chain concentration. Moreover, their simulation can reproduce experimental results from NMR diffusion measurements very well. By appropriately constructing a molecular model for polymer chains, 2nnd lattice simulation is more interest for exploration of the microscopic foundation of entanglement dynamics, because simulation method is based on upon microscopic objects.

In this research work, Tetraglyme:KSCN (TET:KSCN), Poly(propylene glycol):KSCN (PPG:KSCN) and Poly(vinyl alcohol):KSCN (PVA:KSCN) complexes will be characterized by experimental techniques such as FTIR and EXAFS in order to determine the vibrational modes of functional group in polymer chains and the local atomistic structure (*i.e.* the coordination number of ether oxygen around K^+ and the distance between them), respectively. Moreover, MD simulation method will be performed to predict EXAFS spectra of polymer/salt electrolyte. Finally, MC (2nnd lattice) simulation will be employed to study the static and dynamic aspects of bidisperse PEO mixture to see the effect of adding short chains on the change in static and dynamic of PEO molecules.

Research objectives

1. To investigate the effect of host polymer type and salt concentration on the atomic solution structures of ions in TET:KSCN, PPG:KSCN and PVA:KSCN complexes by both experimental and MD simulation techniques.

2. To apply Monte Carlo simulation of coarse-grained polymer model on a high coordination lattice (2nnd) to reveal the underlying features of the physical response of the PEO matrix upon the insertion of low molecular weight PEO.

CHAPTER II

LITERATURE REVIEW

2.1 Solid Polymer Electrolytes

In recent years there has been vigorous research activity in industrial and academic laboratories all over the world on solid materials which possess high ion transport properties (Aono *et al.*, 1994; Owens and Argue, 1967; Takahashi *et al.*, 1972; Tatsumisago *et al.*, 1991). Generally ionic conduction is associated with liquids, either solvents with high dielectric constants or molten salts. However, solids that can function as electrolytes also known as solid ionic conductors, fast ion conductors or solid electrolytes (typical conductivity $10^{-6} \leq \sigma \leq 10^{-1}$ S cm^{-1}) are exciting because of their wide ranging applications such as gas sensors (Nicholson *et al.*, 1992), electrochemical display devices (Bange and Gambke, 1990; Visco *et al.*, 1993) high temperature heating elements (Hagenmuller and Gool, 1978), intercalation electrodes (Vincent *et al.*, 1983), power sources (Gabano, 1983), fuel cells (Rickert, 1978), solid state high energy density batteries (Nicholson *et al.*, 1992; Bonino *et al.*, 1988) and so on. Several solid electrolytes are known such as silver iodide, AgI (Aono *et al.*, 1994; Owens and Argue, 1967; Takahashi *et al.*, 1972; Tatsumisago *et al.*, 1991) which transports Ag$^+$, β-alumina ((Na$_2$O)$_x$.11 Al$_2$O$_3$) (Whittingham and Huggins, 1971) and NASICON (Goodenough *et al.*, 1976) Na$_{1+x}$ Zr$_2$ Si$_x$ P$_{3-x}$ O$_{12}$ which transport Na$^+$, modified zirconia (Ca^{2+} or Y^{3+} doped ZrO$_2$) which is an oxide ion conductor (Aono *et al.*, 1994), or lithium ion conductors such as single crystal

(Aono $et\ al.$, 1994), or lithium ion conductors such as single crystal Li_3N (v. Alpen et $al.$, 1977; Boukamp and Huggins, 1978) and glasses based on Li_2S (Mercier $et\ al.$, 1981; Wada $et\ al.$, 1983; Kennedy $et\ al.$, 1986). However, the operation of this device requires an impractically high temperature. In this context, all solid state rechargeable batteries operating at room temperature are highly desirable because of several advantages such as high energy density (150 Wh/g), high voltage 4.0 V/cell) and longer charge retention characteristics (Aono $et\ al.$, 1994).

In spite of the attractive features of conventional solid electrolytes in various applications, one of the main difficulties in their use in all solid state batteries is the loss of contact between electrodes and electrolyte during the charge-discharge cycles of the battery. This is primarily as a result of dimensional changes occurring at the electrodes during the charging or discharging mode. Alternatively the solid electrolyte should be a material that is flexible and therefore can deform with the electrodes to suit the dimensional changes that occur so that interfacial contact is maintained throughout the operation of the battery. It is in this context that high molecular weight polymers, with specially designed architectures, are being investigated as solid electrolytes (Ratner and Shriver, 1988; Scrosati, 1993; Gray, 1991; Abraham and Alamgir, 1993; Armand, 1986).

Polymers that function as solid electrolytes are a subclass by themselves and are known as polymer electrolytes (Ratner and Shriver, 1988; Gray, 1991). Besides the advantage of flexibility, polymers can also be cast into thin films. Since thin films can minimize the resistance of the electrolyte, it also can reduce the volume and weight. Therefore, the use of polymer electrolytes can increase the energy stored per unit weight and volume. In view of these attractive features, there has been

considerable focus in recent years on the development of both inorganic and organic polymers as electrolytes for ion transport.

In 1973, Fenton *et al.* (1973) and Wright (1996) first reported the ionic conductivity of poly(ethylene oxide), $[CH_2CH_2O]_n$, (PEO), with alkali metal salts. This was followed by the visionary suggestion of Armand for the use of PEO as a solid electrolyte system for the transport of ions. Since then, the area of polymer electrolytes has attracted considerable interest. In the following account, first a discussion is presented on the general features applicable to polymer electrolytes. This is followed by an account on individual polymer electrolytes, particularly on modifications of PEO and related systems, and ether oxygen side chain containing organic and inorganic polymers. Some developments on the structural aspects of polymer electrolytes are also reviewed.

2.2 General Features

2.2.1 Requirements for Polymer Electrolyte

Since the polymers and metal salts involved are both solid materials, the preparation of polymer salt complex can be achieved by the dissolution of the two materials in a common solvent such as acetonitrile, methanol or THF, followed by a slow removal of the solvent under vacuum. This results in either the bulk polymer-salt complex or thin film depending upon the preparation method. It is essential to ensure that no trace of moisture is present and hence the operation should be carried out by glove box method. The essential reaction that occurs in the formation of polymer-metal salt complex can be written as

$$[A-B]_y \; + \; MX \; \rightarrow \; [A-B]_y \, . \, MX \qquad\qquad (2.1)$$

where $[A-B]_y$ is a polymer chain and MX is an alkali metal salt or a transition metal halide. Divalent metal salts have also been used (Ratner and Shriver, 1988).

Just as the dissolution of ionic salt in solvent requires that the solvation energy of ions in solution should overcome the lattice energy of ionic salt. Similarly, polymer-metal salt complex formation proceeds, provided the polymer matrix effectively solvates the ions and overcomes lattice energy of ionic salt. Three essential criteria for this process have been identified (MacCallum and Vincent, 1987):

(a) Electron pair donicity (DN)

(b) Acceptor number (AN) and

(c) Entropy term

The DN term measures the effectiveness of the solvent to function as a Lewis base in its ability to solvate the cation, i.e. Lewis acid. Thus, polymer which should function as a host in polymer electrolyte should posess donor sites such as oxygen, sulfur or nitrogen either in the backbone or in a group attached in the form of side chain. Similarly, the AN term describes the solvation of anion, i.e. Lewis base. PEO can be considered similar to 1,2-dimethoxy ethane (DN=22; AN=10.2) or even tetrahydrofuran (DN=20; AN=8).Thus PEO can effectively solvate cations possessing counter anions that are bulky delocalized anions such as I^-, ClO_4^-, BF_4^- or $CF_3SO_3^-$ which require little or no solvation. The third term (entropy) is related to the spatial disposition of the solvating unit and it has been shown that ethylene oxy (CH_2CH_2O) containing polymers such as PEO have the most favorable spatial orientation of the solvating units. While small ions such as Li^+ which can be strongly solvated, lead to

formation of polymer salt complexes even up to LiCl (lattice energy 853 kJ mol^{-1}), other larger cations such as Na$^+$, K$^+$ etc., require bulky counter anions like I$^-$, SCN$^-$, or CF$_3$SO$_3^-$ in order to be solvated by PEO (MacCallum and Vincent, 1989).

In addition to the above factors, it has also been recognized that polymer should possess a low cohesive energy and a high flexibility in order to effectively solvate the ions. The former is characterized by lack of intermolecular interactions such as hydrogen bonding while the latter feature is indicated by a low glass transition temperature (T$_g$). Thus although polymers like polyamides contain oxygen and nitrogen atoms as donor sites in their backbone, these polymers are quite unsuitable as polymer hosts in polymer electrolytes because of the presence of extensive intermolecular hydrogen bonding. Metal complexation with these polymers would lead to a disruption of this energetically favorable situation. The second factor, the high torsional flexibility of the polymer, is indicated by a low T$_g$ and is crucial for ion transport. Thus large segmental motions of the polymer (either the backbone or the side chain) which is possible above its T$_g$ can lead to fast ion movement.

In view of the above requirements, polymers that have been studied as polymer electrolytes are either oxygen-, nitrogen-, or sulfur-containing materials. The heteroatoms are either part of the backbone of the polymer or are present in the side chain attachments. Some important polymers include

(a) poly(ethylene oxide)

(b) poly(ethylene glycol)

(c) poly(propylene oxide)

(d) poly(siloxanes)

(e) poly(phosphazenes)

(f) poly(acrylates)

(g) poly(vinyl alcohol)

(h) poly(ethylene imine)

While oxygen-containing polymers have received more attention, other heteroatom-containing polymers have also been studied. In addition to homopolymers, copolymers containing more than one monomer have also received attention. Further, modifications of homopolymers by plasticizers, or crosslinking, or grafting to improve the properties of the polymers towards polymer-salt complex formation or increasing the dimensional stability of the materials has also been a focus of research.

In addition to the "salt in polymer" approach as described above, Angell and coworkers have described preparation of "polymer-in-salt" materials (Angell *et al.*, 1993). Lithium salts are mixed with small amounts of poly (propylene oxide) and poly (ethylene oxide) to afford rubbery materials with low glass transition temperatures. This new class of polymer electrolytes showed good lithium ion conductivities and high electrochemical stability.

2.2.2 Measurement of Ionic Conductivity in Polymer Electrolytes

In polymer electrolytes, the electronic conductivity is minimal and the conductivity observed is due to migration of ions. Measurement of this ionic conductivity, however, is not straightforward. This aspect has been dealt with elsewhere in details (K.S and R.H., 1941; Macdonald, 1973). However, a brief description of the method of measurement of ionic conductivity is given below.

Because of the resistance to ion flow at the electrode-electrolyte interface, "normal" measurement of total ionic conductivity is not possible in polymer electrolytes. In order to overcome this problem, the conductivity measurements are carried out by the ac impedance spectroscopy method, which minimizes the effects of cell polarization. The measurements are often made with the electrolyte sandwiched between a pair of electrochemically inert electrodes made of platinum or stainless steel. The detailed methodology of impedance spectroscopy is reviewed thoroughly elsewhere (K.S and R.H., 1941; Macdonald, 1973).

Briefly, impedance spectroscopy is a powerful method of characterizing many of the electrical properties of materials. The dynamics of bound or mobile charge carriers in the bulk or interfacial regions of any kind of solid or liquid materials such as ionic, semiconducting, mixed electronic-ionic and even insulators can be derived from impedance spectroscopy. In this technique the impedance is directly measured in the frequency domain by applying a single frequency voltage to the interface and measuring the phase shift and amplitude or real and imaginary parts of current at that frequency. When a sinusoidal potential is applied, the magnitude (I_m) and the phase shift (θ) of the current (i) which are measured with time (t) are given by

$$i(t) \; = \; I_m \sin (\omega \, t + \theta) \tag{2.2}$$

where ω is the frequency and θ is the phase difference between the voltage and current. These measurements are repeated from very low (10^{-4} Hz) to very high frequencies. From an analysis of this data, it is possible to arrive at the ac current vector (i_t^*) which is expressed in terms of real (i_t') and imaginary parts (i_t'')

$$i_t^* = i_t' + j i_t'' \quad ; \quad j = \sqrt{-1} \tag{2.3}$$

Similarly, ac potential is given by

$$\upsilon_t^* = \upsilon_t' + \upsilon_t'' \tag{2.4}$$

and ac impedance is expressed as

$$Z^* = Z' + jZ'' \quad ; \quad Z^* = \upsilon_t^* / i_t^* \tag{2.5}$$

In the impedance spectrum, also known as the cole-cole plot, the real part of impedance is plotted against the imaginary part for the data collected at various frequencies (Figure 2.1). From this plot, the bulk resistance of the electrolyte (R_b) is obtained. The conductivity (σ) can be obtained from

$$\sigma = g/R_b \tag{2.6}$$

$$R_b = Z^* \cos\theta \tag{2.7}$$

where g is the geometric factor of the electrolyte sample (thickness + area) in cm^{-1}, R_b is the bulk resistance, value at 100% resistance in ohms, Z^* is the impedance of the cell in ohms, and θ is the phase shift in degrees.
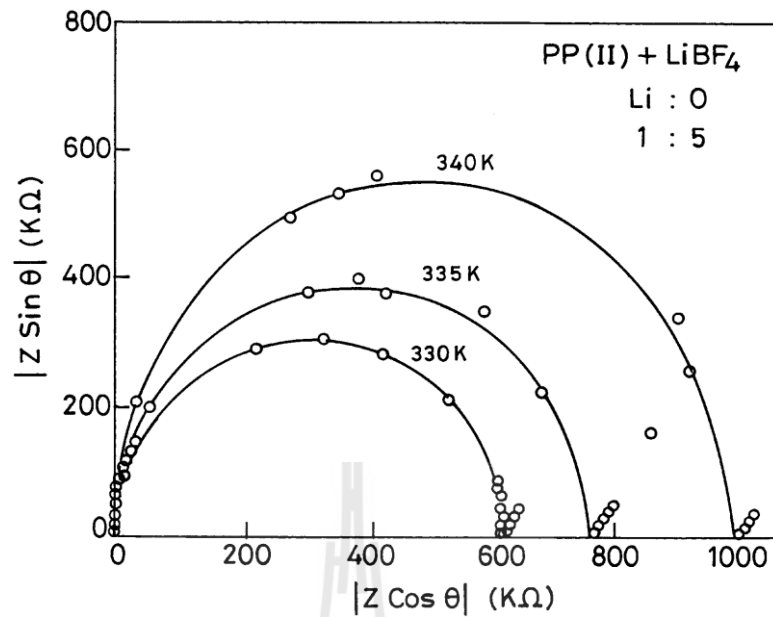
Figure 2.1 Representative impedance spectra of [(PP-II)-LiBF$_4$] (O:Li, 5:1) complex at three different temperatures (Mercier *et al.*, 1981).

2.2.3 Treatment of Conductivity Data

The conductivity data can be treated by Arrhenius equation

$$\sigma = Ae^{-E_A/kT} \tag{2.8}$$

or the VTF (Vogel-Tamann-Fulcher) equation

$$\sigma = Ae^{-B/K(T-T_0)} \tag{2.9}$$

The Arrhenius relation in which log (σT) is plotted against T^{-1} give a straight line. Generally, it has been observed that this plot is generally seen in conventional solid electrolytes as well as crystalline polymer electrolytes.

The VTF equation (Fulcher, 1925) where T_0 is a parameter to be determined (in many cases, however, it is found that T_0 is very close to T_g, the glass transition temperature), B is a constant called the pseudo activation energy and is different from the activation energy E_A that appears in the Arrhenius equation, is generally obeyed by amorphous polymer solid electrolytes.

After the above discussion on the general features of the polymer electrolytes, an account of some of the important individual polymer systems used in this thesis is given below.

2.3 Poly(ethylene oxide) (PEO)

PEO which is a linear polymer containing donor oxygen atoms in the main backbone is prepared by the ring opening polymerization of ethylene oxide. High molecular weight polymers upto 5×10^6 g/mol are available commercially. PEO is a semicrystalline material; about 70% of the bulk is crystalline at room temperature and the rest is present in an amorphous phase. The melting point of the crystalline phase (T_m) is 65 °C and the glass transition temperature of the amorphous phase (T_g) is -60 °C. PEO forms metal-salt complexes with a wide range of metal salts such as alkali and alkaline earth metals, and also transition metal salts (MacCallum and Vincent, 1987; Jones *et al.*, 1991). These include a number of mono and divalent cations such as Li^+, Na^+, K^+, Cs^+, Ag^+, Mg^{2+}, Ca^{2+}, Zn^{2+}, Cu^{2+} *etc.* with different counter anions such as BPh_4^-, $CF_3SO_3^-$, BF_4^-, ClO_4^-, SCN^-, I^- *etc.*

In order to understand the nature of PEO-metal salt complexes, attempts have been made to obtain and study their phase diagrams. In contrast to simple inorganic systems, for polymers, obtaining the phase diagrams is complicated as a result of slow

crystallizations as well as the presence of chain ends and defects. These result in an apparent violation of the Gibbs rule. In spite of these complications, phase diagram information is available for some PEO-metal salt compositions (Chiang *et al.*, 1985; Robitaille and Fauteux, 1986; Lee and Crist, 1986; Stainer *et al.*, 1984). The techniques used for obtaining this information are mainly polarized light microscopy (Himba, 1983), differential scanning calorimetry (Himba, 1983; Parker *et al.*, 1981), X-ray diffraction and NMR (Berthier *et al.*, 1983; Gorecki *et al.*, 1986; Bhattacharja *et al.*, 1986).

The maximum stoichiometry of polymer-metal salt complexes (CH_2CH_2O:metal salt), as shown by NMR and DSC studies, is 3:1 for smaller metal ions such as Li^+ or Na^+. Ions such as K^+ or NH_4^+ tend to form 4:1 complexes. Bulky symmetrical anions such as ClO_4^-, AsF_6^- and $CF_3SO_3^-$ favor 6:1 complexes. A eutectic or a quasi-eutectic exists between pure PEO and PEO-metal salt complexes. For example, the 3:1 complex between PEO and $LiCF_3SO_3$ shows a eutectic point which is very close to that of pure PEO itself in composition and melting temperature (30:1 and 60 °C). In contrast the 6:1 PEO:$LiClO_4$ complexes show a lower salt concentration (18:1 and 42 °C).

More recently, the phase diagram of the PEO system containing a divalent cation, PEO:$Ca(CF_3SO_3)_2$ has been elucidated by Bruce and coworkers (Bruce and Vincent, 1993) by using variable temperature powder X-ray diffraction (VTXRD) and differential scanning calorimetry (DSC). A 6:1 complex has been shown to form with two polymorphic phases. Figures 2.2, 2.3 and 2.4 show representative examples of the phase diagrams studies for the 3:1 (PEO:$LiClO_4$), 4:1 (PEO:NH_4SCN) and PEO$_4$:KSCN systems.

Use of multinuclear NMR (^{1}H, ^{7}Li and ^{19}F) has corroborated evidence from DSC towards phase information. Thus faster relaxation times (T$_2$) have been associated with crystalline phases and while longer T$_2$, values have been attributed to amorphous solid solutions (Berthier *et al.*, 1983). NMR measurements and conductivity study correlations with phase diagrams have clearly established that the amorphous elastomeric phase in PEO is primarily responsible for the ionic conductivity.
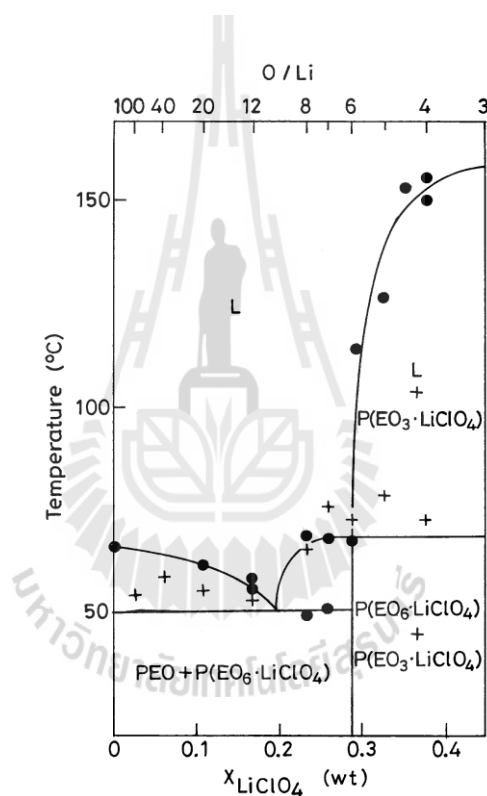
Figure 2.2 Phase diagram of PEO:LiClO$_4$ complexes (Robitaille and Fauteux, 1986).
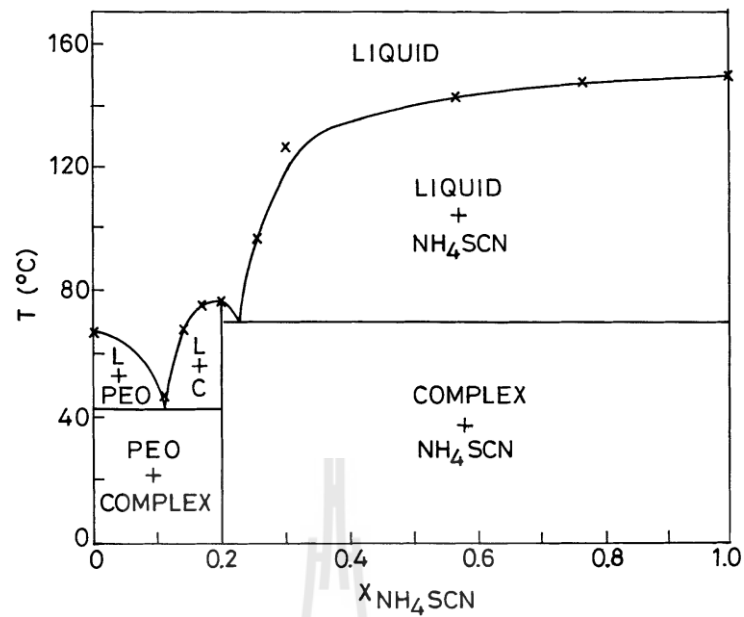
Figure 2.3 Phase diagram of PEO:NH$_4$SCN complex (Stainer *et al.*, 1984).
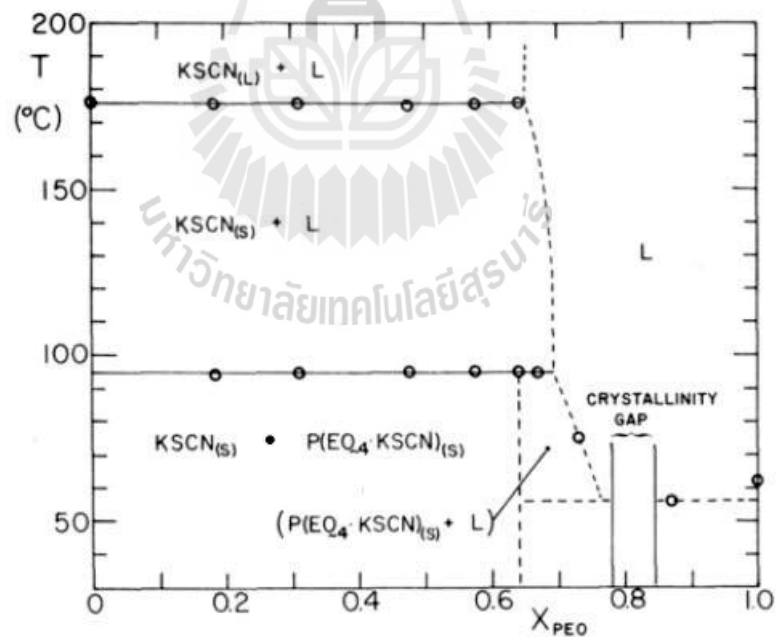
Figure 2.4 Phase diagram of PEO$_4$:KSCN complex (Robitaille *et al.*, 1987).

IR, Raman, NMR, X-ray and EXAFS studies on solid electrolytes give a substantial amount of information about the structure of the electrolytes and the dynamics of ion motion. Vibrational spectroscopy gives the direct evidence of the cation-polymer interaction. Far-IR studies confirm that the cation is coordinated to the ether oxygen atoms in PEO (Papke *et al.*, 1982b; Dupon *et al.*, 1982; Teeters and Frech, 1986; Papke *et al.*, 1982a) and other comb like acrylate polymers having short oligo oxyethylene side chains. The mechanism of conduction of ions involves local, liquid like motions of the solvent (poly ether in the case of PEO) with the ions then moving in the amorphous, locally disordered (liquid) phase. This implies curved plots, (log (σT) vs 1/T) over the entire temperature range with no discontinuities, much weaker stoichiometry dependence, and an increase in conduction with a decreased glass transition temperature.

IR and Raman studies on PEO:NaBF$_4$ and PEO:NaBH$_4$ systems reported by Dupon and coworkers (Dupon *et al.*, 1982), indicate that extensive ion pairing occurs in NaBH$_4$ complexes leading to low conductivity values. Absence of such pairing in NaBF$_4$ complexes leads to enhanced conductivity.

Typical conductivity vs composition and temperature plots for PEO:LiClO$_4$ and PEO:LiCF$_3$SO$_3$ are shown in Figure 2.5. Usually the conductivities are in the range of 10^{-3} to 10^{-4} S cm^{-1} at 100 °C and fall to 10^{-6} to 10^{-8} S cm^{-1} at room temperature. The molecular weight of the polymer changes the conductivity values. However, after a certain molecular weight, the conductivities are invariant with an increase in molecular weight of PEO. The highest conductivities are seen for the Li$^+$ salts while the least conductive are given by the sodium salts. Free volume and configurational entropy models have been used to describe the temperature and

concentration dependent behavior of the conductivity. These models have been described elsewhere (Cohen and Turnbull, 1959; Grest and Cohen, 1980; Gibbs and DiMarzio, 1958; Goldstein, 1973; Angell, 1983; Chaodamrongsakul, 2003).
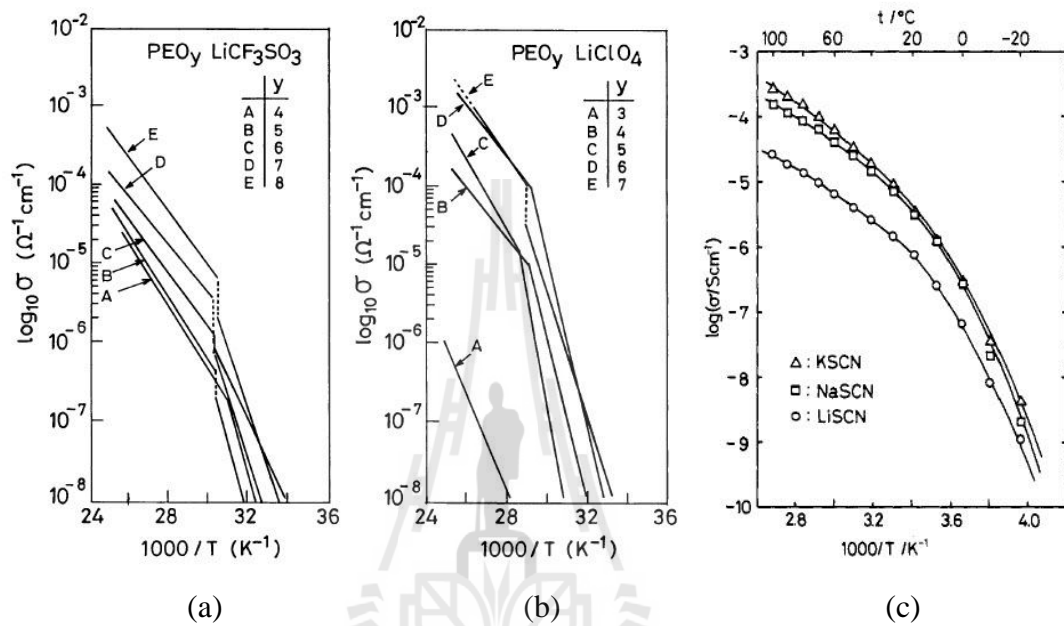
Figure 2.5 Conductivity plots for (a) $PEO_4:LiCF_3SO_3$, (b) $PEO_4:LiClO_4$ and (c) PEO:alkaline metal thiocyanate polymer electrolytes (Watanabe *et al.*, 1987; Robitaille and Fauteux, 1986)

In general the conductivity of PEO polymer electrolyte varies with the concentration of the dissolved salt with the maximum conductivity observed at an intermediate salt concentration. This is understood qualitatively by applying the VTF relation for conductivity. As discussed earlier, the T_0 is a parameter closely related to the T_g of the sample. In the absence of all other effects, increase of salt concentration should increase *A* and hence the conductivity. However, as the salt concentration is increased, there is a simultaneous increase in T_g and this leads to a decrease in

conductivity. Therefore, optimum salt concentrations are required for maximum conductivities. Generally, where phase diagrams have been studied, it is shown that for the eutectic composition a single amorphous phase is formed above the congruent melting point. This leads to an enhanced conductivity which is explained by the VTF equation. Above the eutectic point variation of conductivity appears linear on the Arrhenius plot (Ratner and Shriver, 1988; MacCallum and Vincent, 1987).

Attempts to obtain transport number information by various methods such as pulsed field gradient NMR (Bhattacharja *et al.*, 1986), radio tracer diffusion (Chadwick *et al.*, 1983), and potentiostatic polarization technique (Macdonald, 1973) have suggested that both cation and anion mobilities are important for the total ionic conductivity seen. In general, however, the nature of charge carriers in polymer electrolytes is quite complex and ion aggregates such as triple ions have been implicated in conductivity (Clancy *et al.*, 1986; Fauteux *et al.*, 1988).

2.4 Poly(propylene oxide) (PPO)

Since the high level of crystallinity in PEO-based polymer electrolytes is detrimental to the ionic conductivity below ~ 66 °C, one area of research has focused on producing materials that remain amorphous at these lower temperatures. Poly(propylene oxide) (PPO) would, in theory, appear to be an ideal candidate as a stable, amorphous host polymer. The random arrangement of the methyl groups along the chain prevents the polymer from crystallizing while maintaining the electrochemical stability advantage of PEO. Above 60-66 °C, the conductivity of PPO-salt systems does not compare favorably with analogous PEO systems as steric hindrance of the methyl groups along the chain limit the segmental motion required to

promote conductivity. In addition, this steric hindrance reduces polymer-cation interactions (Cowie and Cree, 1989; Frech *et al.*, 1988) and can even lead to salt precipitation at elevated temperatures. PPO has few advantages as a practical material, but it has been used extensively experimentally where a simple, amorphous host material is an essential requirement.

2.5 Poly(vinyl alcohol) (PVA)

PVA-based polymer electrolytes are known for their higher ease to form films and hydrophilicity to interact with -OH groups, exploitation of the same has been attempted for the development of novel category polymer batteries. It has a carbon chain backbone with hydroxy groups attached to methane carbon that acts as a source of hydrogen bonding and, therefore, assistance in the formation of polymer blends (Coleman and Painter, 1995). Kanbara (1991) studied PVA based electrolytes complexed with lithium salts for applications in electric double-layer capacitors. Chandrasekaran *et al.* (2001) reported the electrical conductivity of PVA-NaClO$_3$ electrolytes to be 10^{-6} S/cm. The conductivity of PVA polymer complexes also shows high values through the blending of PVA with other suitable polymers. Yang (2004) studied the conductivity and mechanical properties of alkaline composite polymer electrolyte with glass-fiber-mat support. It seems that the alkaline solid polymer film appears promising due to its highly potential candidates for application in high-density alkaline batteries system. There are very few literature data for the crystal structure and chemical composition analysis on the alkaline solid polymer electrolyte based on the PVA:KOH system. The ionic conductivity of the alkaline composite

polymer electrolyte is very dependent on the composition of KOH and H_2O in the films.

2.6 Conductivity Mechanism

Conductivity is often used to characterize the performance of polymer electrolytes and an approximate value of 10^{-5} Scm^{-1} has been adopted as a minimal requirement for practical applications (Gray, 1997). Our understanding of the ion transport mechanism is complicated and not completely clear because many of the polymer electrolytes studied have more than one phase. However, it has been shown that the amorphous phase is responsible for the ionic conductivity. At high temperatures, the crystalline phase can dissolve in the amorphous phase which has a higher concentration of charge carriers, thus increasing ionic conductivity. Higher ionic conductivity means that more charge can be transported through the polymer electrolyte per unit time. In other words, it represents one important performance measure for a polymer battery. As a result of the motion of polymer chains, cations are able to move between co-ordination sites, (such as oxygen atoms in the PEO polymer chain), either on one chain or between neighboring chains, called intrachain hopping and interchain hopping respectively shown in Figure 2.6 (Gray, 1997). Moreover, considering ion association from the ion-ion interactions between ions, there are other types of hopping mechanisms involving an ion cluster, as shown in Figure 2.7. The extent of these movements is dependent on the concentration of ions in the polymer host. It is assumed that interchain hopping brings about high ionic conductivity. To date, the conductivity mechanism in polymer electrolytes is still not fully understood.

Intrachain hopping

Interchain hopping
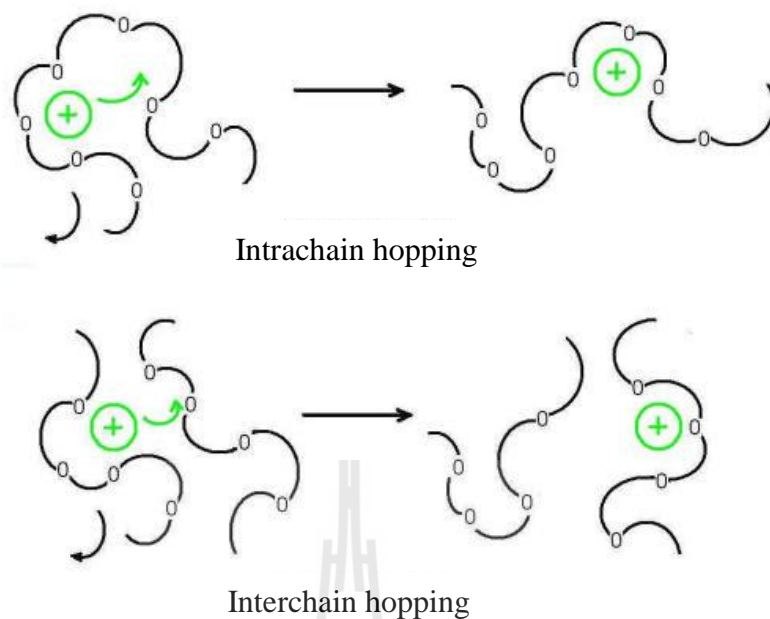
Figure 2.6 Cation motion in a polymer electrolyte assisted by polymer chains only (Gray, 1997).

Intrachain hopping via ion cluster

Intercluster hopping
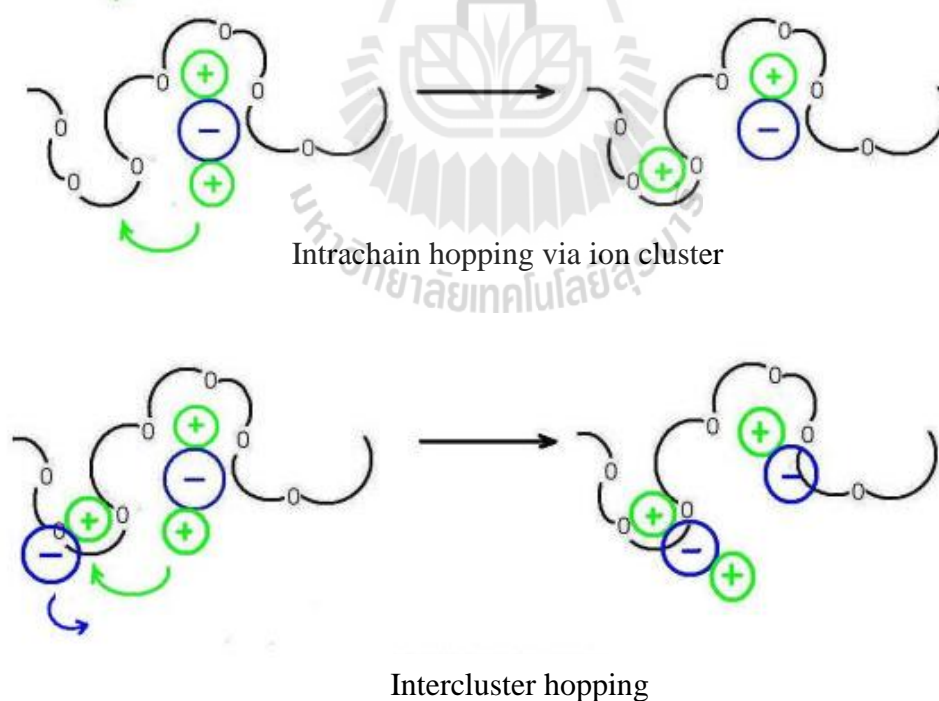
Figure 2.7 Cations motion in a polymer electrolyte facilitated by the ionic cluster (Gray, 1997).

2.7 Monte Carlo Simulation (MC)

The previous discussion shows that unmodified PEO is not ideal polymer host for ambient-temperature solid electrolytes; for example, its crystalline nature alone is a great hindrance to ionic transport. In attempts to improve the performance of PEO-salt systems, the plasticized systems will be much more interest because these systems have been most successful in achieving significant conductivities at room temperature.

The conductivities were enhanced by producing systems with less crystallinity and lower glass-transition temperatures than found in simple PEO-salt systems. Plasticizers, in addition to reducing the crystalline content and increasing the polymer segmental mobility, can result in greater ion dissociation, thus allowing large numbers of charge carriers for ionic transport; in addition, the cationic transport may be enhanced. In several studies (Hardy and Shriver, 1985; Spindler and Shriver, 1986; Ito *et al.*, 1987; Takeoka *et al.*, 1991; Iwatsuki *et al.*, 1992), the ionic conductivity of polymer electrolytes was increased by the addition of low molecular weight poly(ethylene glycol), PEG, which has the same repeat unit as PEO. The conductivity increases as the molecular weight of the PEG plasticizer decrease and as its content increase (Ito *et al.*, 1987). The PEG aids in ionic transport mainly by reducing crystallinity and increasing the free volume of the system.

The incorporation of low molecular weight polymer diffusing through a high molecular weight polymer has also been studied extensively in theoretical models. By appropriately constructing the molecular model for a polymer chain, computer simulation is a unique resource for the exploration of the molecular information. Simulation can provide microscopic information at the short distance and time scale

that otherwise may not be accessible from experimental methods. The objective of this thesis is use a faithfully designed Monte Carlo algorithm, which can be used to simulate static properties and dynamics of bidisperse poly(ethylene oxide).

2.7.1 Why Monte Carlo Simulations?

Monte Carlo methods are especially useful in studying systems with a large number of degrees of freedom, such as liquids, disordered materials, or strongly coupled solids (Tao, 1997). More broadly, they account for modeling phenomena with significant uncertainty and randomness in its nature.

The use of MC methods to model physical problems enables investigation of more complex systems at a shorter time scale. For a simple system, solving equations which account for the interactions between two atoms is fairly easy, but solving the same equations for hundreds or thousands of atoms is computationally too expensive, sometimes even impossible. With MC methods in fact, a large and complicated system can be sampled in a number of random configurations, which will later be used to describe the system as a whole. Random states of matter are generated independently from the prior states.

From a general point of view, MC simulations are more time efficient than classical MD simulations for the prediction of the static properties of amorphous polymers, especially in terms of computational time advantage. Proper equilibration of a dense amorphous polymer system by MD techniques calls for unfeasible simulation times. Thus, very large and complicated polymeric systems with huge characteristic length and time scales can only be simulated by MC techniques. That is

why MC technique is one of the most common simulation techniques for the polymeric systems since the early 1960's (Verdier and Stockmayer, 1962).

2.7.2 Why on Lattice Simulations?

Polymers are long molecules that are formed by the repetition of hundreds of monomer units on the main backbone of the chain. Thus, the characteristic length and time scales of the polymers that define their static and dynamic properties are obviously a few orders of magnitude higher than that of simple liquids. A 3-D simulation study, which targets to determine numerous static properties for instance, should cover a reasonably long length scale. Such simulations call for too much time and effort. Instead, the large number of degrees of freedom of the chain molecules can be diminished to lower values by the discretization of conformational space into lattice sites. Indeed, there are a number of algorithms to simplify the on-lattice modeling of the polymers on a coarse-grained scale (Random Walks, Self Avoiding Walks, etc.), which are very useful to speed up the simulations. Particularly in this thesis, RIS calculations are utilized to govern the bonded interactions between the coarse-grained beads of polymer molecules, which enforce the local conformational preferences.

There are different types of lattices (cubic lattices, diamond lattice, etc.) used for the simulations of polymer molecules (Kotelyanskii and Theodorou, 2004). The selection of the lattice type, especially for MC simulations, is very important in terms of ergodicity concerns. MC calculations are based on the fact that the studied system is stochastic and its properties may not depend on the history of the trajectory of the states generated. Namely, the next generated configuration of the system should not

be dependent upon the prior states. The only thing that relates two consecutive steps is the corresponding energy difference between two configurations, i.e. the configurations before and after the move made. That energy difference is used to calculate the Metropolis factor which is the only criteria to accept or reject the newly generated configuration (Binder, 1995). So, the number of the configurations should be large enough to be able to represent the studied system as a whole, which brings up the ergodicity concerns. In addition, the use of simplified models on a coarse-grained level leads to another drawback: the loss of the chemical details during the switch from a fully atomistic representation to a coarse-grained scale representation. The latter drawback is more significant when a well-defined (M, composition, etc.) polymeric system is targeted to reproduce the physical properties that are common to the all chain molecules (Kotelyanskii and Theodorou, 2004). Therefore, the lack of both ergodicity in the simulated system and atomistic details on the model may cause the false determination of the static and dynamic properties of interest. The former problem may be eliminated by the use of a lattice with a coordination number (N-the number of lattice states that are the neighbors of the central lattice site of interest) as high as possible because the higher the coordination number is, the larger the number of degrees of freedom is. The latter problem can be eliminated as well, only if the information that is stored in every single snapshot of a coarse-grained representation can be transferred into the continuous space with fully atomistic detail of the system. This thesis presents the results from MC simulations that are performed on a recently developed second nearest neighbor diamond (2nnd) lattice (Rapold and Mattice, 1995; Baschnagel *et al.*, 2000). The use of 2nnd lattice eliminates both drawbacks as it has a CN of 12, whereas the cubic and diamond lattices have the Ns of 6 and 4,

respectively. Another advantage of 2nnd lattice is that it is possible to go back and forth between coarse-grained and fully atomistic representations.

2.7.3 The Second Nearest Neighbor Diamond Lattice

The simulations presented in this thesis are performed on a high coordination lattice called "second nearest neighbor diamond lattice". 2nnd lattice is a coarse-grained representation of the diamond lattice in such a way that every second site on the diamond lattice is discarded and the first and third elements of the lattice sites are connected to each other (Rapold and Mattice, 1995; Cho and Mattice, 1997). The representation of coarse-grained beads, which corresponds to a complete monomeric unit, is identical with the closest packing of uniform hard spheres since both cases have a coordination number of 12. The high N not only increases the number of degrees of freedom associated with the system, but also facilitates the most possible realistic representation (in terms of flexibility to define the rotational state) of polymer molecules on the coarse-grained level. Local and non-local interactions used on the 2nnd lattice have recently been developed for a variety of polymer molecules, based on RIS calculations and a discretized form of the Lennard Jones (LJ) potential, respectively (Cho and Mattice, 1997; Doruker and Mattice, 1998; Haliloglu and Mattice, 1998).

Another beauty of this recently developed lattice is that the coarse-grained configurations of polymer chains can be converted into the configurations with fully atomistic detail on the underlying diamond lattice at any time of the simulation (Rapold and Mattice, 1995; Cho and Mattice, 1997; Haliloglu and Mattice, 1998; Doruker and Mattice, 1998). The diamond lattice enables the most realistic on-lattice

representation of polymer molecules since the angle between two consecutive bonds is the tetrahedral bond angle of the saturated carbon covalent bonds (Smith, 1964; Thorpe and Schroll, 1981).

CHAPTER III

EXAFS AND COMPUTATIONAL MOLECULAR

MODELING

3.1 Extended X-ray Absorption Fine Structure Spectroscopy (EXAFS)

X-ray Absorption Spectroscopy (XAS) includes both Extended X-ray Absorption Fine Structure (EXAFS) and X-ray Absorption Near Edge Structure (XANES). XAS that became available with the development of synchrotron radiation sources has introduced powerful experimental methods for the investigation of atomic and molecular structures of materials. With the synchrotron radiation high-flux monochromatic x-ray beams with the energy resolution $\Delta E/E$ of the order of 10^{-4} are easily obtainable, allowing measurements of high quality absorption spectra in a short time.

The basic physics of EXAFS is easy to understand. EXAFS does not occur for isolated atoms but only appears when atoms are in the condensed state. Thus, one has to understand how the absorption is modified in the condensed state to produce EXAFS. The absorption edge corresponds to an X-ray photon having enough energy to just free a bound electron in atom. When the electron are in the most tightly bound $n=1$ shell the edge is called the K-edge. For the next most tightly bound shell of atoms, the $n=2$ shell, the corresponding edges are called the L-edges. At present these

edges are the only one used to the observe EXAFS, thought in principle $n=3$ or higher shells could be used.

X-ray absorption in the photon rang up to 40 keV, the range of the most importance for EXAFS, is dominated by photoelectron absorption where the photon is the completely absorbed, transferring its energy to the excited a photoelectron and leaving behind a core hole in the atom. The excited atom with the core hole has some probability of having additional excitations, but this multi-electron excitation is neglected for now. Assuming that all the absorbed photon energy go into exciting a single core electron, the kinetic energy of excited photoelectron is given by the difference between the photon energy and the electron binding energy in the atom. When the photoelectron has about 15 eV or greater kinetic energy (i.e., for photon energies of 15 eV or more above the edge), this energy is large compared with its interaction energy with the surrounding energy with the surrounding atoms (~3 eV). In that case the interaction with the surrounding medium can be treated can as a perturbation about an isolated atom. Obviously, only the final state of the photo-electron is perturbed by the surroundings. A deep core level, the initial state, is unaffected to a very good approximation.

The final-state photoelectron is modified to first order by a single scattering from each surrounding atom. Quantum mechanically the photoelectron must be treated as a wave whose wavelength (λ) given by the de Broglie relation

$$\lambda = \frac{\hbar}{p} \tag{3.1}$$

Where p is the momentum of the photoelectron and $\hbar$ is Planck's constant. In the EXAFS regime p can be determined by the free electron relation

$$\frac{p^2}{2m} = \hbar\upsilon - E_0 \tag{3.2}$$

where the x-ray photon of frequency (υ) has energy $\hbar\upsilon$ and E_0 is the binding energy of the photoelectron.

For an isolated atom, photoelectron can be represented as an outgoing wave as shown in Figure 3.1 by the solid lines. The surrounding atoms will scatter the outgoing waves as indicated by the dash lines. The final state is the superposition of the outgoing and scattered waves.
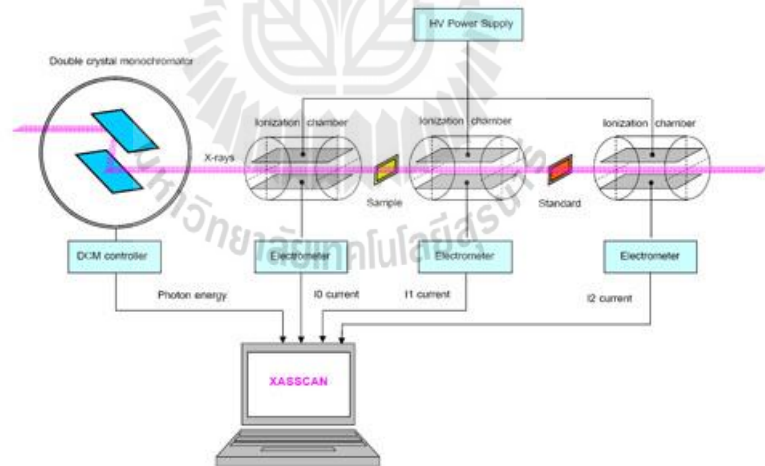
Figure 3.1 Schematic views of X-ray beamline (BL-8) at Synchrotron Light Research Institute (Public Organization) at Nakhon Ratchasima in Thailand.

The absorption X-ray is given quantum mechanically by matrix element between the initial and final states. In our case the initial state is the electron in the

atomic core and the state is this electron excited to the escaping photoelectron. The matrix element is nonzero only in the region where the core state is nonzero that is near the center of the absorbing atom. Thus, it is only necessary to determine how the photoelectron is modified by the surrounding atoms at the center of the absorbing atom to determine the modification leading to EXAFS.

The backscattered waves in Figure 3.1 will add or subtract from the outgoing wave at the center depending on their relative phase. The total amplitude of the electron wave function will be enhanced or reduced, respectively, thus modifying the probability of absorption of the X-ray correspondingly. As the energy of the photoelectron varies, its wavelength varies as indicated in Equation (3.1) and (3.2), changing the relative phase. Thus the variation of the fine structure in EXAFS as shown in Figure 3.2 is a direct consequence of the wave nature of the photoelectron. The peaks correspond to the backscattered wave being in phase with the outgoing part while the valleys appear when the out of phase

How the phase varies with the wavelength of the photoelectron depend on the distance between the center atom and backscattering atom. The variation of the backscattering strength as a function of energy of the photoelectron depends on the type of atom doing the backscattering. Thus EXAFS contains information on the type of atom doing the backscattering and information on the atom surroundings of the center atom. With a more quantitative description of EXAFS, it is possible to obtain all these information.
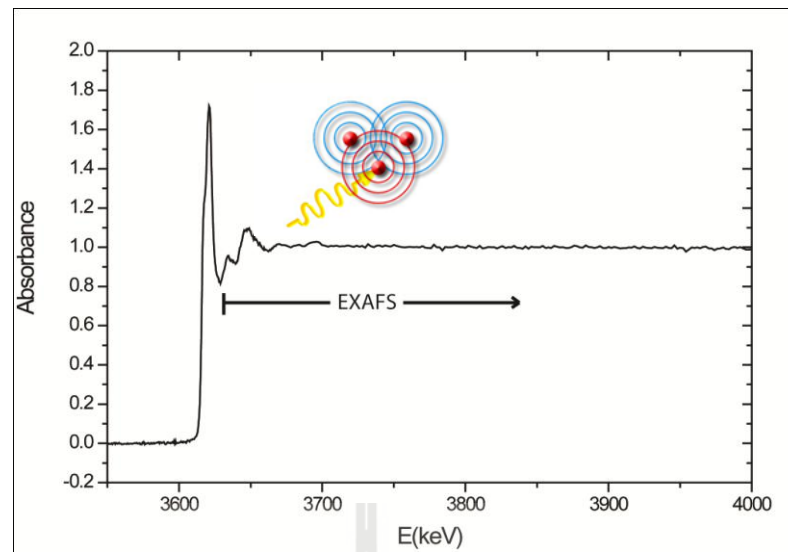
Figure 3.2 X-ray absorption spectra of KCl water solution in the energy range of K K-edge.

We can directly translate the qualitative picture into an expression for EXAFS. As discussed previously, the absorption is proportional to the amplitude of the photoelectron at the origin and the oscillatory part of this part, is produced by the interference between the outgoing and the backscattered wave dependent on their relative phase. The spherical outgoing wave of wave number $k \equiv 2\pi/\lambda$, where λ is the wavelength of Equation (3.1), is proportional to $r^{-1}\exp(ikr)$. The backscattered wave $\exp(ik|r-r_i|)|r-r_i|^{-1}$ is proportional to the product of the amplitude of outgoing wave at position r_i of the backscatter, and a backward scattering amplitude $T_i(2k)$ characteristic of the backscatter, that is,

$$T_i(2k)\frac{e^{ikr_i}}{r_i}\frac{e^{ik|r-r_i|}}{|r-r_i|}$$

(3.3)

The complex form of the spherical waves is employed where it is understood that the real part of the wave is to be taken at the end. The backscattered wave in Equation (3.3) emanates from r_i instead of from the outgoing wave. At the origin ($r = 0$) the backscattered spherical wave in Equation (3.3) has an amplitude proportional to $T_i(2k)\dfrac{e^{i2kr_i}}{r_i^2}$, the factor $2kr_i$ is the phase shift introduced by a wave of wave number $k = 2\pi/\lambda$ in traveling the distance $2r_i$ from the origin and back from the backscatter. This expression would be adequate if the electron were moving in a constant potential. However, the electron moves out of and into the varying potential of the center atom and also sense the varying potential of the backscattering atom. These potential add additional phase shifts that we call scattering atom. These potentials add additional phase shifts that we call $[\delta_i(k) - (\pi/2)]$.

The complex expression for the backscattered wave becomes

$$\frac{T_i(2k)e^{i[2kr_i+\delta_i(k)-\pi/2]}}{r_i^2} \tag{3.4}$$

The backscattered wave modifies the absorption as it interferes with the outgoing wave, and this modification is, by definition, the EXAFS. The real part of Equation (3.4) is thus proportional to EXAFS, which we denote by $\chi_i(k)$,

$$\chi_i(k) = K\frac{T_i(2k)}{r_i^2}\sin[2kr_i + \delta_i(k)] \tag{3.5}$$

Here K is a constant of proportionality. Finally, K is incorporated into $T(2k)$ by defining

$$\frac{m}{2\pi\hbar^2 k^2}t_i(2k) = KT_i(2k) \tag{3.6}$$

The expression for the EXAFS then becomes

$$\chi_i(k) = \frac{m}{2\pi\hbar^2}t_i(2k)\frac{\sin[2kr_i + \delta_i(k)]}{(kr_i)^2} \tag{3.7}$$

In the single-scattering approximation, the effect of many scatters can be obtained by simply adding the effects of each scatters, and the total EXAFS becomes

$$\chi(k) = \sum_i \chi_i(k) = \sum_i \frac{m}{2\pi\hbar^2}\frac{t_i(2k)}{(kr_i)^2}\sin[2kr_i + \delta_i(k)] \tag{3.8}$$

This derivation has left out one important physical effect, namely, the lifetime of the excited photoelectron state. There are two contributions to this lifetime. The hole in the atom, left behind after the excitation of the photoelectron, is filled in a time of the order of 10^{-15} s for the K-shall of copper. The hole lifetime varies from atom to atom and from shell to shell in a manner that has been tabulated in reported (Keski-Rahkomen and Krause, 1974). The photoelectron itself has a finite lifetime because of scattering from the surrounding electrons and atoms. These two lifetimes contribute to determine the finite lifetime of the excited state consisting of the photoelectron

together with the core hole from which it came. The lifetimes is important because in order for the backscattered wave to interfere with the outing wave, the two must be coherent; that is, the phase difference between the two must be well defined, as in Equations (3.4) and (3.5). The processes that determine the lifetime destroy the coherence of the final state and thus the interference that produces the EXAFS. The lifetime effect can phenomenologically be taken into account by a mean free path term $\exp(-2r_i / \lambda)$, which represent the probability that the photoelectron travels to the backscattering atom and return without scattering or the hole being filled. The term λ is the mean free path and is, in general, a function of k. Adding the lifetime contribution to $\chi(k)$, Equation (3.8) becomes

$$\chi(k) = \frac{m}{2\pi\hbar^2 k^2} \sum_i \frac{t_i(2k)\exp(-2r_i / \lambda)}{r_i^2} \sin[2kr_i + \delta_i(k)] \qquad (3.9)$$

The sum in Equation (3.9) is over the surrounding atoms at distance r_i from the X-ray absorbing atom, if, instead of summimg over all atoms, we divide the sum first over atoms that have approximately the same average distance R_i from the center, that is, over coordination shells, and then sum over coordinate shells, the more common form of the EXAFS expression can be obtained. In any coordination shell the atoms will not all be exactly in phase. If this disorder is small and has a Gaussian distribution about the average distance R_j, that is, it has a probability of deviating from the average by

$$(2\pi\sigma_i^2)\exp(-\frac{(r_i - R_j)^2}{2\sigma_i^2})$$

(3.10)

Then the dephasing it produces additional factor $N_i\exp(-2k^2\sigma_i^2)$ to the EXAFS expression instead of N_i, where N_i is the number of atoms of the type i in the shell and σ_i is the rms deviation from the average distance R_j. The EXAFS in Equation (3.9) then becomes

$$\chi(k) = \frac{m}{2\pi\hbar^2 k^2}\sum_i N_i\frac{t_i(2k)}{R_i^2}\exp(-2k^2\sigma_i^2)$$

$$\bullet\exp(\frac{-2R_i}{\lambda})\sin[2kR_i + \delta_i(k)]$$

(3.11)

Shorter wavelength or larger k sense a larger dephasing effect and the EXAFS is correspondingly smeared out. The sum remaining in Equation (3.11) is over coordination shell at average distance R_i. All the same atoms are assumed in each coordination so that $t_i(2k)$ is the same. If there are different atoms approximately the same average distance apart, then each type of atom would constitute a separate coordination shell and the sum in Equation (3.11) is over each of these coordination shells, even though they may have the same R_i. This expression (3.11) is valid for all polycrystalline samples, cubic crystals, and amorphous and liquid materials.

In typical experimental set-up (Figure 3.1) ionization cells monitor the intensity of incident (I_0) and transmitted (I_1) monochromatic photon beam through the sample. With the well-known exponential attenuation of X-rays in a homogeneous

medium, the absorption coefficient $\mu(E)$ at a given photon energy E can be obtained

from the relation:

$$\mu(E) = \frac{-\ln(I_1/I_0)}{d} \tag{3.12}$$

where d is the sample thickness. The energy dependence of the absorption coefficient

is collected by a stepwise scan of the photon energy in the monochromatic beam with

the Bragg monochromator.

These are the absorption edges, and they correspond to the binding energies of

the inner-shell electrons. As each chemical element has specific, well-defined binding

energies, it is possible to select an energy range for the X-ray beam sweeping

specifically only an absorption edge (and the following) region of a selected element.

This way information of the neighbourhood of the atoms of this chosen chemical

element can be obtained.

The dominant process in the x-ray absorption at photon energies below 100

keV is photoeffect, whereby the photon is completely absorbed, transferring its

energy to the ejected photoelectron. The X-ray absorption coefficient for photoeffect

decreases smoothly with increasing photon energy. However, when the photon energy

reaches one of the deep inner-shell ionization energies of the atom, a sharp jump

(absorption edge) marks the opening of an additional photoabsorption channel.

Immediately above the absorption edge, in a range of up to 1000 eV, a precise

measurement of absorption shows rich fine structure superposed onto the smooth

energy dependence. The structure is called Extended X-ray Absorption Fine Structure.

An example is shown in Figure 3.2, where *K*-edge absorption spectrum of potassium measured on KCl in water solution, is plotted.

3.2 Computational Chemistry

Since the development of the first computers in the early 1950's, scientists have tried to explore how these machines might be used in Chemistry. From the very beginning, the field of computational chemistry focused either on solving complex mathematical problems, typically quantum mechanical, or has tried to model the dynamical behavior of atomic and molecular systems. The boundaries between these two areas have never been well defined and, today, we see a convergence between quantum chemistry and simulation in studying chemical reactions (Curtiss and Gordon, 2004).

With advances in computer technology leading to ever faster computers, computational chemistry has become an increasingly reliable tool for investigating systems where experimental techniques still provide too little information. Ultra-fast spectroscopy can be used to follow fast reactions but only at a molecular level. A variety of diffraction techniques can also give detailed information about crystalline structure, but have difficulties monitoring changes at a molecular level. This is why the exponential growth in computer power has led to a corresponding growth in the number of computational chemists and in the variety of different computational techniques available for solving chemical problems: *ab initio* Quantum Mechanics (QM), Density Functional Theory (DFT), semi-empirical methods, Molecular Mechanics (MM), Monte Carlo (MC), Molecular Dynamics (MD), *etc.*

There are two main branches within computational chemistry: the computationally expensive methods which try to explore the electronic structure of small systems or systems with fixed crystal structures by quantum mechanical methods; and the methods which focus on the atomic structure and dynamics of much larger systems but using less complex calculations. In this thesis, the focus is on the latter – simulating atomic and molecular interaction with the mathematics of classical mechanics. The following text is based on (Allen, 1987; Haile, 1997; Colboum, 1994; Rapaport, 1995).

It has been argued that computational chemistry is both "theory" and "experiment": "theory" since clearly no measurements are made on a real system, and "experiment" since the potentials used are often based on experimental data on simple systems. MD is indeed often referred to as a "computer experiment".

Today, most computational chemists would probably say that computation is neither theory nor experiment, but rather a third leg on the chemical body - both to test theory and to interpret experiment; alternatively, to perform "experiments" on systems inaccessible to normal experimental techniques.

This discussion puts focus on the relationship between MD and experiment. Experimentalists interpret their data using theories and models – they do not anticipate reality. Experimental data can often be interpreted in several ways, sometimes even within the same theoretical context. Not rarely are data interpreted on the basis of incorrect or inappropriate theory for the system under study. The interpretation of experimental results is not a search for biblical "truth", just like the computational chemist, the experimentalists use models to make their interpretation,

thereby creating a gap between themselves and reality. MD can indeed sometimes be as good (or bad) a method as experiment for modeling this reality.

3.2.1 Molecular Dynamics (MD)

3.2.1.1 Simulation Method

In reality, atoms and molecules in solid materials are far from static unless the temperature is low; but even at 0 K, vibrational motion remains. For ionically conductive materials, atomic movement is the subject of major interest. Molecular Dynamics (MD) allows us to simulate the dynamics of the particles in a well-defined system to gain greater insights into local structure and local dynamics - such as ion transport in solid materials.

In MD simulation, atomic motion in a chemical system is described in classical mechanics terms by solving Newton's equations of motion:

$$\vec{F}_i = m_i \vec{a}_i \tag{3.13}$$

for each atom i in a system of N atoms: m_i is their respective atomic mass; $a_i = d^2 r_i / dr^2$ is their acceleration; and F_i is the force acting upon atom i due to interactions with all other particles in the system. The forces are generated from a universal energy potential E:

$$-\frac{dE}{d\vec{r}_i} = \vec{F}_i = m_i \frac{d^2 \vec{r}_i}{dt^2} \tag{3.14}$$

The basic idea of MD goes back to classical idea in Physics - that if one knows the location of the particles in the Universe, and the forces acting between them, one is able to predict the entire future. In a normal MD simulation, this Universe comprises only a few thousand atoms; in extreme cases, up to a million.

With Newton's equations, it is possible to calculate sequentially the locations and velocities of all particles in the system. This generates a sequence of snapshots which constitutes a "movie" of the simulated system on the atomic scale. Due to the massive computer time necessary to solve these equations for a large number of particles, the movies are generally fairly short - in this work in the pico- or nanosecond regime. All that is needed to solve the equations of motion are the masses of the particles and a description of the potentials, E.

In order to solve Equation (3.14), various kinds of numerical integration methods such as Gear, Verlet, leapfrog, and velocity Verlet have been developed. From the Verlet algorithm, which is based on particle position at time t, $r(t)$, acceleration at time t, $a(t)$, and the position from previous time $r(t-\Delta t)$, the new position of a particle after time Δt (Δt is the time-step between two snapshots.) is given by

$$r(t+\Delta t) = 2r(t) - r(t-\Delta t) + \Delta t^2 a(t) \tag{3.15}$$

Then, the velocity at time t can be calculated by

$$v(t) = \frac{r(t+\Delta t) - r(t-\Delta t)}{2\Delta t} \tag{3.16}$$

The Verlet algorithm uses no explicit velocities. The advantages of the Verlet algorithm are, (*i*) it is straightforward, and (*ii*) the storage requirements are modest. The disadvantage is that the algorithm is of moderate precision.

The leapfrog algorithm works stepwise by:

1. Calculating the acceleration at time t according to Equation (3.2).

2. Updating the velocity at time $t + \Delta t / 2$ using

$$v(t + \Delta t / 2) = v(t - \Delta t / 2) + a(t)\Delta t \tag{3.17}$$

3. Calculating the atom position in the snapshot using:

$$r(t + \Delta t) = r(t) + v(t + \Delta t / 2)\Delta t \tag{3.18}$$

In this way, the velocities *leap* over the positions, then the positions *leap* over the velocities. The advantage of this algorithm is that the velocities are explicitly calculated, however, the disadvantage is that they are not calculated at the same time as the positions.

The velocity Verlet algorithm is as follows:

$$r(t + \Delta t) = r(t) + \Delta t v(t) + \frac{\Delta t^2 a(t)}{2} \tag{3.19}$$

$$a(t + \Delta t) = \frac{f(t + \Delta t)}{m} \tag{3.20}$$

$$v(t + \Delta t) = v(t) + \frac{1}{2} \Delta t \left[a(t) + a(t + \Delta t) \right] \tag{3.21}$$

This algorithm yields positions, velocities and accelerations at the same time. There is no compromise on precision.

The MD simulation method is very straightforward, but one must bear in mind that it is based on some severe approximations. At the highest level, the Born-Oppenheimer approximation is made, separating the wavefunction for the electrons from those of the nuclei. The Schrödinger equation can then be solved for every fixed nuclear arrangement, given the electronic energy contribution. Together with the nuclear –nuclear repulsion, this energy determines the potential energy surface, *E*. At the next level of approximation, all nuclei are treated as classical particles moving on the potential energy surface, and Schrödinger equation is replaced by Newton's equations of motion. At the lowest level of approximation, the potential energy surface is approximated to an analytical potential energy function which gives the potential energy and interatomic forces as a function of atomic coordinates.

3.2.1.2 Forcefields for MD Simulations

In the context of molecular modeling, a forcefield means the energy functions and parameter sets used to calculate the potential energy of a system. The energy functions and parameter sets are either derived from quantum chemistry calculations or empirically from experimental data. Typically, classical forcefields employ two-body pairwise additive potentials and ignore multi-body dispersion and many-body polarization effects. The basic functional form of a classical forcefield can be

regarded as the sum of nonbonded interactions, also called intermolecular interactions, and intramolecular interactions (bond stretch, valence angles and dihedral angles):

$$E = \sum_{i \neq j} E_{ij}^{NB}(r) + \sum_{ij} E_{ij}^{s}(r) + \sum_{ijk} E_{ijk}^{b}(\theta) + \sum_{ijkl} E_{ijkl}^{t}(\Phi) \qquad (3.22)$$

where r is the distance between atom centers, $E_{ij}^{NB}(r)$ is the nonbonded energy associated between atom i and j , $E_{ij}^{s}(r)$ is the covalent bond stretching energy between atom pair i and j , $E_{ijk}^{b}(\theta)$ is the bond-angle bending energy that depends on the angle θ formed by atoms i , j and k , and $E_{ijkl}^{t}(\Phi)$ is the torsional energy arising from rotation around the dihedral angle Φ defined by atoms i,j,k and l . Nonbonded interactions $E_{ij}^{NB}(r)$, the interactions between atoms in different molecules or in the same molecules separated by two or more bonds, are composed of electrostatic interactions and van der Waals interactions as given by:

$$E_{ij}^{NB}(r) = E_{ij}^{elec}(r) + E_{ij}^{vdw}(r) \qquad (3.23)$$

The summations run over all interactions of each type present in each molecule and between molecules. The bond-stretching, bond-angle and torsional-angle terms have many forms. In the vast majority of forcefields used in MD simulations, bond breaking is not possible; this is also the case for the forcefields used in this work. The electrostatic energy, E_{ij}^{elec} , also called the Coulombic energy, is directly related to atomic charges by Coulomb's law,

$$E_{ij}^{elec}(r) = \frac{1}{4\pi\varepsilon_0} \frac{q_i q_j}{r} \tag{3.24}$$

where q_i, q_j are the charges on atoms i and j, and ε_0 is the permittivity of free space. There are many forms used to describe the van der Waals energy. The two most popularly used are the Lennard-Jones (LJ) potential (Lennard-Jones, 1931),

$$U(r) = \left(\frac{A}{r^{12}}\right) - \left(\frac{B}{r^6}\right) = 4\varepsilon\left[\left(\frac{\sigma}{r}\right)^{12} - \left(\frac{\sigma}{r}\right)^6\right] \tag{3.25}$$

where $A = 4\varepsilon\sigma^{12}$ and $B = 4\varepsilon\sigma^6$ or the Buckingham potential,

$$U(r) = A' \exp(-B'r) - \frac{C'}{r^6} \tag{3.26}$$

In Equations (3.25) and (3.26), A, B, ε, σ, A', B' and C' are constants fitted to *ab initio* and/or experimental data. The parameters A' and B' determine the short range repulsive interaction, C' is the dispersion parameter. The parameters ε and σ have the significance of being the depth and zero point of the potential. Both the LJ and Buckingham potential include the long-range London dispersion term.

Such classical forcefields are used widely in MD simulations of polymer electrolytes, but recent molecular dynamics simulations by Smith and coworkers have shown that polarization effects can play a very important role for these systems and should not be ignored (Londono *et al.*, 1997).

3.2.1.3 Periodic Boundary Conditions and Other Requirements

Since the computation time required to calculate the trajectories of all N particles in a simulation box increases with N^2, the simulated system cannot be made large enough to accurately represent the bulk properties of an actual crystal or amorphous material: surface effects would always be present. This problem is solved by implementing periodic boundary conditions, in which the simulation box is replicated through space in all directions; see Figure 3.3. The set of atom present in the box is thus surrounded by exact replicas of itself, *i.e.* periodic images. If an atom moves through a boundary on one side of the simulation box, so will its replica on the other side. This keeps the number of atoms in one box constant, and if the box has constant volume the simulation then preserves the density of the system, which can affect the properties of the simulation, but much less than the surface effect would have done without the periodicity. An MD simulation should also follow the laws of thermodynamics. At equilibrium, it should have a specific temperature, volume, energy, density, pressure, heat capacity, *etc.* In statistical thermodynamics, this constitutes the state of the system; its *ensemble*. Since MD is a statistical mechanic method, an evaluation of these physical quantities can be made from the velocities and masses of the particles in the system. MD can also serve as a link between these atomic-level quantities and macroscopic properties. Three different ensembles have been used here:

1. The microcanonical ensemble (NVE), which maintains the system under constant energy (E) and with constant number of particles (N) in a well-defined box with volume (V). This is appropriate during the initial equilibration phase of a simulation.

2. The isothermal-isobaric ensemble (NPT), where temperature and pressure are kept constant. This is normally the best model of the experimental conditions.

3. The canonical ensemble (NVT), where volume and temperature are kept constant. This ensemble has been used for most simulations, so that comparisons can be made with experimental data from structures with fixed dimensions.
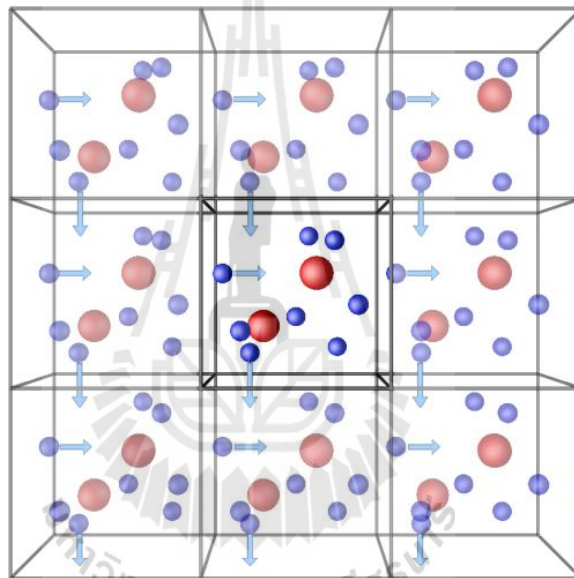
Figure 3.3 Periodic boundary conditions in molecular simulation.

One factor that impacts total CPU time required by a simulation is the size of the integration time-step (Δt). This is the time length between evaluations of the potential. The time-step must be chosen small enough to avoid discretization errors (*i.e.* smaller than the fastest vibrational frequency in the system). Typical time-step for classical MD is in the order of 1 femtosecond (10^{-15} s). This value may be extended by using algorithms such as *SHAKE*, which fix the vibrations of the fastest

atoms (*e.g.* hydrogens) into place (Wikipedia, 2008). The SHAKE algorithm, a modification of the Verlet algorithm, has become the standard approach for doing molecular dynamics with fixed bond lengths. It can also be used to hold angles fixed, but this is less common. It works well for time-step up to 5 fs, thereby enabling a five-fold speedup in computational time as long as the process of iteratively solving the constraint equations does not consume too much time (Mathiowetz, 1994).

3.2.1.4 Atomistics Molecular Structure from MD Simulations

The trajectories given by MD simulations can be used to calculate different properties relating to structural behavior. This analysis and its chemical interpretation is the major part of this thesis work.

3.2.1.4.1 Radial Distribution Function (RDF)

One of the most important properties extracted from MD simulation is the pair radial distribution function (RDF). It is a function, usually written as $g_{a..b}(r)$, which presents the probability of finding a particle of type *b* at a distance *r* from particle of type *a*. In a perfect crystal without thermal motion, RDF would appear as periodically sharp peaks, which gives information about the short-range order in the system.

RDF can be calculated by counting the number of atom pairs within some distance ranges, and averaging this over a number of time-steps and particle pairs:

$$g_{ab}(r) = \frac{\sum_{k=1}^{M} N_k(r_{ab}, \Delta r)}{M(\frac{1}{2}N)\rho V(r_{ab}, \Delta r)} \qquad (3.27)$$

where N_k is the number of atoms found at time k in a spherical shell of radius r and thickness Δr, and ρ is the average system density, N/V, of a given atom type.

Integrating this RDF over r gives the coordination number function (CNF), which is the average coordination number of particle type a to particle type b at distance r. RDF can be compared directly with experimental data from X-ray or neutral diffraction, and can thus be used as a check on the reliability of the potentials in many systems.

3.2.1.4.2 End-to-end Distance and Radius of Gyration

Since polymer molecules may in general assume an enormous number of spatial arrangements, descriptions of chain configuration are generally given in terms of statistical (ensemble) averages of some characteristic properties. Two examples of parameters used to specify average global configuration are the distribution and moments of the end-to-end distance and the radius of gyration. The end-to-end distance (r) of a single chain may be defined by:

$$r = \sum_{i=1}^{n} l_i \tag{3.28}$$

where l_i denotes the vector along backbone bond i, and n denotes the number of backbone bonds in the molecule. The radius of gyration (s) is defined as the root mean square distance of the atoms in the molecule from their common center of mass, that is,

$$s^2 = \frac{\sum_{i=1}^{N} m_i s_i^2}{\sum_{i=1}^{N} m_i} \qquad (3.29)$$

where s_i denotes the distance of atom i from the center of mass, and N denotes the total number of atoms.

In polymer science, the radius of gyration is used to describe the dimensions of a polymer chain. Since the chain conformations of a polymer sample are quasi infinite in number and constantly change over time, the "radius of gyration" discussed in polymer science must usually be understood as a mean over all polymer molecules of the sample and over time. That is, the radius of gyration which is measured is an *average* over time or ensemble. One reason that the radius of gyration is an interesting property is that it can be determined experimentally with static light scattering as well as with small angle neutron- and x-ray scattering. This allows theoretical polymer scientists to check their models against reality. The hydrodynamic radius is numerically similar, and can be measured with size exclusion chromatography.
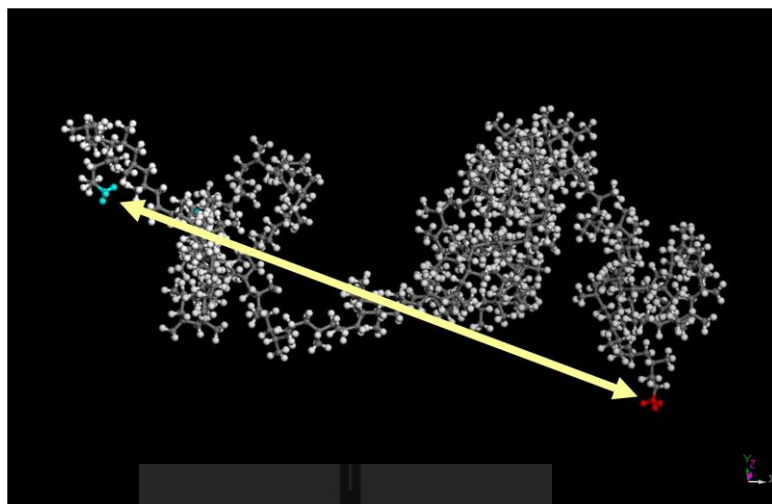
Figure 3.4 End-to-end distance.
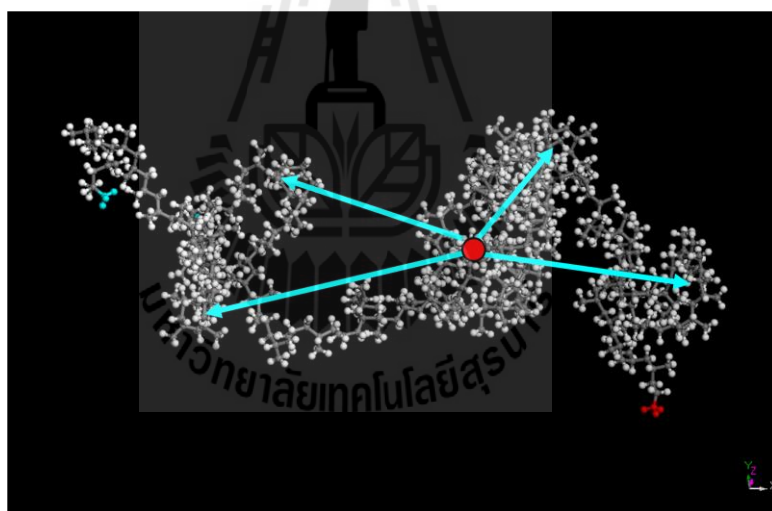
Figure 3.5 Radius of gyration.

3.2.1.4.3 Bond Angle and Dihedral Angle

Local chain geometry is frequently characterized by measurements of valence and dihedral angle distributions. The latter, whose values are essentially determined by a combination of packing effects and local intramolecular interactions are strongly correlated with global dimensions, and are often experimentally measurable.

In a chemically complex system such as $LiPF_6:PEO_6$, the average atomic distances calculated as RDF can be too rough measurement to capture all the structural information available. The spatial arrangement of atoms can also be of major interest, and can be obtained throughout by calculating bond angle and dihedral angle distributions in the crystallographic asymmetric unit. The total distribution of all bond and dihedral angles contains all the information we need on the polymer configuration. Figure 3.6 shows the geometry of a simple chain molecule.

Plotting especially the dihedral angles in this way gives group information for the simulated system, which can be related to the crystallographically determined space group. The appearance of new peaks indicates some new repeat unit.
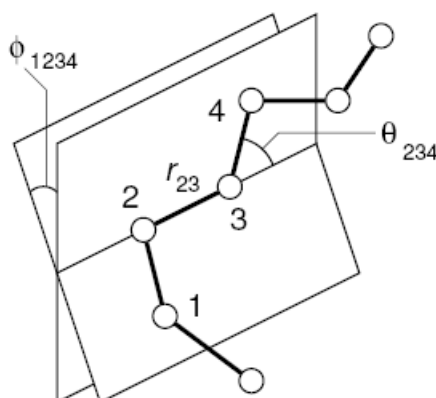
Figure 3.6 Geometry of a simple chain molecule, illustrating the definition of interatomic distance (r_{23}), bend angle (θ_{234}), and torsion angle (ϕ_{1234}) (Allen, 2004).

3.3 Monte Carlo (MC)

Monte Carlo simulation is the simulation technique that gathers samples in a random way. As the name implies, Monte Carlo simulation uses random numbers for making decision during the simulation. In terms of molecular mechanics, MC provides another way to explore a conformational space. While molecular dynamics can visit a conformational state in a deterministic way by solving Newtonian equations of state, MC simulation can find a conformational state in a stochastic way by generating random numbers.

With a given potential like Equation (3.30), the simulation involves a successive energy evaluation to make a decision for acceptance of a move attempt which is chosen randomly.

$$V_{total} = \underbrace{V(r)_{bond} + V(\theta)_{angle} + V(\phi)_{torsion} + V(\chi)_{out-of-plane}}_{V_{bonded}} + \underbrace{V(r)_{vdw} + V(r)_{elec}}_{V_{non-bonded}} \quad (3.30)$$

The decision is accomplished by Metropolis algorithm (Metropolis *et al.*, 1953) in the most cases, which has the following criteria.

$$\Delta E = V(r)_{new} - V(r)_{old} \leq 0 \qquad\qquad accepted$$

$$\Delta E = V(r)_{new} - V(r)_{old} > 0 \, AND \, \exp(-\Delta E/kT) \geq rand(0,1) \quad accepted \qquad (3.31)$$

$$\Delta E = V(r)_{new} - V(r)_{old} > 0 \, AND \, \exp(-\Delta E/kT) < rand(0,1) \quad rejected$$

If the new state is in a lower energy state, the new state replaces the previous state. If the new state is in a higher energy state, the decision is based on the energy difference between two states. For the decision procedure, MC simulation allows a system to move to higher energy state. The probability to overcome the higher energy barrier depends on the energy difference between the new attempt and the current conformation. By doing so, MC simulation explores the conformational space to calculate the ensemble averaged properties, while MD simulation deals with time averaged properties. Both averaged properties should be same through the ergodic hypothesis.

Much effort has drawn attention to increasing the computational efficiency of MC simulation. One of the efforts is to run the simulation on a lattice, which reduces the floating number calculation. Another way to gain speed in the MC simulation is to use an efficient move algorithm that allows the faster relaxation or equilibration. Many beads can move at a single move attempt. The computational time of the lattice simulation based on MC method is proportional to the power of 1 to 2 depending on the quality of the potential energy function.

3.3.1 Monte Carlo Simulation on a High Coordination Lattice

A coarse graining model in a lattice has the computational efficiency that comes from two seasons. The first one is the reduction of the evaluation of energy terms, which is generally proportional to the square of the number of particles because many energetic terms are two-body potentials. The second reason is that the position of particles during simulation can be stored as integers, which reduces the number of instructions done by a central process unit (CPU) and memory usage compared to the

real number operation in off-lattice simulation. As a result of the efficiency, the method enables running a simulation in a large scale, which is required for polymer simulation. As often is the case, the pros come with the cons. Due to the coarse graining, the detailed chemical information such as the chemical nature of the coarse-grained particle (bead) and the nature of bond between the two beads disappears. The drawback would not be an important issue when a polymer chain is expressed by a collective set of simple beads. In the bulk state of polyolefin, the simplification works well with only the topological consideration. The decoupling of the effect of the variables or the ruling-out of an effect of a variable using a computer simulation requires a detailed description of a polymer chain embodied in the simulation as well as its applicability to the large-scale system.

3.3.1.1 Coarse Graining into Rotational Isomeric State Model

Often the energy state of a molecule can be described by a sum of energetic contributions of internal coordinates and non-bonded interactions, as in Equation 3.30. Among them, the bond stretching and angle bending terms are so strong, because of large force constants, that they do not vary much with time, staying at the most probable bond length and bond angle. Since computational efficiency is indispensable for a polymer simulation, these two terms are neglected in most cases. Accordingly, a property of a polymer chain cannot be only dependent on the remaining energy terms, torsional energy and non-bonded energy. Furthermore, if a polymer chain is not perturbed by the existence of others, the importance of the long-range interaction is diminished. In that case, the partition function of a single chain

can be expressed by only torsional partition function or conformational partition function as follows.

$$Z = \int_{\phi_1}...\int_{\phi_n} \exp(\frac{-E_{\phi_1...\phi_n}}{kT})d\phi_1...d\phi_n \qquad (3.32)$$

Then, the average of a property, <A>, can be written as,

$$<A> = Z^{-1} \int_{\phi_1}...\int_{\phi_n} \exp(\frac{-E_{\phi_1...\phi_n}}{kT})A(\phi_1...\phi_n)d\phi_1...d\phi_n \qquad (3.33)$$

The continuous torsional states can be grouped to have several discrete states. This assumption is reasonable because discrete torsional states are separated by an activation barrier. The torsional states are called "Rotational Isomeric State (RIS)". With the discrete torsional states, the conformational partition function of Equation (3.30) can be rewritten as the summation over the discrete conformationals space.

$$Z = \sum_{\phi_1}...\sum_{\phi_n} \exp(\frac{-E_{\phi_1...\phi_n}}{kT}) \qquad (3.34)$$

The RIS model (Mattice and Suter, 1994) is a coarse grained model, which only considers the discrete rotational isomeric states with other internal coordinates frozen. Schematically, the mapping from a realistic chain to a RIS chain is illustrated in Figure 3.7. In this simulation for PEO chanis, which have (CH_2-CH_2-O) repeat

units, either one of CH$_2$ groups is represented as a single united atom as well as O atoms. In Figure 3.7, every second bead on the main chain, regardless of C or O, is taken out, and the remainder of united atoms is connected. In this particular kind of coarse-graining approach, every single bead has to be treated identically. There is no difference between C-O or C-C contacts in terms of the long-range (LR) interactions, but there exist a bit of ambiguity regarding the short-range (SR) interactions about which we will give details in the next sections.
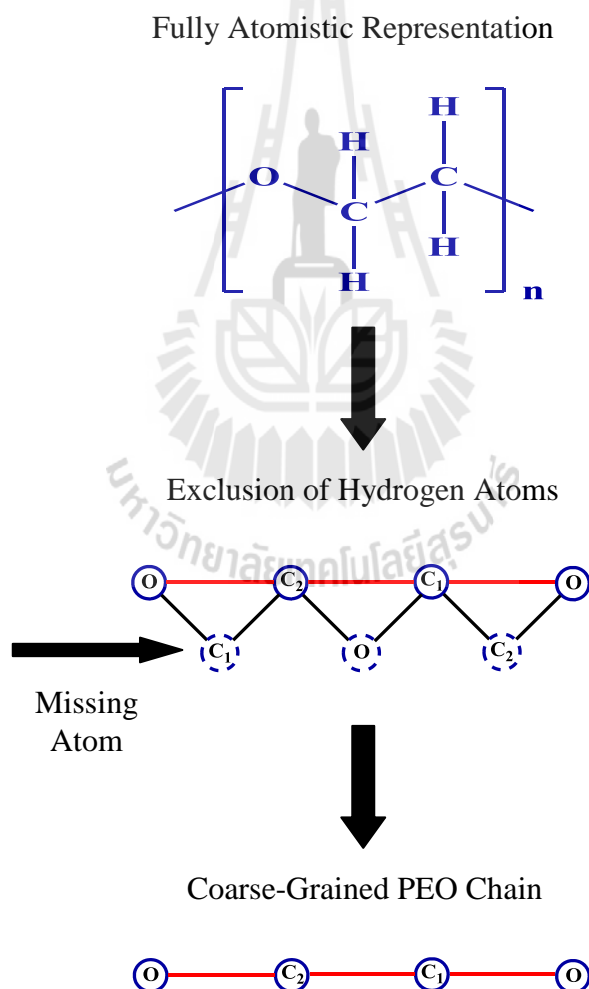
Figure 3.7 Example of the mapping of a real chain into lattice by coarse graining.

As shown in Figure 3.8, the 2nnd lattice can be considered a distorted cubic lattice with 60° between any two axes. Because of that, each lattice site of the 2nnd lattice can be assigned with integer numbers, which expedites the RIS calculations of interest. By the geometry, the 2nnd bond length (or step length) can also be calculated. The 2nnd lattice spacing, or step length, for a coarse-grained PEO chain is calculated as 2.39 Å (details of the calculation can be found in the following pages). When the melt density of PEO is satisfied at the simulation temperature (373 K), the 2nnd lattice has an occupancy value of 20%. It should be noted that, all of the simulations presented in this report are done for dense melt systems.

Fully Atomistic representation

Coarse-gained representation
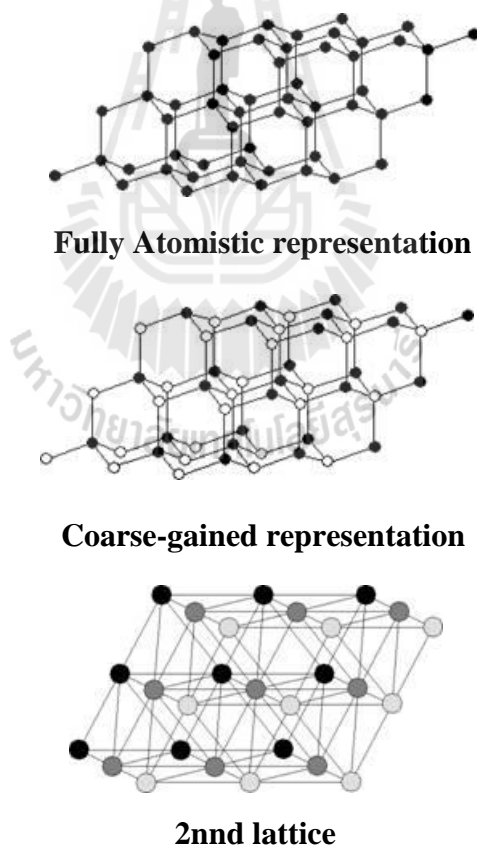
2nnd lattice

Figure 3.8 Graphical demonstration of how a tetrahedral lattice can be converted into a 2nnd lattice.

3.3.1.2 Short-Range intramolecular interactions

The short-range (SR) interactions basically enforce the local conformational preferences of the polymer chains. As emphasized before, the reproduction of realistic polymer chains on the 2nnd lattice necessitates the use of realistic interaction potentials. Compared to a simple random walk case, torsion potential energy functions for real chains are definitely far more complex. In this report, short range interactions are represented by a model based on RIS calculations.

The RIS model (Flory, 1988; Mattice and Suter, 1994) is very good at describing the conformational properties of the chain molecules. Therefore, Abe *et al.* calculated configuration-dependent properties of PEO chains by means of RIS calculations (Abe *et al.*, 1985). These calculations are based on a symmetric three-fold torsion potential with nearest neighbor interdependence. Along the main backbone of a PEO chain one can find three different types of bonds: C-C, C-O, and O-C. Thereby, each torsion potential in their RIS model representation is peculiar in the sense that each of them belongs to a certain bond family.

The RIS model is known to work properly to reveal the local characteristics of polymer chains. In addition, the diamond lattice is also considered a good candidate for on-lattice polymer simulations. Thus, the RIS approximation should be considered a good way to model PEO chains on the diamond lattice. However, in order to describe the short-range interactions on the 2nnd lattice properly, a mapping procedure, which will define the torsion angles in the real chains on the 2nnd lattice, is needed.

There are three available rotational isomeric states, which are trans (*t*), gauche$^+$ (g^+), and gauche$^-$ (g^+) for every single bond on the diamond lattice. As shown

in Figure 3.9, for a 9-atom polymer subchain there are 8 bonds on the tetrahedral lattice. With further coarse-graining, i.e. after switching to the 2nnd lattice, half of the bonds on the diamond lattice will disappear and there will be only four 2nnd bonds left. Although half of the diamond lattice bonds disappear on the 2nnd lattice, we still keep track of their information at every single step throughout the MC simulations.
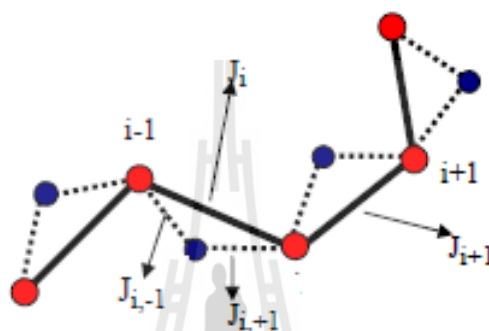
Figure 3.9 Schematic representation of 2nnd subchain composed of 4 coarse-grained bonds. The coarse grained bonds are represented by solid lines, whereas the dashed lines denote the corresponding real bonds on the underlying diamond lattice.

The RIS calculations are based on the probabilities of the rotational isomeric states of pairs of bonds on the main backbone. By combining the probabilities of the entire amount of rotational isomeric states, the probability of a certain multi-chain system can be calculated. As described in the previous paragraph, there exists an independent rotational isomeric state associated with each single bond. Each bond may be represented by one of t, g^+, or g^- states. On the 2nnd lattice however, there will be only a coarse-grained single bond, whose rotational isomeric state is defined by that of former two tetrahedral bonds. For example, if the two corresponding rotational isomeric states of the two diamond-lattice bonds are g^+ and g^-; then the

resulting 2nnd bond's rotational isomeric state will be defined by a double rotational isomeric state representation like "g^+g^-" instead of a single representation. In that sense, every single rotational isomeric state on the 2nnd lattice may have triple more possibilities (tt, tg^+, tg^-, g^+t, g^+g^+, g^+g^-, g^-t, g^-g^+, g^-g^-) when the torsions on the underlying diamond lattice are considered. The probability of a specific multi-chain system can be calculated in this way with the aid of the mapping technique. In particular, a more detailed explanation of this mapping technique for polymer chains with (A-A-B) type of repeat unit, e.g. PEO, can be found.

Next, we present the related statistical weight matrices that determine the local conformation of the PEO chains used in the MC simulations (Doruker *et al.*, 1996). In the following three matrices, the rotational isomeric states of bonds $J_{i,-1}$ and $J_{i,+1}$ are represented by the rows and columns, respectively. There are three different statistical weight matrices, each representing a specific bond type. $\sigma_{C\text{-}C}$ and $\sigma_{O\text{-}O}$ are the statistical weights for the C-C and O-O type first-order interactions. $\omega_{C\text{-}C}$ and $\omega_{C\text{-}O}$ correspond to the second-order interactions. These numbers are calculated as the Boltzman factors (exp ($-E/RT$)) of the associated energy values listed in Table 3.1.

$$
U_{C\text{-}C} \quad = \quad
\begin{array}{c}
 \\
t \\
g^+ \\
g^-
\end{array}
\begin{array}{c}
t \qquad\quad g^+ \qquad\qquad g^- \\
\left(
\begin{array}{ccc}
1 & \sigma_{O\text{-}O} & \sigma_{O\text{-}O} \\
1 & \sigma_{O\text{-}O} & \sigma_{O\text{-}O}\omega_{C\text{-}O} \\
1 & \sigma_{O\text{-}O}\omega_{C\text{-}O} & \sigma_{O\text{-}O}
\end{array}
\right)
\end{array}
\qquad (3.35)
$$

$$
U_{C\text{-}O} \quad = \quad
\begin{array}{c}
 \\
t \\
g^+ \\
g^-
\end{array}
\begin{array}{c}
t \qquad\quad g^+ \qquad\qquad g^- \\
\left(
\begin{array}{ccc}
1 & \sigma_{C\text{-}C} & \sigma_{C\text{-}C} \\
1 & \sigma_{C\text{-}C} & \sigma_{C\text{-}C}\omega_{C\text{-}O} \\
1 & \sigma_{C\text{-}C}\omega_{C\text{-}O} & \sigma_{C\text{-}C}
\end{array}
\right)
\end{array}
\qquad (3.36)
$$

$$U_{O-C} = \begin{array}{c} \\ t \\ g^+ \\ g^- \end{array} \begin{array}{ccc} t & g^+ & g^- \\ \left(\begin{array}{ccc} 1 & \sigma_{C-C} & \sigma_{C-C} \\ 1 & \sigma_{C-C} & \sigma_{C-C}\omega_{C-C} \\ 1 & \sigma_{C-C}\omega_{C-C} & \sigma_{C-C} \end{array} \right) \end{array} \qquad (3.37)$$

Table 3.1 First- and Second-order local interactions on the 2nnd lattice for PEO chains: a RIS model approximation.

Interaction	(kJ/mol)
$E\sigma_{C-C}$	3.2
$E\sigma_{O-O}$	-2.2
$E\omega_{C-C}$	∞
$E\omega_{C-O}$	2.2

In summary, the rotational isomeric state of any 2nnd bond can be defined by those of its corresponding tetrahedral lattice bonds $J_{i,+1}$ and $J_{i,-1}$. For instance, if the 2nnd bond J_i in Figure 3.9 is a *C-C* type of a bond and the states of the real bonds $J_{i,-1}$ and $J_{i,+1}$ are g^+ and g^-, the resulting statistical weight of the 2nnd bond J_i will be equal to U_{C-C} [2,3], which is $\sigma_{O-O}\omega_{C-O}$. The values of the statistical weights σ_{O-O} and ω_{C-O} can be determined by substituting their related energy values, the simulation temperature, and the universal gas constant into the Boltzman factor. Obviously, the simulation temperature and the universal gas constant are pre-known parameters. So, the substitution of the true matrix element is the key point to the determination of the corresponding statistical weight of the bond J_i. Consequently, the same procedure is

followed for all of the coarse-grained beads in the system. The combination of those leads to the configurational probability of the overall system.

3.3.1.3 Long-range Interactions

The incorporation of the rotational isomeric state model is not enough to describe the energetics of the melt system because the RIS model is a single chain model in the unperturbed state, θ state. The model only accounts for the short-range intermolecular interaction up to next nearest neighbor bonds on the 2nnd lattice. For the remaining long-range intramolecular and intermolecular interaction, the Lennard-Jones pair potential, $u(r)$, seems to be a reasonable choice since there are only dispersive interactions in a polyethylene melt. Including the long-range interaction, the total energy which will be used in Metropolis evaluation will be

$$E_{total} = E_{RIS} + E_{LJ} \tag{3.38}$$

The lattice representation of the continuous Lennard-Jones potential at the ith shell, u_i, is obtained from an averaged Mayer f-function which is used for the description of the second virtual coefficient of a non-ideal gas. The interaction parameter at the ith shell is defined through following equation.

$$\exp(-\frac{u_i}{k_B T}) - 1 \equiv \bar{f}_i \tag{3.39}$$

The average Mayer f-function at the ith shell, f_i, is obtained by integrating $u(r)$ over the cells in the ith shell.

$$\bar{f_i} = \frac{\int_{cell} f dr}{\int_{cell} dr} \qquad (3.40)$$

$$f = \exp(-\frac{u(r)}{k_B T}) - 1 \qquad (3.41)$$

The set of the interaction parameters for 2nnd beads is derived from the Lennard-Jones potential for a methyl ether molecule (CH_3-O-CH_3). Table 3.2 gives a set of interaction parameters obtained by the averaging method. The details about the long-range interaction is given by Cho and Mattice (1997).

Table 3.2 Long-range interaction shell energy obtained from the averaging process.

Shell	Shell energy (kJ/mol)[a]
1	8.113
2	-0.213
3	-0.339
4	-0.067
5	-0.017

[a]In this example, the used LJ parameters are $\sigma = 3.76$ Å and $\mathcal{E}/k = 154$ K

and the interaction shell energies are derived at 373 K.

The single bead move is always employed in this study with the restriction that a chain cannot pass through itself, as in a self-avoiding random walk. A randomly chosen bead can move to a vacant site in the first shell when the attempt does not change the bond length to its two bonded neighbors. Even though the relaxation or equilibration of a system is quite slow with the single bead move, the move provides the reliable dynamic properties at the time scale of Monte Carlo step (MCS). One MCS is defined as the simulation length when every bead in the system has attempted one move, on average.

CHAPTER IV

APPLICATION OF X-RAY ABSORPTION

SPECTROSCOPY AND MOLECULAR SIMULATION TO

STUDY THE SOLVATION STRUCTURE OF

POLYMER:KSCN ELECTROLYTES

4.1 H_2O:KSCN

In this work, MD (Molecular Dynamic) simulation, Extended X-ray Absorption Fine Structure (EXAFS) spectroscopy, and the combination of MD simulation and EXAFS called "MD-EXAFS" method are employed to determine the atomistic solvation structures of H_2O:KSCN system which is the simplified models for polymer electrolytes. This model would give the information on the solvation structure around the solute ions which is the first step to understand a more complicated polymer electrolyte system. Although the structure of solvated ions is not as well-defined as in the case of crystals, one can still define an average structure, which is quite the characteristic of ion and its immediate environment.

In general, structural parameters can be calculated from experimental measurements, *ab initio* electronic structure calculation or numerical simulations such as MD. Figure 4.1 gives a qualitative picture of these structural parameters, the coordination number of the nearest neighbors (N), Debye-Waller factor (σ^2),

which corresponds to half-width of the peak in radial distribution function, $g_{ij}(r)$; and the average distance between the central absorbing atom (*i*) and surrounding atoms (*j*), which corresponds to the center of peak, R_0. The broken line depicts the (ideal) Gaussian peak centered at $R_{0,G}$, which in general, can be more symmetric and narrower than the real peak. This center is shifted compared to the one obtained experimentally, or even from MD simulations. The coordination number can be calculated by a direct integration of this first peak:

$$N = \rho \int_{r_1}^{r_2} 4\pi r^2 g_{ij}(r) dr \tag{4.1}$$

where r_1 and r_2 are the integration limits.
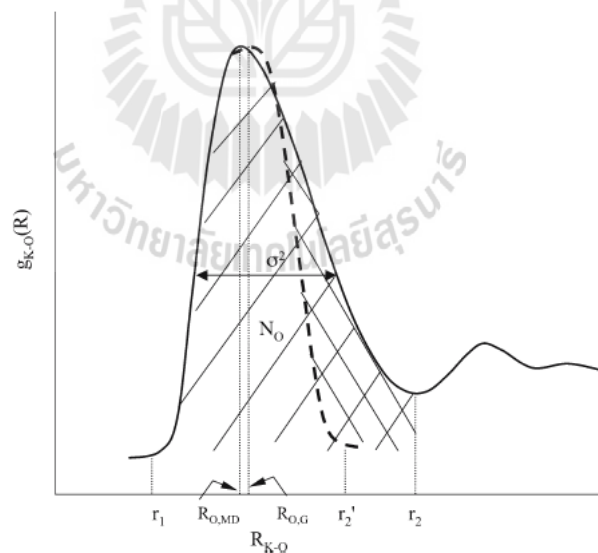
Figure 4.1 The fundamental quantities of ion solvation structure, coordination number N_0 (*area under curve*), Debye-Waller factor (half-width) σ^2, center of peak, R_0 (Glezakou *et al.*, 2006).

4.1.1 EXAFS Measurement and Data Analysis

The experimental potassium *K*-edge XAS spectra was measured at beamline BL-8 of Synchrotron Light Research Institute (Public Organization) at Nakhon Ratchasima, Thailand. The ring current was 100 mA, and the ring energy 1.2 GeV. The data was collected in Fluorescent mode (Lytle detector) using a Si(111) double crystal monochromator. A 2 eV step was used in the pre-edge region and EXAFS region, while 0.5 eV step was employed from 60 eV below the edge to 60 eV above the edge. Energy calibration was performed with the standard anhydrous KI compound. A total of 3 scans were collected and the scans were averaged after E_0 determination before further data analysis to improve the signal to noise ratio. The EXAFS data processing was carried out with ATHENA software (Ravel and Newville, 2005). Phase shift and backscattering amplitudes were calculated by FEFF7.0 software (Rehr and Albers, 2000). The EXAFS data were Fourier transformed over the ranges $2.0 < k < 8.0$ with k^2 weighting.

Clusters were obtained from each configuration by extracting all species that fell within 5 Å radius of potassium ion. Each cluster was then used as the input for FEFF7.0, to calculate the EXAFS spectrum ($\mu(E)$) as a function of energy *(E)*, using a multiple scattering approach. The resulting spectra were then averaged together to get a configurationally averaged absorption coefficient $\overline{\mu}(E)$. $\overline{\mu}(E)$ is actually a combination of the background absorption coefficient, $\mu_0(E)$, and EXAFS oscillations, $\chi(E)$. The EXAFS oscillations can be extracted from $\overline{\mu}(E)$ by the formula

$$\bar{\chi}(E) = \frac{\bar{\mu}(E) - \mu_0(E)}{\Delta\mu_0(E_0)} \qquad (4.2)$$

where $\Delta\mu_0(E_0)$ is the jump in the absorption background at the absorption edge E_0. FEFF7.0 provides $\chi(E)$ directly for each cluster, so $\bar{\chi}(E)$ can be obtained directly by averaging individual $\chi(E)$.

The EXAFS oscillations, $\chi(k)$, were mapped from photoelectron energies to wavenumbers by $h^2k^2/2m = E - E_0$, where E_0 is the absorption threshold energy. An analysis of $\chi(k)$ function was based upon the standard EXAFS relationship

$$\chi(k) = \sum_i \frac{N_i}{kR_i^2} F_i(k) e^{-2\sigma_i^2 k^2} e^{-2R_i/\lambda} \sin[2kR_i + \varphi_i(k)] \qquad (4.3)$$

where N_i is number of neighboring atoms in the ith coordination shell at a distance (R_i) away from the absorbing atom. The backscattering amplitude and mean-squared displacement of neighboring atoms are given by $F_i(k)$ and σ_i, respectively. The phase shift of the photoelectron is given by $\varphi_i(k)$, while the exponential term containing the mean free path (λ) of the photoelectron accounts for their inelastic scattering. In order to obtain a real-space representation of the EXAFS spectra, Fourier transform of $\chi(k)$ function is calculated as implemented in FEFFIT package (Newville *et al.*, 1995). Equation (4.3) is thus transformed to:

$$\widetilde{\chi}(R) = \frac{1}{\sqrt{2\pi}} \int_0^\infty k^2 \overline{\chi}(k) W(k) e^{i2kR} dk \qquad (4.4)$$

where $W(k)$ is Hanning window.

4.1.2 Molecular Dynamic (MD) Simulations

MD simulations were carried out on a system consisting of 200 H_2O molecules plus 10 K^+ and 10 SCN^- ion in a cubic simulation box with the cell length determined from the density of ~1.0 g/cm^3. Periodic boundary conditions were applied in all three spatial directions. MD simulations were performed at 300 K, using the Amorphous Cell module in Materials Studio 4.2 simulations package provided by National Nanotechnology Center, Thailand. The COMPASS forcefield which is the first *ab initio* forcefield was used. After energy minimization, MD simulations were initially performed in NPT ensemble at 400 K for a few ns to obtain a new equilibrium density. Further equilibrations of approximately 1 ns were run in NVT ensemble. For data analysis, atomic trajectories were collected for another 1 ns.

Table 4.1 Charge parameters used in the simulation.

atom	q (e)	atom	q (e)
K	+1.000	O_w	-0.848
S_{SCN}	-0.560	H_w	+0.424
C_{SCN}	0.140		
N_{SCN}	-0.580		

4.1.3 Results and Discussion

4.1.3.1 SCN⁻ Hydration Shell

According to chemistry textbooks, the negative charge of SCN⁻ is equally distributed on the S and N sites and consequently it is an ambidentate ligand, which can coordinate cations or water molecules at both ends. The effective potential model (Vincze *et al.*, 2001) available in the literature indicates a small charge difference between the S and N site. Despite such small difference, our data suggest a clear asymmetry between the hydration shells of the two atomic sites, as shown in Figure 4.2. As a matter of fact, the first H_w-S peak is at $r = 2.2$ Å and this distance looks far too long in order to achieve hydrogen bonding between hydrogen and sulfur atom.

Conversely, the first peak of $g_{NHw}(r)$ is at 1.9 Å and the first peak of $g_{NOw}(r)$ is about 1 Å apart, suggesting that nitrogen atoms form a typical hydrogen bond with surrounding water molecules. Integration over the first peak of $g_{NH}(r)$ gives a coordination number ~2.0. Importantly, preferential H-bonding at the N site has been previously reported in aqueous solutions of NaSCN. These earlier experimental works

(Mason *et al.*, 2003; Kameda *et al.*, 1994) were not supported by an atomistic simulation and consequently the individual site-site contributions to the total radial distribution functions were not separated; as a result, a single broad peak at about 2 Å was identified due to H-bonding at the N site of SCN⁻ ion. From our results, water molecules are likely H-bonded to the N site and weakly coordinated with the S site as also suggested by the sharpness of the first peak of the $g_{NH}(r)$ and broad peak of the $g_{SHw}(r)$. Both $g_{COw}(r)$ and $g_{CHw}(r)$ show a very broad first peak, at higher distances, $r \approx 3.4$ Å, compared to the other site-site RDFs, suggesting that the C site is less accessible to water molecules.

From the work of Botti *et al.* (2009), the Empirical Potential Structure Refinement (EPSR) code was used to identify the peak at 3.0 Å as due to the correlation between water oxygen and nitrogen different from a standard hydrogen bond due to its primarily Coulombic nature. All RDFs and probability isosurfaces do not show significant dependence on solute concentration, suggesting that the egg-shaped hydration shell of the anion (Figure 4.3) is a stable feature of these solutions. However there is an asymmetry between the top and bottom of this hydration shell, because our data suggest that water molecules form a H-bond with the N site (top), and are instead weakly coordinated with the S site (bottom).
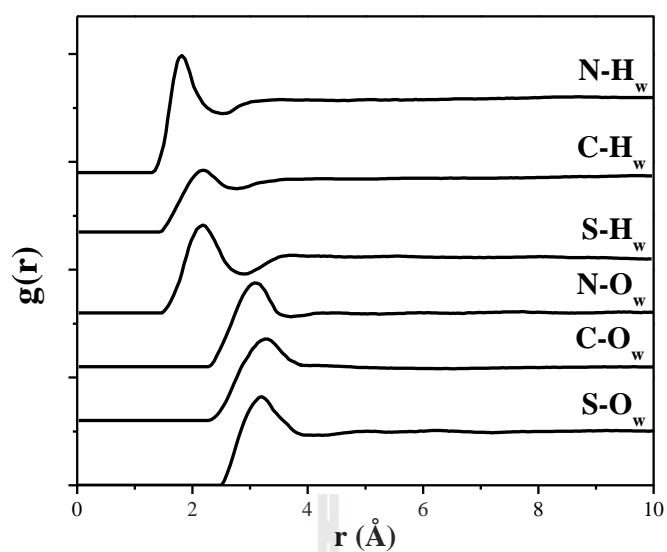
Figure 4.2 The anion hydration site-site RDF for the individual SCN⁻-water atomic pairs at all the investigated solutions. Data have been shifted for clarity.
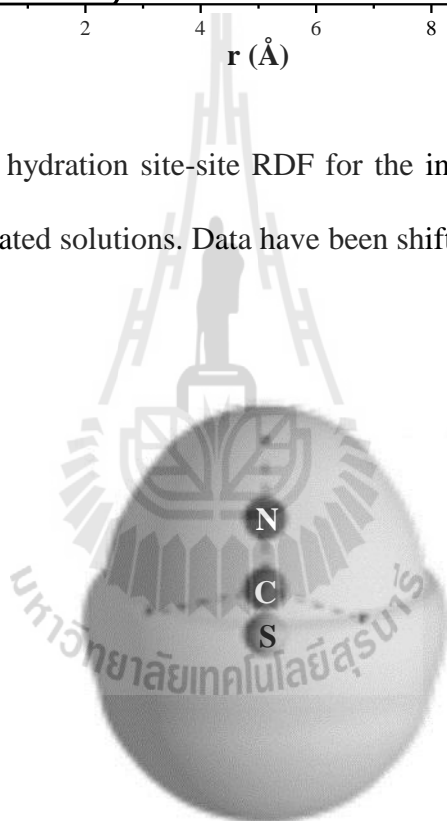
Figure 4.3 The spatial distribution functions (SDFs) for water around and SCN⁻ ion. The S atom is represented as a light gray sphere, the C atom as a middle gray sphere, the N atom as a dark gray sphere (Botti *et al.*, 2009).

The SCN⁻ ion shares with OH⁻ the asymmetric character of the hydration shell. Both ions have indeed H-bonded water molecules at one site and weakly correlated water molecules at the opposite site. They are strongly bonded to water at one extreme and in virtue of this can induce distortion to the water network, while the other extreme can easily loose its hydration water and be exposed to a solute. We notice however that the N-H bond-length, 1.8 Å, is larger than the H-bond length found in the case of OH⁻, 1.4 Å (Imberti *et al.*, 2005), although compatible with chemical literature (Jeffrey, 1997).

4.1.3.2 K⁺ Hydration Shell

For KSCN aqueous solution, RDFs between K⁺ and all other species (O_w, H_w, N, S and C) were calculated and plotted together in Figure 4.4. The simulated peak positions (R_0) and N calculated from the first peaks of all RDFs are summarized in Table 4.2. Each K⁺ cation is coordinated by ~5.7 oxygens (K⁺-O distance 2.65 Å) and ~17.6 hydrogens (K⁺-H distance 3.31 Å). This is consistent with MD technique with polarized forcefield reported by Dang *et al.* (2006) and from the recent MD simulation as well as experimental measurements (Marcus, 1988; Botti *et al.*, 2009), respectively. K⁺-O distance and coordination number from our MD simulation are also in good agreement with the recent *ab initio* dynamic simulation where values of 2.80 Å and 6.0-6.8 are reported (Rempe *et al.*, 2004; Fulton *et al.*, 2003). The negative charges of SCN⁻ anion are equally distributed on S and N sites and consequently it is an ambidentate ligand, which can coordinate cation or water molecules at both ends. The effective potential model (Botti *et al.*, 2009) available in the literature indicates a small charge difference between the S (-0.5600e) and N

(-0.5800e) site. RDF between K^+ and SCN^- anion (Figure 4.4(b)) exhibit the first K^+-N, K^+-S and K^+-C_{SCN} peak at 3.15, 3.22 and 3.34 Å, respectively. Both nitrogen and sulfur atoms are less likely to coordinate with K^+ compared to oxygen because *N* of solvated K^+ with anion is very small (0.3) compared to that of K^+-O (5.7). Therefore, to compute MD-EXAFS spectra of H_2O:KSCN solution, there is no need to include anion for further calculation. Figure 4.5 displays the example of cluster extracted from MD trajectory. There are about six water molecules surrounding one potassium cation. The position of oxygen atoms in the solvation structures is quite symmetric and hydrogen atoms prefer to point away from the symmetric K^+-O axes.
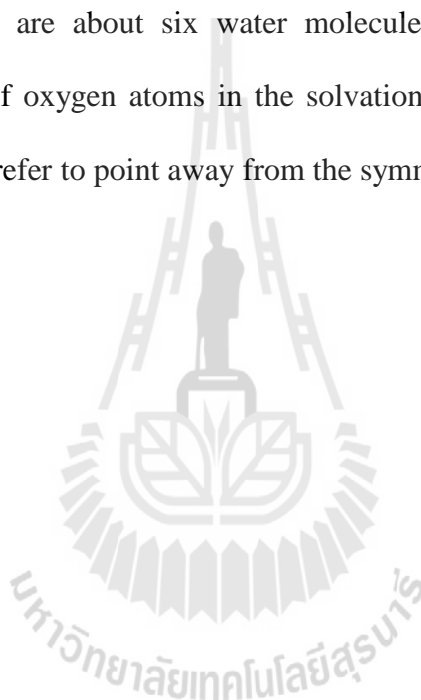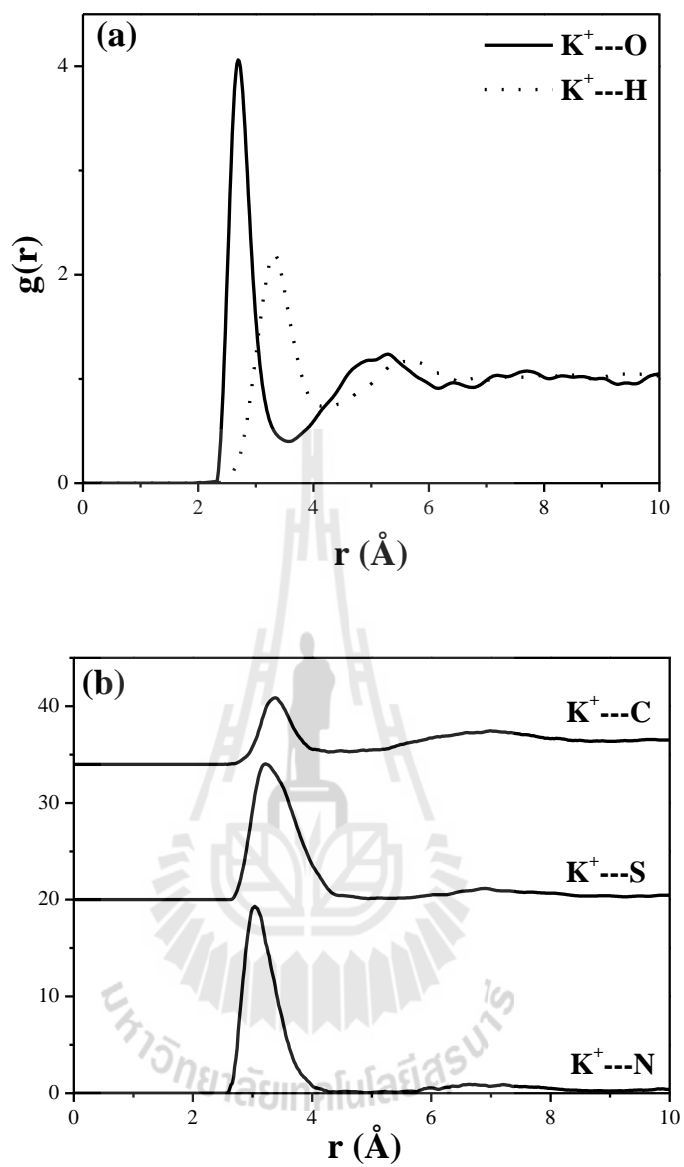
Figure 4.4 Radial distribution functions of $H_2O:K^+$.
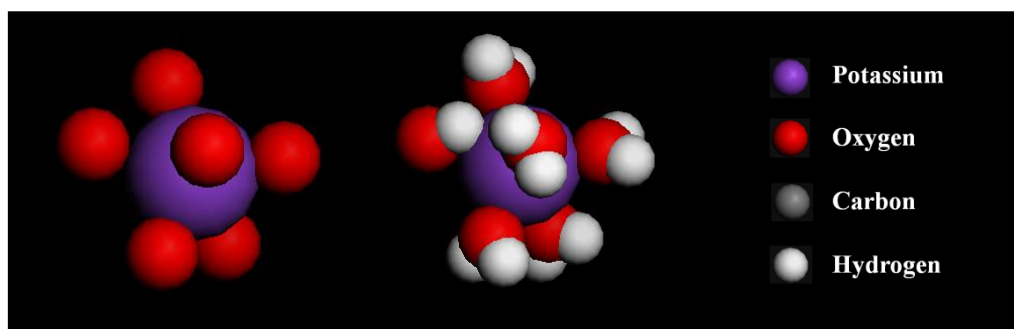
Figure 4.5 Model of potassium ion in water.

Table 4.2 Parameter characterizing the first peak of RDFs determined from MD.

Correlation	H$_2$O:KSCN					
	R$_0$ (Å)	N	R$_0$ (Å)[a]	N[a]	R$_0$ (Å)[b]	N[b]
K$^+$-O$_w$	2.65	5.7	2.6	5.9	2.77	5.7
K$^+$-H$_w$	3.31	17.6	3.4	-	-	-
K$^+$-N$_{SCN}$	3.15	0.3	~ 3.0	~ 0.2	-	-
K$^+$-S$_{SCN}$	3.22	0.3	~ 3.1	~ 0.2	-	-
K$^+$-C$_{SCN}$	3.34	0.3	~ 3.2	-	-	-

[a]Botti *et al*. (2009)

[b]Dang *et al*. (2006)

4.1.3.3 EXAFS Spectra and MD-EXAFS prediction

Selected 100 configurations of potassium aqueous solution from MD trajectories were taken into account for MD-EXAFS analysis. For each configuration, a cluster of the surrounding molecules within 5 Å to the photoelectron source (K^+) were extracted to form an input for electron multiple scattering analysis in FEFF.

In Figure 4.6(a), the k^2-weighted $\chi(k)$ experimental data from potassium aqueous solution is compared to both MD-EXAFS spectra with and without hydrogens. The MD-EXAFS spectrum calculated from the system with hydrogens is far from satisfactory as the amplitude of $\chi(k)$ oscillation is too low. The effect of adding hydrogens on the calculated EXAFS spectra of cation hydration systems has been explained previously in literature (Palmer *et al.*, 1996; Merkling *et al.*, 2003). The inclusion of hydrogen atoms proved necessary for obtaining a realistic backscattering potential but led to a sensible degradation of the spectrum when they were included as backscatterers. Hydrogens distort the calculation of the background $\mu_0(E)$ quite severely, apparently due to their effect on the muffin-tin radius of the potential of the absorbing atom, but do not have as large an effect on $\chi(k)$. It turns out that the spectrum calculated without hydrogens does a much better job of reproducing the number of nearest neighbors.

EXAFS spectra from experiment and MD simulation which left all the hydrogens out of the configurations show an overall good agreement for the frequency and the amplitude of the oscillations over the full k range. Matching of the frequency of oscillations means that the K^+-O distances are nearly the same. The corresponding $\tilde{\chi}(R)$ plots derived from experimental measurements are shown in Figure 4.6(b), together with the computed generated ensemble (MD-EXAFS). The

$\widetilde{\chi}(R)$ was generated by Fourier transform of the $k^2\chi(k)$ data, and they represent the partial pair distribution functions convoluted with the photoelectron scattering functions from Equation (4.3). Again, there is a remarkably good agreement in the radial structures of experimental and simulated data. It is important to realize that $\widetilde{\chi}(R)$ are not exact representations of $g_{KO}(r)$ (Guillaume, 2005). The K-O phase shift function, $\varphi_{KO}(k)$ in Equation (4.3) alters the phase of the scattered photoelectron leading to significant broadening and an *R*-shift of the K-O peak in Fourier transformed $k^2\chi(k)$ data. The exclusion of anion atoms proved that KSCN is completely dissociated. These results can be confirming by potassium coordination number with anion which is quite low and negligible (*N*=0.3).
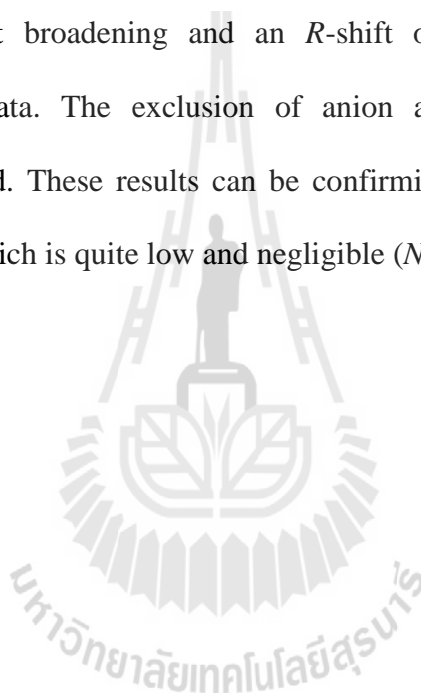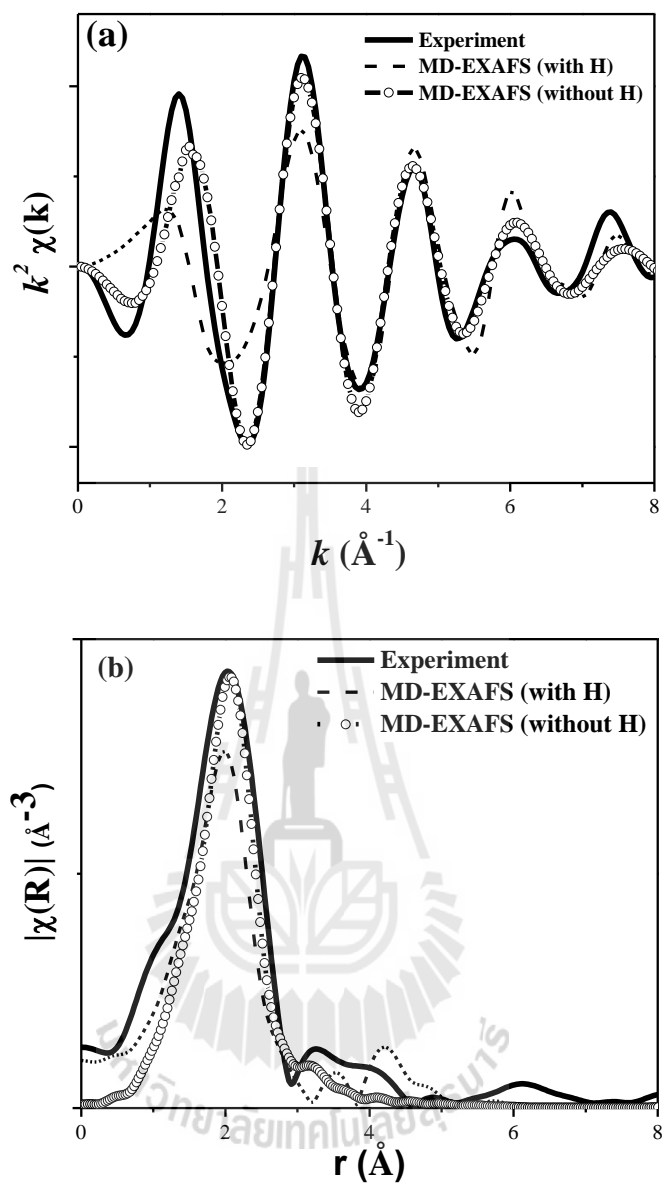
Figure 4.6 Comparison (a) $k^2\chi(k)$ and (b) $|\tilde{\chi}(R)|$ from experiment and MD simulation for potassium aqueous solution.

4.2 Poly(vinyl alcohol):KSCN (PVA:KSCN) Electrolyte

Poly(vinyl alcohol) (PVA) is one of the most important polymeric materials as it has many applications in industry and relatively low cost. Most of the commercial PVA samples have been prepared by hydrolyzing poly(vinyl acetate). Due to a presence of hydroxyl group, hydrogen bond between the PVA chains are developed. This causes a high melting point and good mechanical stability. In PVA:KOH systems (Mohamad *et al.*, 2003; Yang, 2004) possessing a conductivity level of 10^{-2} - 10^{-4} Scm^{-1} at room temperature, which highly depends on the composition of electrolyte, has been prepared. XRD analysis reveals that KOH disrupts the crystalline nature of PVA-based polymer electrolytes and converts them to an amorphous phase, which enhances their ionic conductivity.

In the past few years, Molecular Dynamics (MD) simulations have become a powerful tool to evaluate such structural and dynamic properties for polymer system. Karlsson (Karlsson, 2002) have performed MD simulations of atactic poly(vinyl alcohol) system built from a chain with 145 repeating units. The simulation results were compared with pressure-volume-temperature data, solubility parameter, X-ray scattering pattern and the characteristic ratio. X-ray scattering experiment data can be compared with the Fourier transformed of the radial distribution function. The results show peaks at ~1 Å and ~1.5 Å corresponding to bonded (H-C and H-O) hydrogen atoms and C-O and C-C bonds, respectively. The non-bonded curve is zero and starts to grow around 2 Å this corresponds to the hydrogen bond between oxygen and hydrogen. The purpose of this part is to employ the EXAFS spectra and MD simulations to determine the structural quantities such as distance and coordination numbers for PVA:KSCN electrolytes.

4.2.1 EXAFS Experimental Details

Potassium K-edge (3608.4 eV) EXAFS spectra were collected at X-ray Absorption Spectroscopy beamline 8 (BL8), Synchrotron Light Research Institute (Public Organization), Thailand. The EXAFS measurements were done at K^+:O = 1:20 of PVA:KSCN electrolytes.

4.2.2 Computational Details

MD simulation was carried out on a system consisting of 10 K^+SCN^- and 50 PVA $[CH_2CH(OH)]_8$ chains in a cubic simulation box with linear dimensions roughly of 20 Å. Periodic boundary condition was applied in all three spatial directions. After energy minimization, MD simulations were initially performed in NPT ensemble at 300 K for 1 ns to obtain a new equilibrium density. Further equilibrations of approximately 1 ns were run in NVT ensemble. For data analysis, atomic trajectories were collected for another 1 ns. The MD-EXAFS spectra were averaged over the 100 configurations. For each configuration, a cluster of all atoms that fell within a 5 Å radius of the potassium ion was extracted to form an input for electron multiple scattering analysis.

Table 4.3 Charge parameters used in the simulation.

atom	q (e)	atom	q (e)
K	+1.000	C_{PVA}	+0.300
S_{SCN}	-0.560	O_{PVA}	-0.700
C_{SCN}	0.140	H_{PVA}	+0.400
N_{SCN}	-0.580		

4.2.3 Results and discussion

To validate MD simulation for PVA system, thermodynamic and structural properties are reported and compared with experiment.

4.2.3.1 Cohesive energy and solubility parameters

The cohesive energy density is the amount of energy needed to completely remove unit volume of molecules from their neighours to infinite separation (an ideal gas), which is equal to the heat of vaporization divided by molar volume. In this calculation, the cohesive energy, U_{coh}, is the energy associated with the intermolecular interactions only and can be estimated by taking a difference between total energy of the microstructure, U_{tot}, and that of the isolated parent chain, U_{par}. In order to determine the parent-chain energy, the cube edge length was simply set to very large value so that the chain was fully enclosed in the box and did not interact with its images. Hildebrand's solubility parameter (δ), is the square root of the cohesive energy density, as following

$$\delta \;=\; \sqrt{\frac{\left(U_{par}-U_{tot}\right)}{V}} \;=\; \sqrt{\frac{U_{coh}}{V}} \tag{4.5}$$

where V is the volume of the cell. The average Hildebrand solubility parameter of PVA is $\delta = 25.5$ $(J/cm^3)^{1/2}$. The reported experimental value for the solubility parameters of PVA (Barton, 1991) is 25-27 $(J/cm^3)^{1/2}$, in good agreement with the estimated results.

4.2.3.2 Chain Conformation

Experimental studies of PVA:salt complexes such as vibrational spectroscopy and XRD (Bhargav *et al.*, 2009; Mohamad *et al.*, 2003) show that the conformation of PVA chains is altered upon complexation of metal salts. This characteristic can be considered by the distribution of dihedral angles population of PVA chains. To examine the conformation of PVA chains, the time-averaged population density distributions of backbone dihedral angles (θ) around C*-C bonds (Figure 4.7) were calculated from MD simulation trajectories. This analysis provides more detailed information about PVA chains and supplements the preceding chain dimension calculations. Dihedral angles around C*-C bonds for uncomplexed PVA and PVA:KSCN are compared in Figure 4.8. For pure PVA, there are three peaks: with two smaller peaks at two ends centered around 68° and 293° and between them a large peak centered around 181°. Similar results study by using Rotational Isomeric States (RIS) and 2,4-pentanediol as a model compound for PVA give dihedral angles at $\phi_t = 185°$, $\phi_{g+} = 65°$ and $\phi_{g-} = 290°$ (Wolf and Suter, 1984). The corresponding fractions were calculated and compared in Table 4.4. The fractions of *trans* conformation around the C*-C bond are in good agreement with the molecular modeling of isotactic PVA (De La Rosa *et al.*, 2002), $f_t^{C*C} = 0.65$, $f_{g^+}^{C*C} = 0.19$ and $f_{g^-}^{C*C} = 0.16$.

Dihedral angles distribution of PVA:KSCN along C*-C bonds show small difference compared to pure PVA. The population of both g^+ and g^- conformations slightly increases (~16 and ~7%) relative to those of pure PVA while *t* state slightly

decreases (~4%). This means that PVA backbone adopt a relatively lower-energy *gauche* conformation which oxygen atoms in side chains coordinated with K^+.
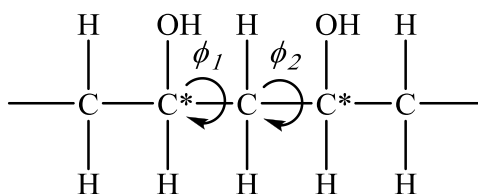
Figure 4.7 Atom sequence in PVA.

Main-chain dihedral angles, ϕ_1 and ϕ_2, are measured in the right-handed or left-handed sense, depending on the stereochemical character of the diad along C-C*-C-C*-C PVA chain sequence. The two dihedral angles are around C*-C, C-C* and their dihedral angles favor g^+ (or g^-) and t, respectively. Therefore, the most probable diads for pure PVA should be g^+t and g^-t (in this case, g is used to represent either g^+ or g^-). Populations of PVA diads in pure PVA and in PVA:KSCN are also shown in Figure 4.9. In both systems, the *gt* conformation is predominant. The total population of *gt* in pure PVA (43.0%) is lower than in PVA:KSCN (48%). The preference for the *gt* conformation in PVA:KSCN indicates that the K^+-O complexation favors this local chain conformation. It can be easily understood that a *gauche* angle around the C*-C bond enables oxygens to coordinate with K^+, and the t state implies a further distance between the side chain and the K^+ which thus lowers the repulsion. For PVA:KSCN, *tg* and *tt* conformations have the second (36.0%) and third largest (7.0%) populations.
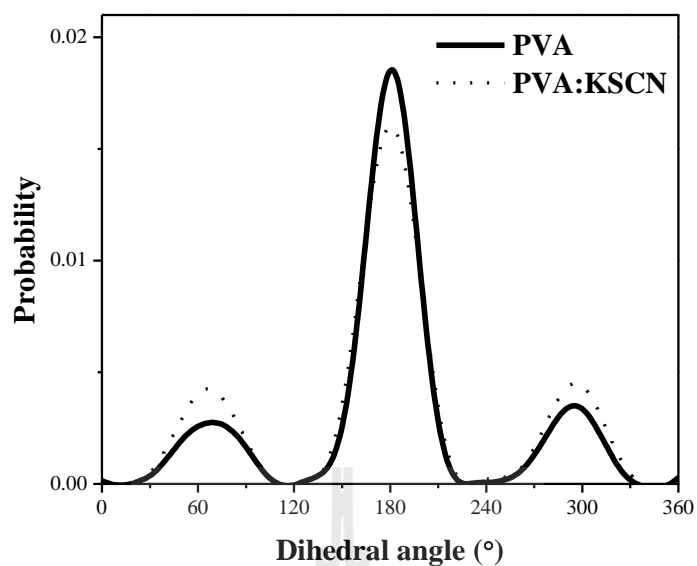
Figure 4.8 Average population density distributions of PVA backbone dihedral angles around C*-C bond.

Table 4.4 The population of *gauche*$^{\pm}$ and *trans* in PVA and PVA:KSCN.

	population					
	g^+	t	g^-	g^{+a}	t^a	g^{-a}
PVA; CC*CC*	0.13	0.75	0.12	0.19	0.65	0.16
PVA:KSCN; CC*CC*	0.14	0.72	0.14	-	-	-

[a]De La Rosa *et al.*(De La Rosa *et al.*, 2002) for isotactic PVA.
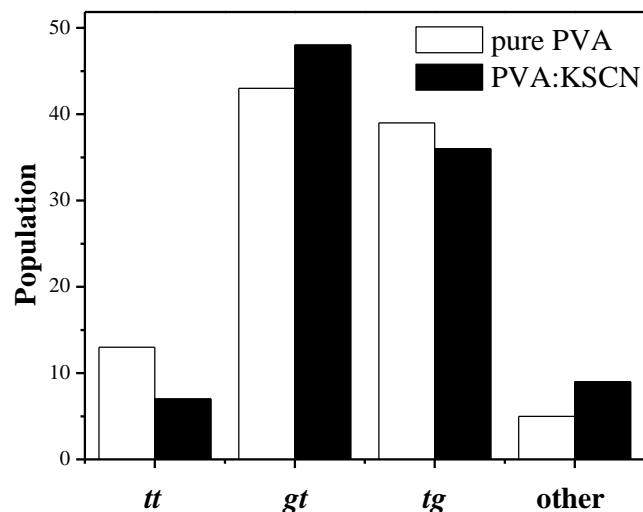
Figure 4.9 Populations of conformational (C-C*-C-C*-C backbone atom sequences) for pure PVA and PVA:KSCN complex.

4.2.3.3 Radial Distribution Function (RDF)

The radial distribution function (RDF) of oxygen atoms and the neighboring methane carbons at 300 K of PVA are shown in Figure 4.10. The oxygen RDF for PVA oligomer shows that the major peak occurs approximately at the same position as in the case of hydrogen bond of isopropyl alcohol (around 2.9 Å). From Figure 4.10(a), we can identify the major peaks at 2.75 and 5.60 Å, similar to result reported by Rossinsky *et al.* (Rossinsky *et al.*, 2009). The first peak (2.8 Å) arises both from *intra*molecular and *inter*molecular hydrogen bonds between hydroxyl groups. The *intra*molecular part is due to oxygen atoms from neighboring repeat units. The prominent peak at 5.5 Å is created by *inter*molecular and *intra*molecular atoms far apart. Adding KSCN salt in PVA shows decreasing peak at 2.75 Å due to K^+ coordinated with hydroxyl groups.

The RDF of the carbon atoms (Figure 4.10(b)) carrying hydroxyl groups are similar to the distribution of hydroxyl oxygens. It is possible to correlate each peak in

the C(CO)-C(CO) RDF to a characteristic peak in the O-O RDF. We also can identify a set of small sharp peaks at 4.65, 5.13, 6.89 and 7.71 Å. All of these peaks are the fingerprints of the monomers in the long-chain systems due to these peaks completely absent in isopropyl alcohol and partially absent for 2,4-pentanediol (Rossinsky *et al.*, 2009). In analogy to the oxygen RDF, these peaks are due to methine carbon-methine carbon located at nearly 4.65, 5.13, 6.89 and 7.71 Å which result mainly from the contribution of the *intra*molecular pair for PVA (Moon *et al.*, 2007). They are somewhat sharper than the corresponding peaks in oxygen RDFs. This can be explained by the fact that carbon atoms are linked through fewer bonds than oxygen atoms. Upon mixing KSCN to PVA, the peak at 5.13 Å become sharper than pure PVA due to the conformation change upon coordinating with K^+ ion.
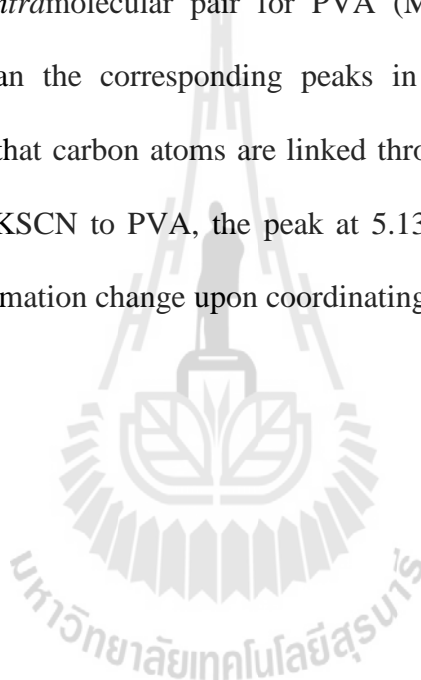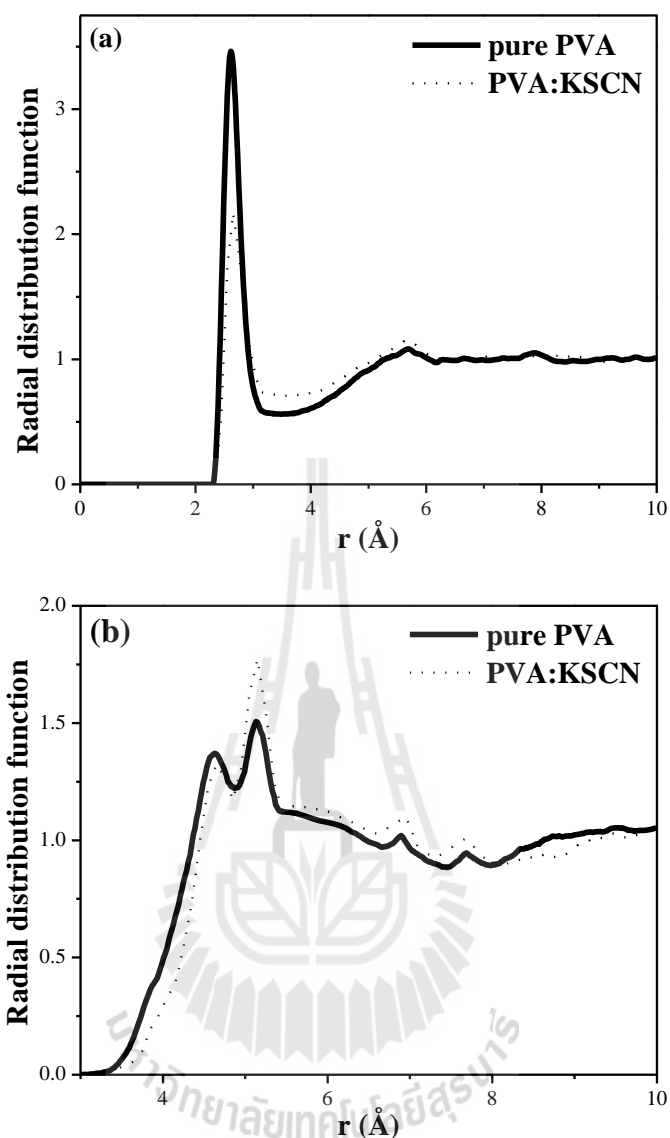
Figure 4.10 RDF between (a) oxygen atoms and (b) carbon atoms (connected to oxygen) of PVA at 300 K.

For PVA:KSCN system, RDFs between K^+ and all other species in the complexes were calculated and plotted separately in Figure 4.11. The R_0 and N were summarized in Table 4.5. Integrating over the first coordination shells of K^+-O, K^+-H and K^+-C RDFs give 4.8 oxygens, 19.4 hydrogens and 11.70 carbons coordinated with K^+. Accordingly, the distance of K^+-O, K^+-H and K^+-C were 2.57, 3.13 and 3.77

Å, respectively. In addition, there is no competition in the interaction between K^+ with

SCN^- (same as H_2O:KSCN system). Therefore, K^+ surrounded by PVA oxygen atoms

is mainly electrostatic. The example snapshot of K^+ surrounded by PVA is shown in

Figure 4.12. It is seen suggested that PVA chain is wraped around K^+ ion by some

oxygen atoms. As in the case of K^+ in liquid methanol (Faralli *et al.*, 2007) R_0 and N

of K^+-O coordination obtained by *ab initio* Car-Parrinello molecular dynamics

simulations (CPMD) is around 2.70 Å and 5.41, respectively. It is important to note

that R_0 and N obtained by CPMD simulation for methanol system are lower than the

corresponding values in water ($R_0 = 2.81$ Å and $N = 6.75$), essentially due to greater

steric effects of methanol molecules. Conversely, (PEO)$_4$KSCN complex (Lightfoot *et*

al., 1994) gives the oxygen coordination number around K^+ ion around seven. This

probably accounts for the availability of five ether oxygens and two nitrogens of

anion for coordination to K^+ ion. So, for the solvation structure to compute MD-

EXAFS spectra of PVA:KSCN complex, there is no need to include SCN^- anion in

the calculation.

Figure 4.13 display probability for number of oxygen atoms coordinating with

K^+ cation for K^+:O = 1:20 in PVA:KSCN system. The coordination number varies

from four to six for the first coordination shell (within 4.0 Å). The case of five

oxygens coordinating to K^+, however, is the most frequently observed. Intra- and

inter-chain coordination shown in Figure 4.13 represents one and two chains

coordinating with K^+. The overwhelming majority of K^+ cations are complexed by

oxygen atoms from two chains.
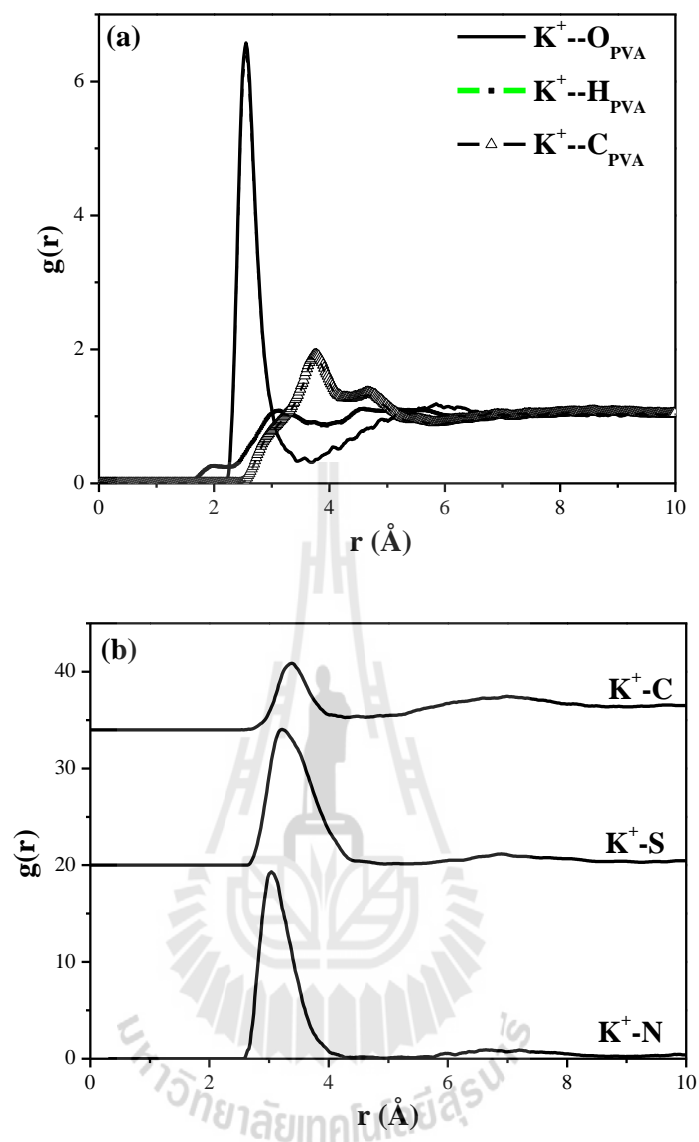
Figure 4.11 Radial distribution functions of PVA:KSCN.

Table 4.5 Parameter characterizing the first peak of RDFs determined from MD of PVA:KSCN at 300 K.

Correlation	PVA:KSCN	
	R_0 (Å)	N
K^+-O_{PVA}	2.57	4.8
K^+-H_{PVA}	3.13	19.4
K^+-C_{PVA}	3.77	11.7
K^+-N_{SCN}	3.15	0.37
K^+-S_{SCN}	3.22	0.37
K^+-C_{SCN}	3.34	0.37
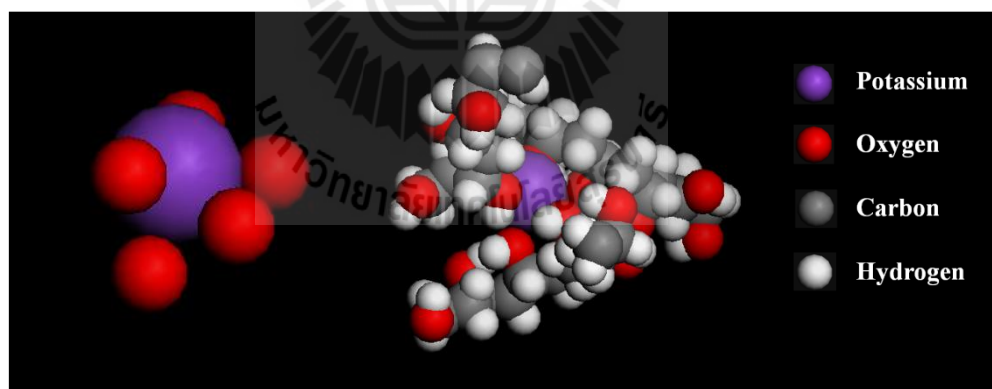
Figure 4.12 Model of potassium ion in PVA.
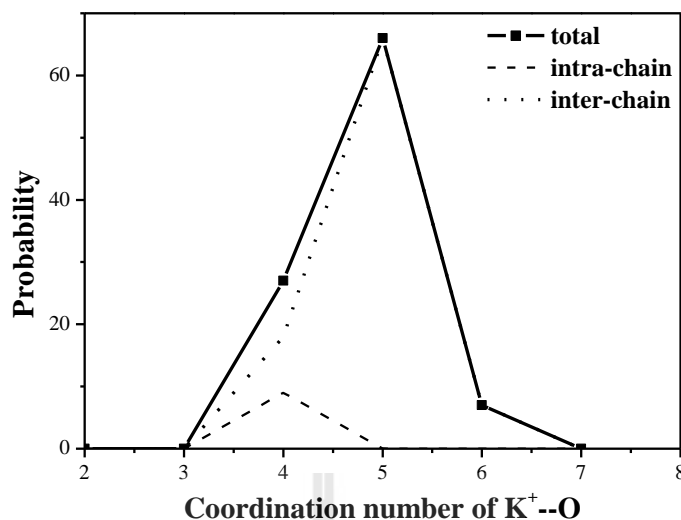
Figure 4.13 Probability of an oxygen atoms coordinating with K^+ cation for K^+:O = 1:20 in PVA:KSCN system.

4.2.3.4 EXAFS spectra and MD-EXAFS

Figure 4.14, shows MD-EXAFS spectra for both k^2-weighted $\chi(k)$ and $\tilde{\chi}(R)$ plot compared to experimental spectra for PVA:KSCN (K^+:O = 1:20) at 300 K. Similar to K^+-H_2O interaction in Figure 4.6, MD simulation faithfully reproduces the major features of the spectrum. This is further demonstrated by $\tilde{\chi}(R)$ plots in Figure 4.14(b) that shows K^+-O scattering from the first-shell O atoms in PVA. The frequency matching of these oscillations means that the distances between K^+ and oxygen of PVA molecules were nearly the same compared between experiment and simulation. The MD-EXAFS peak is narrower indicating that PVA molecules are more ordered in solvating K^+ for the simulated structures. There is little or no evidence of K^+-H and K^+-C scattering from the methyl unit (-CH_2-) which mainly affect the low-k region in either experiment or simulation. This mean that the wagging or rocking motions about the K^+-O-C bonds induce a large amount of positional

disorder for the K^+-C distance, thereby dampening this contribution to the EXAFS signal. The higher degree of disorder is similar to that observed for Sr^{2+} in methanol (Roccatano *et al.*, 1998), where the Sr^{2+}-H and Sr^{2+}-C scattering shows only very weak contribution to the total signal. It is remarkable that although the -CH$_3$ group on the methanol impedes interaction with the second shell molecules, it seems to have little effect on the first solvation shell structure. As mentioned in H$_2$O:KSCN system, MD-EXAFS calculation exclude the anion effect due to a small amplitude of anion coordination number. This work demonstrates that the combination of MD-EXAFS and the corresponding experimental measurement provides a powerful tool in the analysis of the solvation structure of PVA with salt.
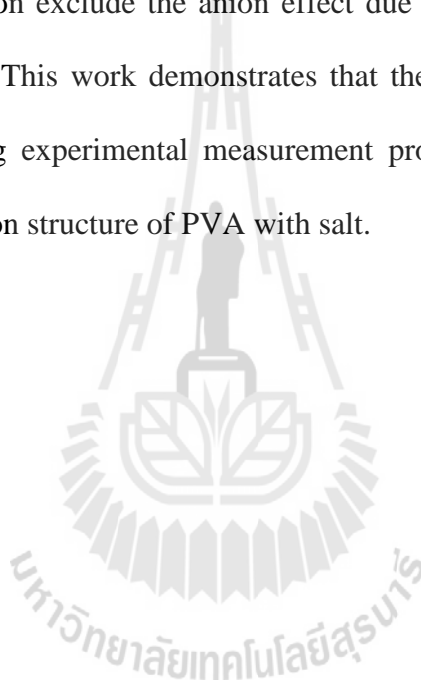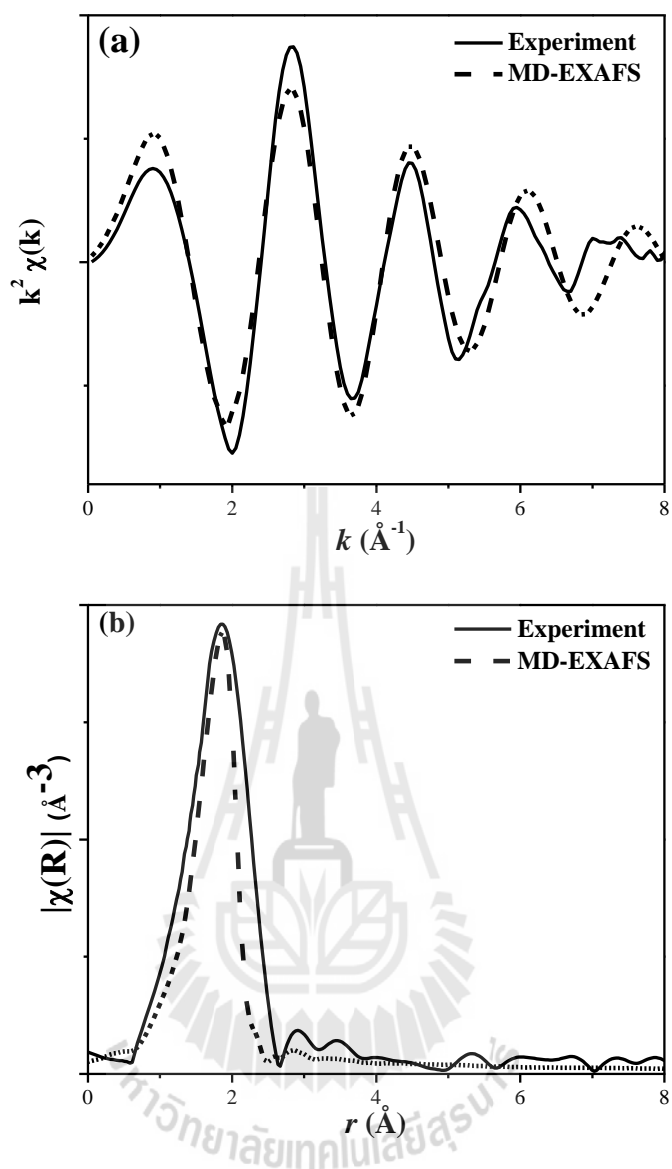
Figure 4.14 Comparison (a) $k^2\chi(k)$ and (b) $|\tilde{\chi}(R)|$ EXAFS spectral from experiment

and MD-EXAFS for PVA:K$^+$ system.

4.3 Tetraglyme:KSCN (TET:KSCN) Electrolyte

4.3.1 EXAFS Experimental Details

Potassium K-edge (3608.4 eV) EXAFS spectra were collected at X-ray Absorption Spectroscopy beamline 8 (BL8), Synchrotron Light Research Institute (Public Organization), Thailand. The EXAFS measurements were done for a 1:10, 1:20 and 1:40 (K^+:O) TET:KSCN (tetraglyme or tetraethylene glycol dimethyl ether, defined as $CH_3O(CH_2CH_2O)_4CH_3$).

4.3.2 Fourier Transform Infrared spectroscopy (FTIR)

TET [Mw = 222 g/mol, a 4-mers model compound of PEO] was used as received. Potassium thiocyanate (KSCN, Fluka), was dried in vacuum oven at 353 K for 24 hour. TET and given amounts of KSCN were mixed and stirred vigorously for 24 hour until a homogenous solution was formed. For infrared measurements, the gelatinous polymer solution was cast on KBr windows and then the spectra were collected at room temperature. The composition of SPEs is represented as K^+: ether oxygen ratio (K^+:O) = 1:n, where n refers to the molar ratio of ethylene oxide repeating unit and salt. Infrared absorption spectra were recorded on FT-IR spectrometer Perkin-Elmer model: spectrum GX in the range 4000-400 cm^{-1} with a resolution of 2 cm^{-1}.

4.3.3 Computational Details

MD simulation was employed to study the structure of amorphous TET:KSCN. An advantage to use tetraglyme (TET) to represent PEO is because tetraglyme and tetraglyme:salt complexes are easily equilibrated, experimentally and

computationally, than longer chain analog. It is also benefit to use KSCN salt as one can capture the monodentate, bidentate, or tridentate different atom to coordinate with K^+ by SCN^-. Coordination of cation to tetraglyme or PEO also causes the conformational change and their relation to the extent of ionic aggregation.

MD of TET, TET:K^+ and TET:KSCN were performed using the Amorphous Cell module with COMPASS forcefield in Materials Studio 4.2 software package provided by National Nanotechnology Center, Thailand. The simulated systems containing 50 TET chains, 50 TET plus 12 K^+ and 50 TET chains plus 12 K^+ and 12 SCN^- ions (M:O = 1:20) were generated. After energy minimization, MD simulations were initially performed in NPT ensemble at 400 K for 1 ns to obtain a new equilibrium density (1.009 g/cm^3). Further equilibration of approximately 1 ns was run in NVT ensemble. For data analysis, atomic trajectories were collected for another 1 ns. The properties investigated by MD techniques are: structure (radial distribution function between K^+ and all other species $i.e.$ O, C, H and SCN^-), conformation (dihedral angle distribution along C-C, O-C and C-O bonds) and dimension (radius of gyration, a measure of the size of the spatial domain of polymer chain).

Table 4.6 Charge parameters used in the simulation.

atom	q (e)	atom	q (e)
K	+1.000	C_{TET}	+0.054
S_{SCN}	-0.560	O_{TET}	-0.320
C_{SCN}	0.140	H_{TET}	+0.053
N_{SCN}	-0.580		

4.3.4 Results and Discussion

4.3.4.1 Chain Conformation and Dimension

Experimental studies of PEO:salt complexes such as vibrational spectroscopy and XRD (Papke *et al.*, 1981; Dupon *et al.*, 1982) show that the conformation of PEO chains is altered upon complexation of metal salts. KSCN complexation with TET chains is therefore expected to alter the conformation of TET chains. This characteristic can be considered by the change in dihedral angles population and dimensions of TET chains such as the root-mean-square radius of gyration $\langle S^2 \rangle^{1/2}$.

To examine the conformation of TET, the time-averaged population density distributions of backbone dihedral angles (θ) around *C-O* bonds (*C-C-O-C* atom sequence) and *C-C* bonds (an *O-C-C-O* atom sequence) were calculated from MD simulation trajectories. This analysis provides more detailed information about TET chains and supplements the subsequent chain dimension calculations. Comparison of dihedral angles for uncomplexed TET and TET:KSCN is shown in Figure 4.15. The dihedral angles around C-C bonds distribution of TET gives three peaks, with two bigger peaks at two ends centered around 70° and 290° and between them a small peak centered around 180°. The convention is to define the conformation with heavy atoms eclipsed as $\theta = 0°$ and label *gauche*$^+$ (g^+) conformations if the torsional angle has value in the range $0° < \theta < 120°$, *gauche*$^-$ (g^-) conformations if $240° < \theta < 360°$, and *trans* (*t*) conformations if $120° < \theta < 240°$. By our definition, the C-C bonds of TET prefer the *gauche* over the *trans* states. This is referred to as the oxygen *gauche* effect (Flory, 1988; Abe and Mark, 1976). The *gauche* effect is also found in PEO and low molecular weight oligomer crystals, melts, and in solution. It is believed that a

pendent oxygen atom acts to lower the energy of the *gauche* conformation despite the Coulombic repulsion between oxygen atoms in polyethers and therefore makes the *gauche* state the preferred conformation over the *trans* state. For the dihedral angles around C-O bonds, the distributions indicate that the *trans* conformation is predominant. The corresponding fractions were calculated and compared in Table 4.7. The fractions of *trans* conformation around the C-C bond of TET (0.18) are in good agreement with other studies: i.e., $f_t^{CC} = 0.21$ from electron diffraction (Astrup, 1979), 0.23 from NMR (Inomata and Abe, 1992), 0.26 from MD (Hyun *et al.*, 2001) and 0.23 from RIS model (Jaffe *et al.*, 1993). For the adjoining C-O bond ($f_t^{CO} = 0.73$), the agreement is moderate: $f_t^{CO} = 0.64$ (ED), 0.76 (NMR), 0.80 (MD) and 0.77 (RIS model).

For dihedral angles of KSCN:TET along *C-C* bonds, g^+ and g^- conformation are centered about 64° and 296°, instead of 70° and 290° in pure TET (Figure 4.15). This means that two adjacent oxygen atoms of TET can stay in the relatively low-energy *gauche* conformation which allows coordinating K^+ cation. These results are in good agreement with Dhumal *et al*. (Dhumal and Gejji, 2006) work, which focus on how K^+ ions coordinated with TET based on the hybrid density functional theory (B3LYP). The optimized structure 1:1 K^+-TET ion pair exhibit oxygen atom to bind strongly with K^+ ion and the conformation around C-C bond prefers to *gauche* state (67.9° and 292.1°). In MD simulation of TET:NaCF$_3$SO$_3$ (Dong *et al.*, 2002), two distribution peaks of g^+ and g^- are centered around 60° and 300°. The two distribution peaks of TET:NaCF$_3$SO$_3$ complexes show small differences from TET:KSCN complexes. The population of both g^+ and g^- conformations slightly increases (~7.7%)

relative to those of pure TET while t state almost vanishes (~11.1%). The distribution along C-O bonds shows less population of t conformer (~8.0%) and gives higher g^+ and g^- conformations (~22.2%) compared to pure TET. This is resulted from the interaction of K^+ with ether oxygens. An increase in *gauche* population causes TET become more compacted shape as seen in Figure 4.17 where the root-mean-square radius of gyration decreases upon K^+-O coordination. The population of *trans* and *gauche* conformation in KSCN:TET (Table 4.7) are in good agreement with MD simulation reported by Hyun *et al.* (Hyun *et al.*, 2001). The major difference may be from the difference salt used in the previous work (TET:LiCF$_3$SO$_3$ complex).

Conformational triads are three consecutive dihedral angles along C-O-C-C-O-C sequence in tetraglyme chain. Three dihedral angles are around O-C, C-C, C-O bonds and their dihedral angles favor t, g^+ (or g^-), and t, respectively. Therefore, the most probable triads for pure tetraglyme should be tg^+t and tg^-t (in this case, g will be used to represent either g^+ or g^- and g' to indicate a change in sign of the gauche conformation. For example, tgg' implies either tg^+g^- or tg^-g^+). Populations of tetraglyme triads in pure tetraglyme and TET:KSCN are also shown in Figure 4.16.

In both pure tetraglyme and TET:KSCN, the tgt conformation is predominant. The total population of tgt for pure tetraglyme is 49.0% and for TET:KSCN is 57.0%, respectively at 300 K. At this temperature, the population of tgt is higher in TET:KSCN compared to pure tetraglyme. The preference for tgt conformation in TET:KSCN indicates that the K^+-O complexation favors this local chain conformation. It can be easily understood that the gauche angle around the C-C bond enables two oxygens to coordinate with K^+, and the t state implies a further distance

between the big end groups and thus lowers the repulsions. For TET:KSCN, the *tgg* and *tgg*′ conformations have the second (16.0%) and third largest (8.0%) populations.

Compared to pure TET, TET chains that are involved in complexation with K^+ have more *tgg* and fewer *tgg*′ conformations. Dong *et al.* (Dong *et al.*, 2002) reported the TET:NaCF$_3$SO$_3$ complex with Na^+:O = 1:10. The structure shows that TET chain adopts a zigzag conformation in which the triads (C-O-C-C-O-C sequence) are *tgt* and *tgg* conformational sequences, which is consistent with our computational results. Another difference in triads population between pure TET and TET:KSCN occurs in the *ttt* conformation. The K^+-O complexation decreases its population from 17.0% in pure tetraglyme to 8.0%. *ttt* conformation is the most extended chain structure and decrease in *ttt* population implies a shorter end-to-end distance for tetraglyme chains. This is in agreement with the reduction of chain dimension.

As mentioned before, the root-mean-square radius of gyration, $\left\langle S^2 \right\rangle^{1/2}$ are used to investigate the dimensional changes of TET chains which are affected by K^+-ether oxygen complexation. Figure 4.17 shows the distribution of the root-mean-square radius of gyration, $\left\langle S^2 \right\rangle^{1/2}$ for pure TET (*solid line*) and KSCN:TET complexes (*dotted line*). $\left\langle S^2 \right\rangle^{1/2}$ distribution gives two main peaks at 3.35 Å and 4.25 Å. The first smaller peak is represented the more compacted chains and the second larger peak is due to a more stretched chain as shown in Figure 4.18(a) and (b). The higher second peak means that stretched chain is more probable than the compacted one. Upon adding KSCN into TET, the height of first peak obviously increases whereas the second peak decreases. This suggests that K^+-O interaction changes the conformation and dimension of TET. Strong Coulombic attraction between K^+ and ether oxygen tends

to pull segments together and the overall size of molecules in TET:KSCN becomes

smaller. From simulation, the most stable form of KSCN is that K^+ bridges between N

and S Figure 4.18(c) and (d). This result agrees well with *ab initio* calculation of

NaSCN having larger stability of Na^+ in bridging position between N and S compared

to N connected to Na^+ (Oláh *et al.*, 2004).

Figure 4.15 Average population density distributions of TET backbone dihedral

angles around *C-O* and *C-C* bonds.

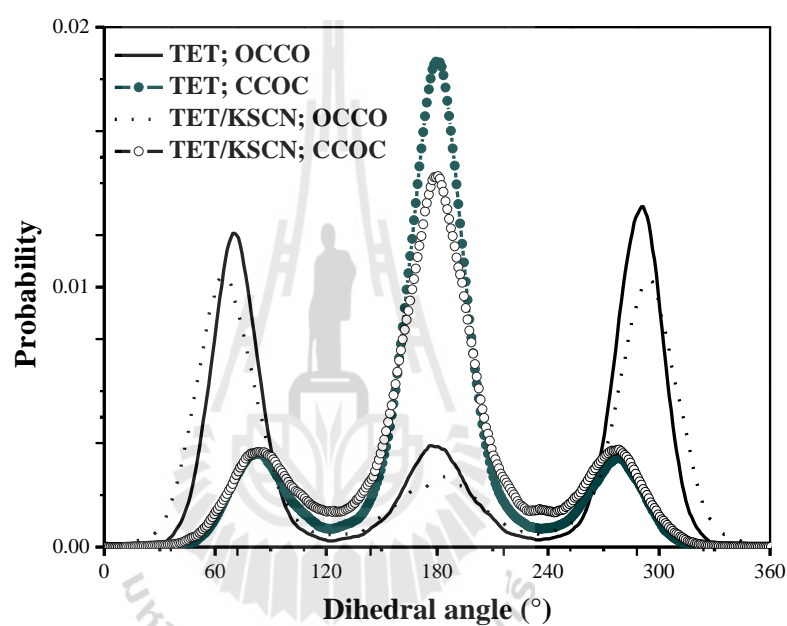
Figure 4.15 Average population density distributions of TET backbone dihedral

angles around *C-O* and *C-C* bonds.

Table 4.7 The population of *gauche*$^{\pm}$ and *trans* in TET and TET:KSCN.

	population								
	g^+	g^{+a}	g^{+b}	t	t^a	t^b	g^-	g^{-a}	g^{-b}
TET; *OCCO*	0.39	0.38	0.39	0.18	0.26	0.23	0.43	0.38	0.38
TET; *CCOC*	0.14	0.10	0.12	0.73	0.80	0.77	0.13	0.10	0.11
TET:KSCN; *OCCO*	0.42	0.44	-	0.16	0.12	-	0.42	0.44	-
TET:KSCN; *CCOC*	0.17	0.12	-	0.67	0.76	-	0.16	0.12	-

[a]Hyun *et al.* (Hyun *et al.*, 2001)

[b]Inomata *et al.* (Inomata and Abe, 1992)
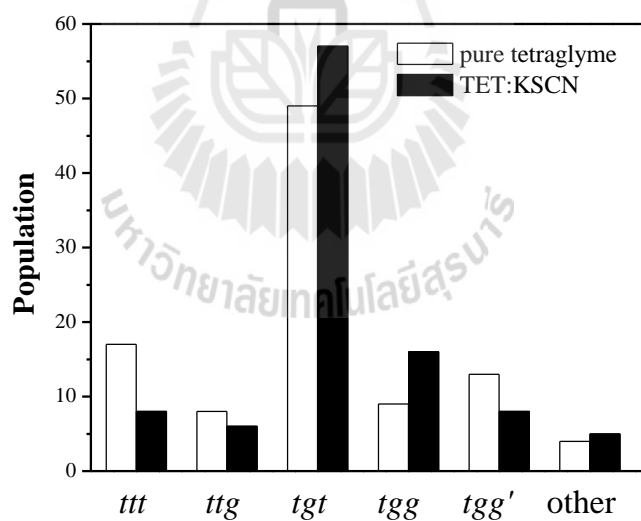
Figure 4.16 Populations of conformational triads (*C-O-C-C-O-C* backbone atom sequences) for pure tetraglyme and TET:KSCN complex.
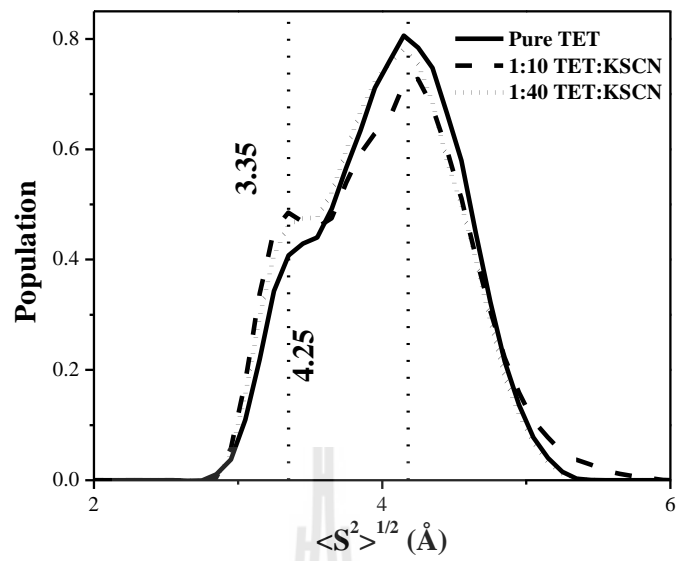
Figure 4.17 $\left\langle S^2 \right\rangle^{1/2}$ distribution for TET:KSCN system with K^+:O = 1:10 *(dashed line)*

and 1:40 *(dotted line)* compared with pure TET system *(solid line)*.

(a)

(b)

(c)

(d)
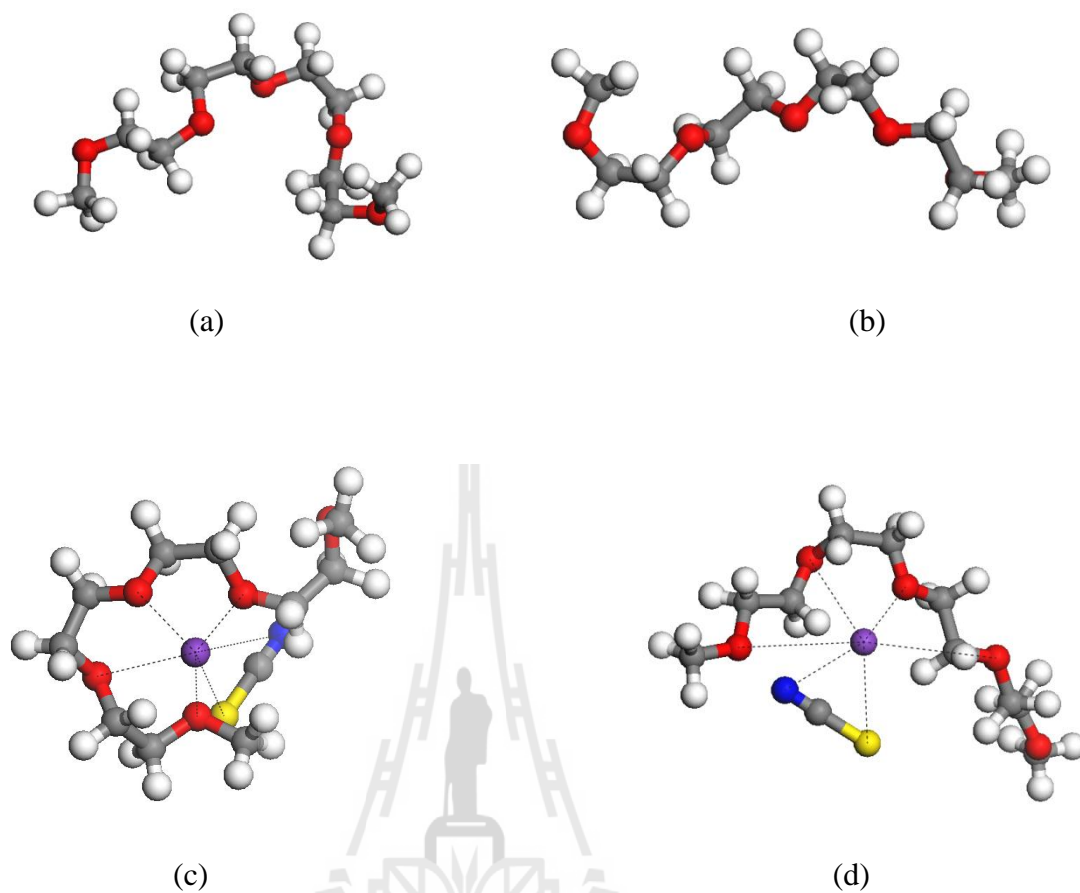
Figure 4.18 Snapshots from MD simulations of (a) compacted TET ($\langle S^2 \rangle^{1/2} = 3.35$ Å),

(b) stretched TET ($\langle S^2 \rangle^{1/2} = 4.25$ Å), (c) compacted 1:20 TET:KSCN and (d) stretched

1:20 TET:KSCN. (colors: hydrogen atoms: white, oxygen atoms: red, carbon atoms:

gray, potassium atoms: purple, sulfur atoms: yellow and nitrogen atoms: blue).

4.3.4.2 Radial Distribution Functions (RDFs)

In TET:K^+ complex, RDFs between K^+ and all TET atoms (O, C, H) were calculated and plotted together in Figure 4.19. The simulated peak positions (R_O) and N calculated from the first peaks of all RDFs are summarized. Each K^+ cation is coordinated by ~8.0 oxygens (K^+–O distance $\leq$ 4.55 Å), ~35.8 carbons (K^+–C $\leq$ 7.15 Å), and ~40.6 hydrogens (K^+–H $\leq$ 5.15 Å). So, in the first solvation shell, K^+ cation is coordinated with ether oxygen from TET. This is consistent to MD techniques with polarizable potential models. Dang *et al*. (2006) presented a detailed study of the solvation structure of K^+ in water. The calculations show that an average of 5.7 water oxygens coordinate K^+ while in our work an average of 8.0 TET oxygens coordinate each K^+. We suggest that the smaller coordination number for H_2O:K^+ system is due to oxygens (or water molecules) in H_2O:K^+ system can diffuse easier than ether oxygens in TET chains. Compared to TET:$NaCF_3SO_3$ complex (Dong *et al.*, 2002), the first solvation structure of Na^+ contain oxygen with the total coordination number of seven, consisting five oxygens from trifate ions and two oxygens from polyether chain. So, for the simulated solvation structural model to compute MD-EXAFS spectra, anion from salt must be included in the calculation.

For TET:KSCN system, RDFs between K^+ and all other species in the complexes (O, C_{SCN}, S and N) were calculated and plotted separately in Figure 4.20(a)-(d). R_0 and N from RDFs were summarized in Table 4.8. Integrating over the first coordination shells of K^+-O, K^+-N, K^+-C_{SCN} and K^+-S RDFs give 2.0 oxygens, 2.4 nitrogens, 2.3 carbons and 2.3 sulfurs coordinated with K^+. There is a competition in the interaction between K^+ with ether oxygens and SCN^-. Accordingly, the distance of K^+-O, K^+-N, K^+-C_{SCN} and K^+-S were 2.67, 2.77, 2.86 and 2.95 Å, respectively. In

addition, the peak position of K^+-anion RDFs suggest that ion pairing may occur at both ion sides, as expected for an ambidentate ligand. The simulated peak position approach the distance of K^+-N pair which are shorter than those of K^+-S, due to smaller ionic radius. Similar results were reported by Dhumal and Gejji (2006b) for 1:1:1 diglyme:K^+:SCN^- complex, K^+ ion exhibits tetradentate coordination (3 ether oxygens and one nitrogen) and the calculated K^+-O distance are varied in the range of 2.76 - 2.85 Å. Other distances (K^+-N, K^+-C_{SCN} and K^+-S) are 2.97, 2.87 and 3.29 Å, respectively. In Figure 4.20, all RDFs peak positions for more diluted system (K^+:O = 1:20 and 1:40) remain the same while N are different as listed in Table 4.8. The similarity in RDF peak positions indicates a fundamental similarity in K^+ complexation. Integrating the first peaks for K^+:O = 1:20 system gives an average 3.0 oxygens, 1.8 nitrogens, 1.8 carbons and 1.8 sulfurs coordinated to K^+. This suggests that ether oxygen is more competitive than SCN^- anion in coordinating with K^+ for diluted system as shown by fewer numbers of solvated anions. It can be said that increase in tight coordination for cation-polymer should lead to low ionic conductivity. Thus, the 1:40 TET:KSCN complexes which gives high coordination numbers should have lower ionic conductivity than 1:10 TET:KSCN complexes. This result is supported by Preechatiwong and Schultz (1996) work in that the highest ionic conductivity of PEO:KSCN is at K^+:O = 1:8 and exhibits an almost completely amorphous state. In addition, the interaction between ether oxygens and K^+ causes a change in TET conformation can be observed in the dihedral distribution function and root-mean-square radius of gyration.

Figure 4.21 display the probability for number of the ether oxygen atom coordinating K^+ cation for (a) 1:10 (b) 1:20 and (c) 1:40 TET:KSCN systems. The

coordination number varies from one to three for 1:10 TET:KSCN, two to four for 1:20 TET:KSCN and three to five for 1:40 TET:KSCN in the first coordination shell (within 4.0 Å). However, the most frequently observed is two (1:10 TET:KSCN), three (1:20 TET:KSCN) and four (1:40 TET:KSCN) ether oxygens coordinating to K^+. Similar results were reported by Borodin and Smith (1998), they report a wide distribution of complexation environments of PEO_{12}:LiI at 450 K, with a significant probability of finding anywhere from two to seven ether oxygen atoms in the first coordination shell of Li^+ cation, with three and six ether oxygen being the most probable. As mention in PVA system, intra- and inter-chain coordination used to represent one and two chains that coordinate with K^+. In 1:10 TET:KSCN system, K^+ cation is complexed by two ether oxygen atoms from a single TET chain. The majority of K^+ cations are complexed by three ether oxygen atoms from a single chain (1:20 TET:KSCN system). This indicate that the conformation around the C-C bond preferred to *gauche* state which promote oxygen binding to K^+. For 1:40 TET:KSCN system, the majority of K^+ cations are complexed by four ether oxygen atoms from two different chains.

Table 4.8 Parameter characterizing the first peak of RDFs determined from MD at 300 K.

Atom Pair	1:10 TET:KSCN		1:20 TET:KSCN		1:40 TET:KSCN	
	R_0	N	R_0	N	R_0	N
K^+-O	2.67	2.0	2.65	3.0	2.67	4.3
K^+-N	2.77	2.4	2.77	1.8	2.79	1.5
K^+-C_{SCN}	2.86	2.3	2.86	1.8	2.88	1.5
K^+-S	2.95	2.3	2.97	1.8	2.95	1.5

R_0 unit = Å
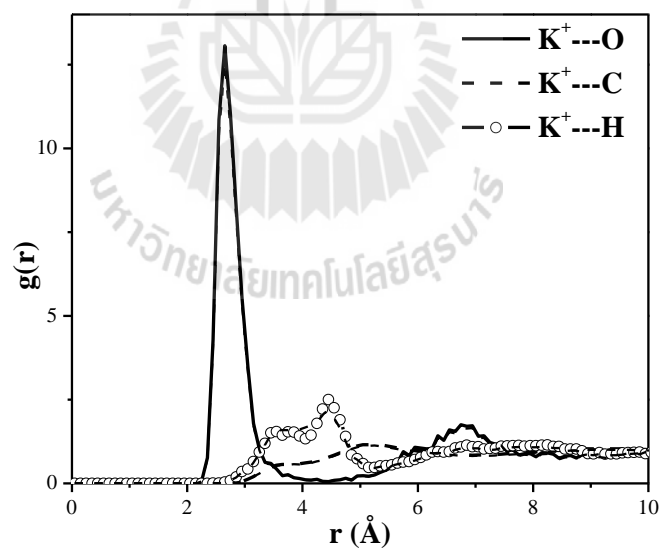
Figure 4.19 Radial Distribution Function (RDFs) for K^+ and all TET atoms.
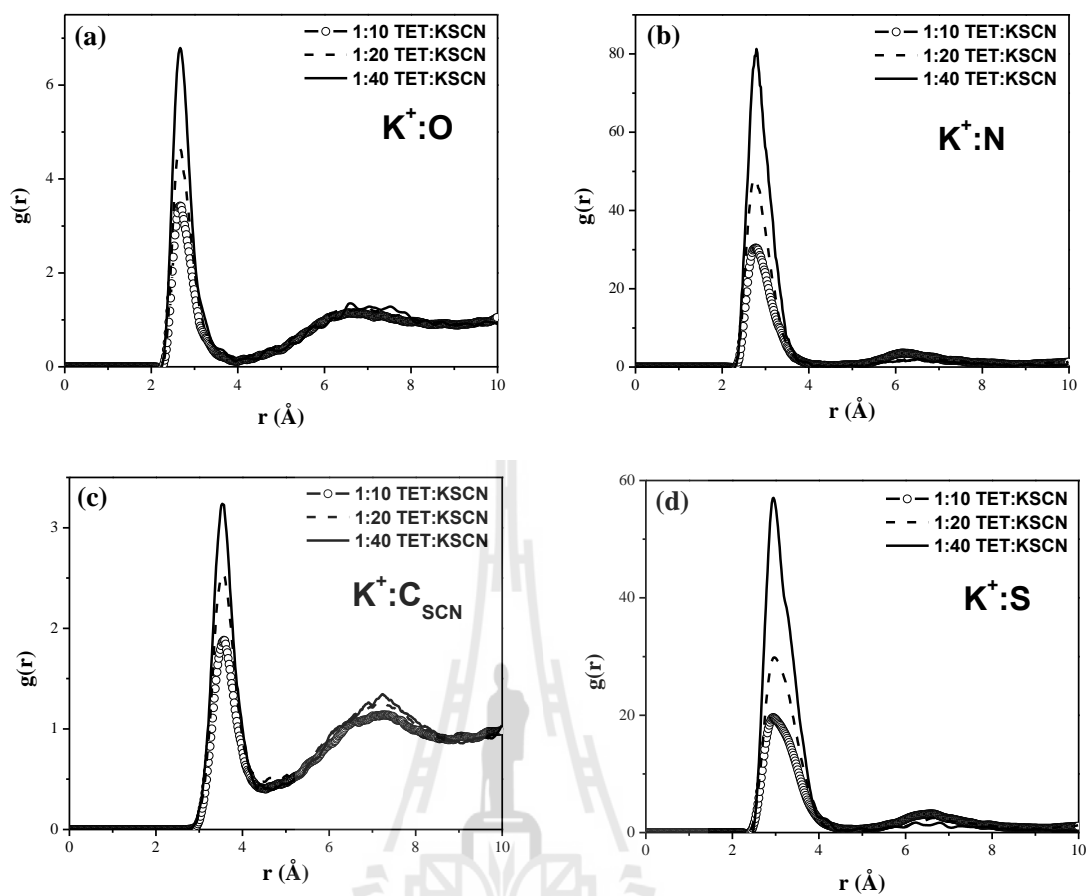
**Figure 4.20** Radial Distribution Function (RDFs) for (a) K^+-O, (b) K^+-N, (c) K^+-C_{SCN} and (d) K^+-S at different K^+:O concentration.
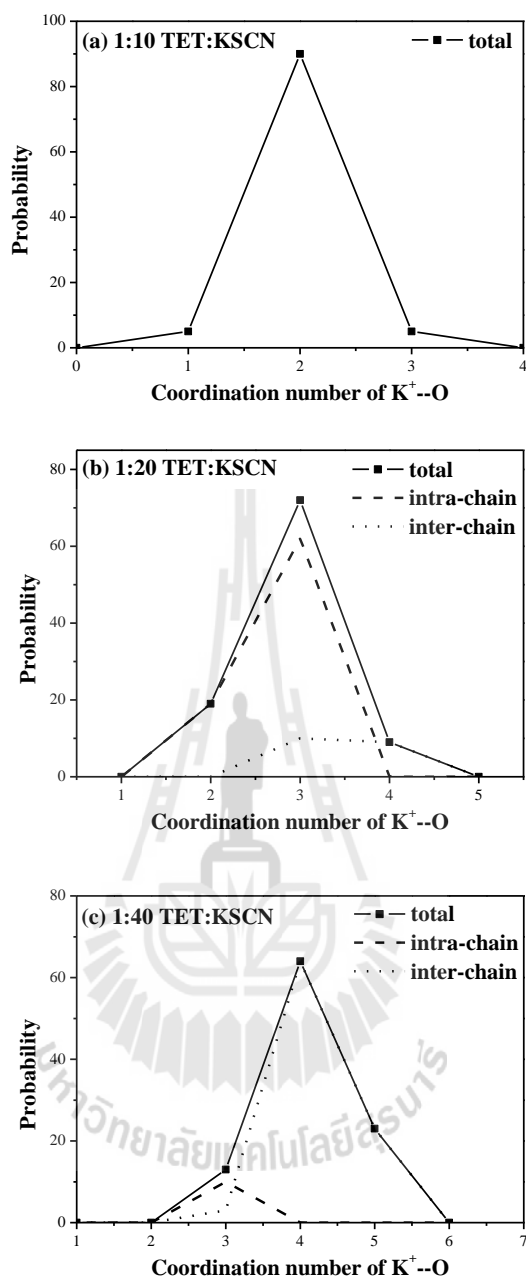
Figure 4.21 Probability of ether oxygen atom coordinating a K^+ cation for (a) 1:10 (b) 1:20 and (c) 1:40 TET:KSCN systems.

4.3.4.3 EXAFS Experiment and MD-EXAFS

Selected 100 independent configurations of TET:K^+ and TET:KSCN from MD trajectories were taken into account for MD-EXAFS analysis. For each configuration, a cluster of the TET and thiocyanate (SCN^-) anion within 5 Å to the photoelectron source (K^+) were extracted to form an input for electron multiple scattering analysis in FEFF.

In Figures 4.22(a) and 4.23(a), the k^2-weighted $\chi(k)$ and $\tilde{\chi}(R)$ plot derived from experimental data were compared to simulated MD-EXAFS spectra for K^+:O = 1:50 system. The MD-EXAFS spectrum calculation not containing thiocyanate anion is far from satisfactory *i.e.* the amplitude of $\chi(k)$ oscillation is too low. Inclusion of SCN^- anion atoms proved necessary to get a realistic backscattering potential. This is consistent to X-ray structure of PEO_4KSCN that shows K^+ ion coordinating with ether oxygen and nitrogen from SCN^- anion.

For TET:KSCN system, Figures 4.22(b)-(d) and 4.23(b)-(d) compare experimental data to MD-EXAFS simulated spectra for K^+:O = 1:10, 1:20 and 1:40 system both in k^2-weighted $\chi(k)$ and $\tilde{\chi}(R)$ plot. All curves are in good agreement for frequency and amplitude of the oscillations over the full k rang from 1 to 8 Å^{-1}. The frequency matching of the oscillations means that the distances of K^+-O, K^+-N, K^+-C_{SCN} and K^+-S were nearly the same for experiment and simulation. The corresponding $\tilde{\chi}(R)$ plots derived from the experimental measurements were shown in Figure 4.23, together with the computed generated ensemble (MD-EXAFS) and fitting. $\tilde{\chi}(R)$ was generated by Fourier transform of $k^2\chi(k)$ data to represent partial pair distribution functions convoluted with the photoelectron scattering functions.

Again, this is a remarkably good agreement in the radial structures of experimental and simulated data. These results suggest that K^+ coordinated to both ether oxygen and SCN^- as described in RDFs results.
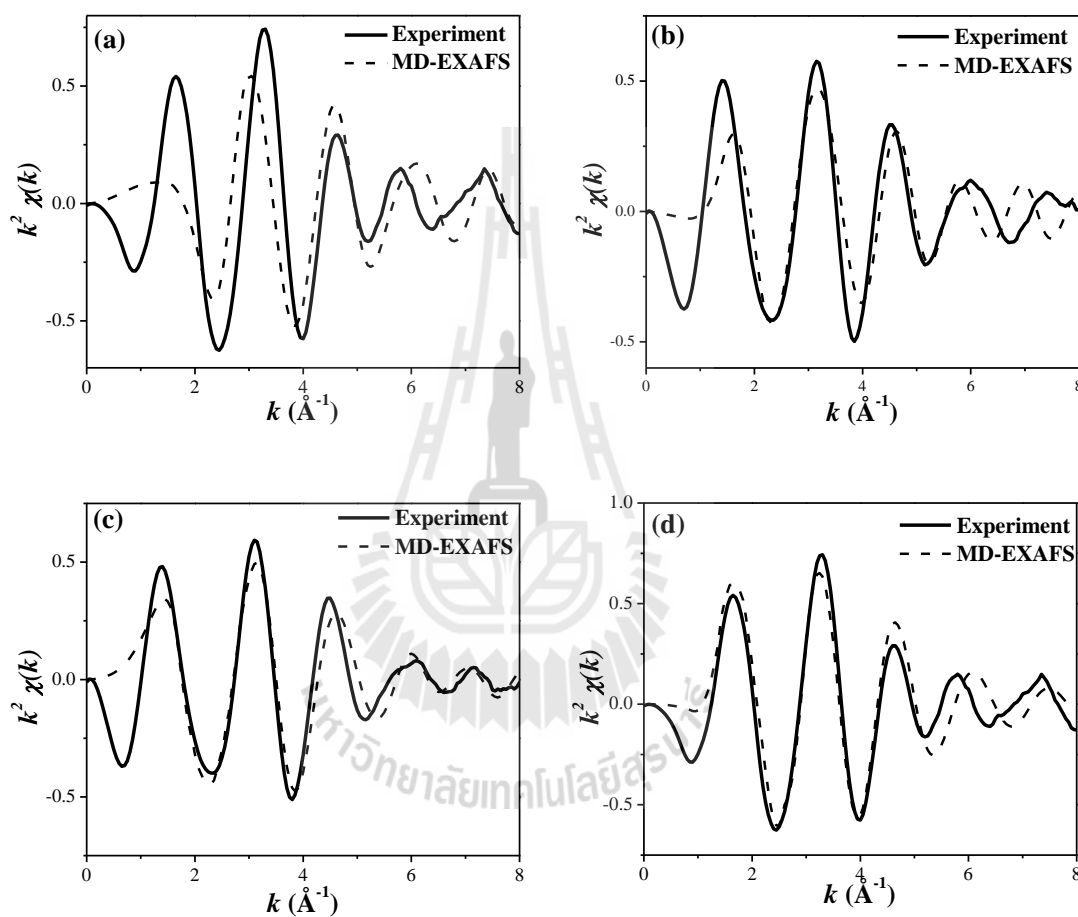
Figure 4.22 Comparison of the $k^2\chi(k)$ EXAFS spectral from experiment and MD simulation for (a) 1:20 TET:K^+, (b) 1:10, (c) 1:20 and (d) 1:40 TET:KSCN system.
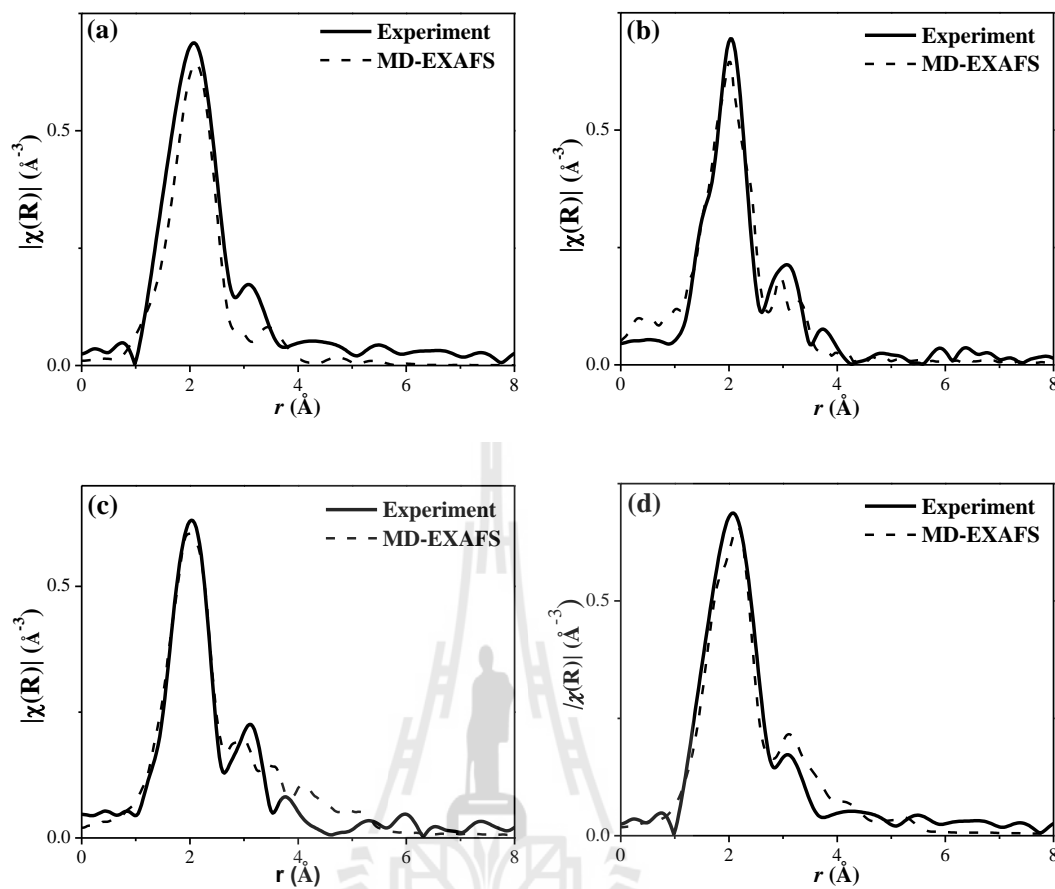
Figure 4.23 The $|\tilde{\chi}(R)|$ plots corresponding to the Fourier transformed $k^2\chi(k)$ from experiment and MD simulation for (a) 1:50 TET:K$^+$, (b) 1:10, (c) 1:20 and (d) 1:40 TET:KSCN system.

### 4.3.4.4 Ionic Association

As mentioned earlier, RDFs results for SCN$^-$ suggest a formation structure between TET with metal ions through N or S atom. The formation of N- or S-bonded complex gives rise to spectral changes in the vibrational frequencies of CN stretching mode in SCN$^-$ (in 2010-2130 cm^{-1} region). The CN stretching modes have high absorption intensity, high sensitivity to its ionization states and little overlap with FT-IR spectrum of PEO. In order to investigate ion association in these electrolytes, the spectral envelope of SCN$^-$ is curve-fitted to a straight base line and one Gaussian function for each band. The predominant peak at 2056 cm^{-1} is assigned to spectroscopically contact ion-pairs (K$^+$SCN$^-$); the peak at 2081 cm^{-1} is attributed to the triple ion aggregates; the peak at 2104 cm^{-1} is an indication for the formation of the higher ion aggregations; the peak at 2044 cm^{-1} is ascribed to the contact ion-pair dimers (K$^+$SCN$^-$)$_2$. The results of curve fitting for TET:KSCN were shown in Figure 4.24, in which the relative intensity of the peaks was expressed as percents. For lower salt concentration (K$^+$:O = 1:40), it can be seen that a relative intensity of the peak of contact ion-pair increase with increasing the salt content, whereas the relative intensities of peaks of the triple ion and higher ion aggregates decrease under the same condition and no peak of contact ion-pair dimers is observed. These phenomena can be explained as results of PEO:NH$_4$SCN electrolytes (Zhang and Wang, 2009). It is well known that PEO at room temperature consists of crystalline and amorphous phases, and inorganic salts can well dissolve in the amorphous part of PEO. When inorganic salts are introduced to PEO, the large SCN$^-$, the contact ion-pairs can play a role of "plasticizer", and transform PEO form crystal to amorphous phase. Therefore, the microenvironment of solvation in the electrolytes is improved due to salt addition,

and leads to a decrease of relative intensity of the bands of triple ion and higher ion aggregates. Moreover, these phenomena lead to more ether oxygen coordinated with K^+ rather than N or S in SCN^-, these results consistent with RDFs results. For higher salt concentration (K^+:O = 1:10), it is observed that the peak of contact ion-pair, triple ion and the higher ion aggregates decrease with increasing salt content. However, a new peak at 2044 cm^{-1} is detected and suggest as the contact ion-pair dimers are formed. These phenomena suggest the trend of potassium solvation by ether oxygen is reduced. It is evident that the relative intensity depends on salt content to N for K^+ with all other species in TET:KSCN.
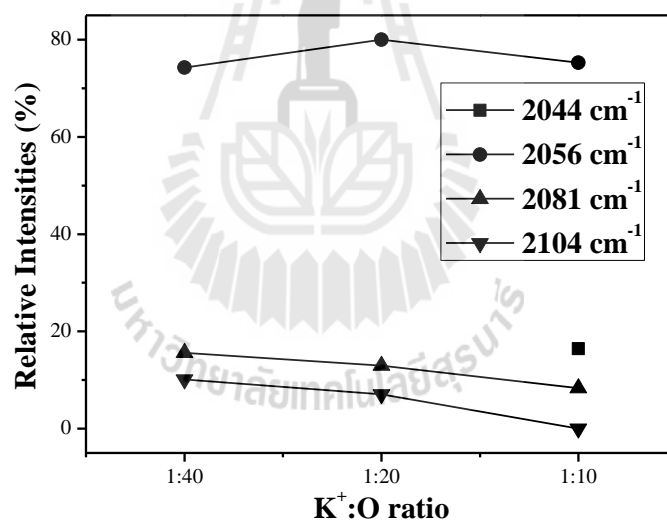
Figure 4.24 The results of curve-fitting to FTIR data for TET:KSCN complexes at different K^+:O ratio.

4.4 Poly(propylene glycol):KSCN (PPG:KSCN) electrolyte

It is generally believed that ion conduction takes place in the amorphous domains of the polymer matrix and is assisted by large-amplitude segmental motion (Berthier *et al.*, 1983; Fauteux *et al.*, 1988). Hence, it is advantageous to reduce the crystalline order and try to create an amorphous system which remains in this state throughout the temperature range of interest. Several methods have been reported in literature for the synthesis of novel polymers that would improve the ionic conductivity of polymer electrolyte (Blonsky *et al.*, 1984; Killis, Le Nest, Gandini and Cheradame, 1984; Xia *et al.*, 1984; Allcock *et al.*, 1986; Blonsky *et al.*, 1986; Greenbaum *et al.*, 1988). They include modification of polymer by (i) formation of crosslinked networks (Killis, Le Nest, Gandini, Cheradame*, et al.*, 1984; Watanabe *et al.*, 1986; Le Nest *et al.*, 1988; Ballard *et al.*, 1990; Killis, Le Nest, Gandini and Cheradame, 1984) (ii) formation of block copolymers (Robitaille and Prud'homme, 1983; Bannister *et al.*, 1984; Watanabe *et al.*, 1985; Spindler and Shriver, 1988) (iii) plasticization (addition of small organic solvent molecules) (Kelly *et al.*, 1985; Sheldon *et al.*, 1989; Chintapalli and Frech, 1996; Chaodamrongsakul, 2003) and use of structurally similar polymers such as poly(propylene glycol); PPG (Bernson and Lindgren, 1993; Schantz and Torell, 1993). PPG appear to be an ideal candidate as a stable and amorphous host polymer which significant ionic motion in polymer electrolytes.

This part studies the solvation structure of PPG:KSCN using a combination of Molecular Dynamic (MD) simulation and Extended X-Ray Absorption Fine Structure (EXAFS) called "MD-EXAFS" method. The solvation structure and ionic

conductivity of PPG:KSCN were undertaken and compared with TET:KSCN to get more understanding at the molecular level.

4.4.1 EXAFS Experimental Details

Potassium K-edge (3608.4 eV) EXAFS spectra were collected at X-ray Absorption Spectroscopy beamline 8 (BL8), Synchrotron Light Research Institute (Public Organization), Thailand. The EXAFS measurements were done on a 1:20 (K^+:O) PPG:KSCN.

4.4.2 Conductivity measurement

Ionic conductivity was obtained using Jenway 4020 conductivity meter. Before measurement the conductivity, the probe has been calibrated. The tip of the probe were inserted into the samples to be tested. While gently swirling the probe, wait for the reading on your computer screen to stabilize. This should take no more than 5 to 10 seconds. Rinse the tip of the Conductivity Probe with distilled water.

4.4.3 Computational Details

MD simulation was carried out on a system consisting of 10 KSCN and 25 atactic PPG [$CH_3O(CH_2CH(CH_3)O)_7CH_3$] chains in a cubic simulation box with linear dimensions roughly of 20 Å. Periodic boundary condition was applied in all three spatial directions. After energy minimization, MD simulations were initially performed in NPT ensemble at 300 K for 1 ns to obtain a new equilibrium density. Further equilibrations of approximately 1 ns were run in NVT ensemble. For data analysis, atomic trajectories were collected for another 1 ns. MD-EXAFS spectra

were averaged over the 100 configurations. For each configuration, a cluster of all atoms that fell within a 5 Å radius of the potassium ion was extracted to form an input for electron multiple scattering analysis.

Table 4.9 Charge parameters used in the simulation.

atom	q (e)	atom	q (e)
K	+1.000	C_{PPG}	+0.120
S_{SCN}	-0.560	O_{PPG}	-0.330
C_{SCN}	0.140	H_{PPG}	+0.117
N_{SCN}	-0.580		

4.4.4 Results and Discussion

4.4.4.1 Chain Conformation

The chain conformation is conveniently described via a set of dihedral angles. There are three different types of dihedrals along the main chain, OC*CO, COC*C, C*COC*, where the notation C* is used for the chiral carbon atom. For the dihedral angles around the C-O bonds the *trans* conformation is dominating with about 60% for the C*COC* and COC*C dihedral. On the other hand, around the C*-C bond, only about 40% of the dihedrals are in the *trans*-conformation and the rest is in the two *gauche*-conformations. The reason for this trend is that the connected methyl groups and hydrogen atoms make the chiral carbon atom more "bulky" compared to the oxygen atoms. It implies that the *gauche* transformations become less favorable

for the C*COC* and COC*C dihedrals. Similar results are found by MD simulation for PPG systems with various chain lengths (Ahlstrom *et al.*, 2000). The backbone dihedral angle distributions are also nearly identical for PPG_{11} and PPG_{45} but deviate slightly from the ones for PPG_1. The probability for *gauche* conformations is quite large. It is equal to about 60%, 40% and 30% for the OC*CO, COC*C and C*COC* dihedrals, respectively.

Conformational distributions for PPG system at 300 K have been calculated. The OC*CO and COC*C distributions are evaluated by mirroring around 180° for each dihedral angle depending on the chirality of the C* carbon. This gives rise to the distributions shown in Figure 4.25. A quantitative analysis of the dihedral distribution is presented in Table 4.10. The probability of *gauche* conformations for PPG:KSCN system slightly increases (~15%) relative to pure PPG. This means that PPG backbone adopt a relatively lower-energy *gauche* conformation which oxygen atoms coordinating K^+.

Conformational triads are three consecutive dihedral angles along a C*-O-C-C*-O-C PPG chain sequence. The three dihedral angles are around O-C, C-C*, C-O bonds and their dihedral angles favor *t, g^+* (or *g^-*), and *t*, respectively. Therefore, the most probable triads for pure PPG should be *tg^+t* and *tg^-t*. Populations of triads in pure PPG and in PPG:KSCN are also shown in Figure 4.26. For pure PPG, the total population of *tgt* is 53.0% and in PPG:KSCN the population of *tgt* is 58.0%. At a given temperature, the population of *tgt* is higher in PPG:KSCN compared to pure PPG. Similarly in TET:KSCN system, *tgt* conformational sequences is dominated, which indicates that the K^+-O complexation favors this local chain conformation. The *gauche* angle around C*-C bond implies that two oxygen atoms coordinate with K^+

and *trans* angle around O-C and C-O bond implies the low repulsion between end groups and K^+.

Table 4.10 The distribution of the various dihedral angles at 300 K.

	population					
	g^+	g^{+a}	t	t^a	g^-	g^{-a}
PPG; OC*CO	0.18	0.21	0.39	0.39	0.43	0.40
PPG; COC*C	0.05	0.02	0.57	0.58	0.38	0.40
PPG; C*COC*	0.20	0.14	0.60	0.72	0.20	0.14
PPG:KSCN; OC*CO	0.20	-	0.32	-	0.48	-
PPG:KSCN; COC*C	0.056	-	0.524	-	0.42	-
PPG:KSCN; C*COC*	0.24	-	0.52	-	0.24	-

[a]Ahlstrom *et al.* (2000)
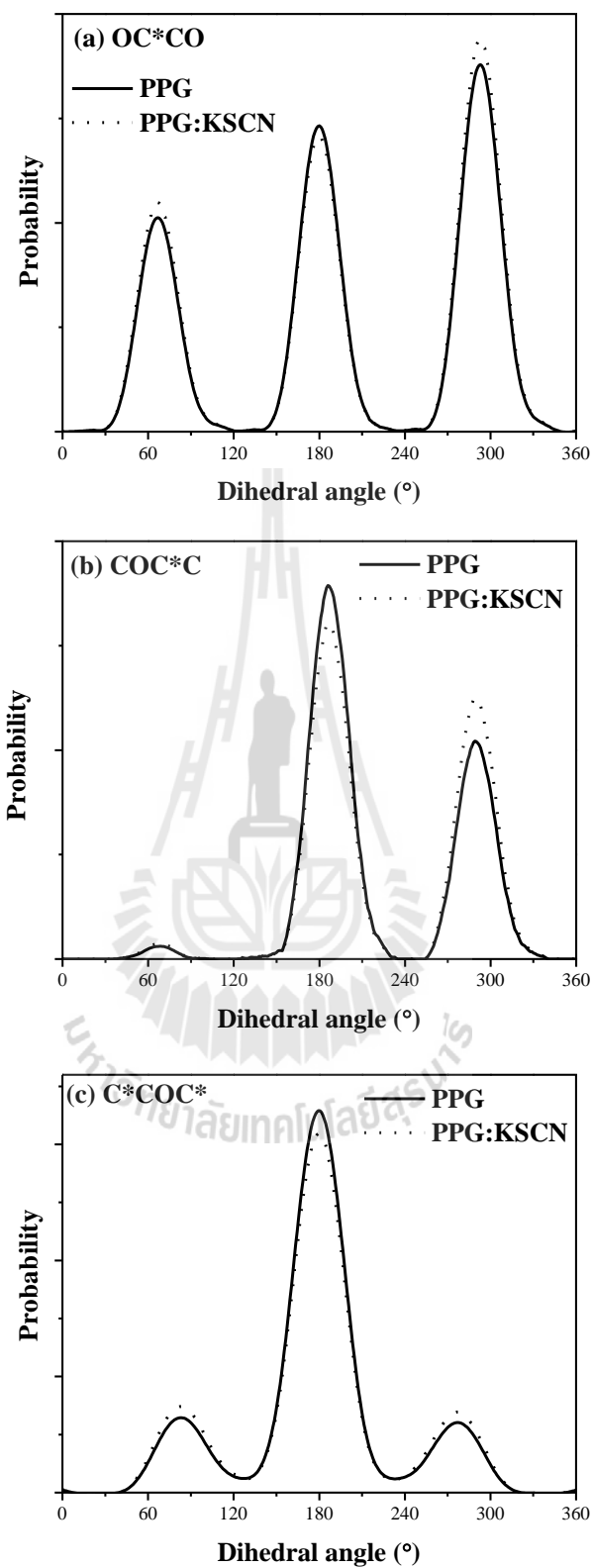
Figure 4.25 Average population density distributions of PPG backbone dihedral angles around (a) OC*CO, (b) COC*C and (c) C*COC* bond.
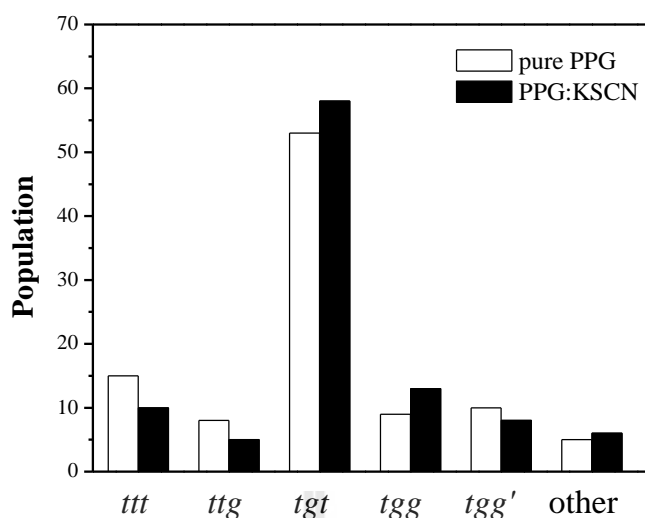
Figure 4.26 Populations of conformational triads (C*-O-C-C*-O-C backbone atom sequences) for pure PPG and PPG:KSCN complex.

4.4.4.2 Radial Distribution Functions (RDFs)

As in the case of TET:KSCN system, to study the solvation structures of PPG:KSCN system, the model for MD simulation must have anion. RDFs between K^+ and all other species in the complexes were calculated and plotted separately in Figure 4.27. R_O and N were summarized in Table 4.11. Integrating over the first coordination shells of K^+-O, K^+-H and K^+-C RDFs give 3.8 oxygens, 15.6 hydrogens and 4.9 carbons coordinated with K^+. Accordingly, the distance of K^+-O, K^+-H and K^+-C were 2.65, 3.29 and 3.55, respectively. So, in first solvation shell, K^+ cation is mainly coordinated with ether oxygen from PPG (same as TET system). This is consistent with previous vibrational studies by Suthanthiraraj *et al*. (2010) that show the vibrational spectroscopic and electrochemical characteristics of PPG:AgCF$_3$SO$_3$. The observed infrared spectral features of the C-O-C stretching mode (~1,110 cm^{-1}) decrease as the cation tend to dissociate and coordinate with ether oxygen. Figure

4.27(c) shows RDF of K^+ and SCN^- species and equally give 0.9 nitrogen, sulfur and carbon atoms coordinated with K^+. There is a competition in the interaction between K^+ with ether oxygens and SCN^-. Accordingly, the distance of K^+-N, K^+-S and K^+-C_{SCN} were 2.60, 2.77 and 2.69 Å, respectively. These results resemble to TET:KSCN system (Figure 4.27(b) and (d)) which suggest that the first solvation shell of K^+ should coordinate with both ether oxygen and SCN^- anion. The simulated peak position approach distance of K^+-N pair is shorter than those of K^+-S, due to smaller ionic radius. *N* of PPG:KSCN system exhibit more oxygen atoms to coordinate with K^+ than in TET:KSCN system. The different solvation structure of PPG:KSCN (Figure 4.28) may affect the ionic conductivity due to tighter coordination which lead to a reduced ionic mobility.

The probability of K^+ complexed with oxygen atoms by one (intra-chain coordination) or two different (inter-chain coordination) PPG chains for K^+:O = 1:20 PPG:KSCN system is shown in Figure 4.29. The coordination numbers vary from three to five for the first coordination shell (within 4 Å). The most frequent probability is four oxygen atoms from two PPG chains coordinated to K^+. Comparison between 1:20 PPG:KSCN and 1:20 TET:KSCN system, it indicates that only one TET chain but two PPG chains needed to coordinate with K^+. These results can be explained by the bulky chiral carbon atoms that connected to methyl group in PPG and the C*-C bonds prefer to form *gauche*-conformation that make two PPG chains to complex with K^+.
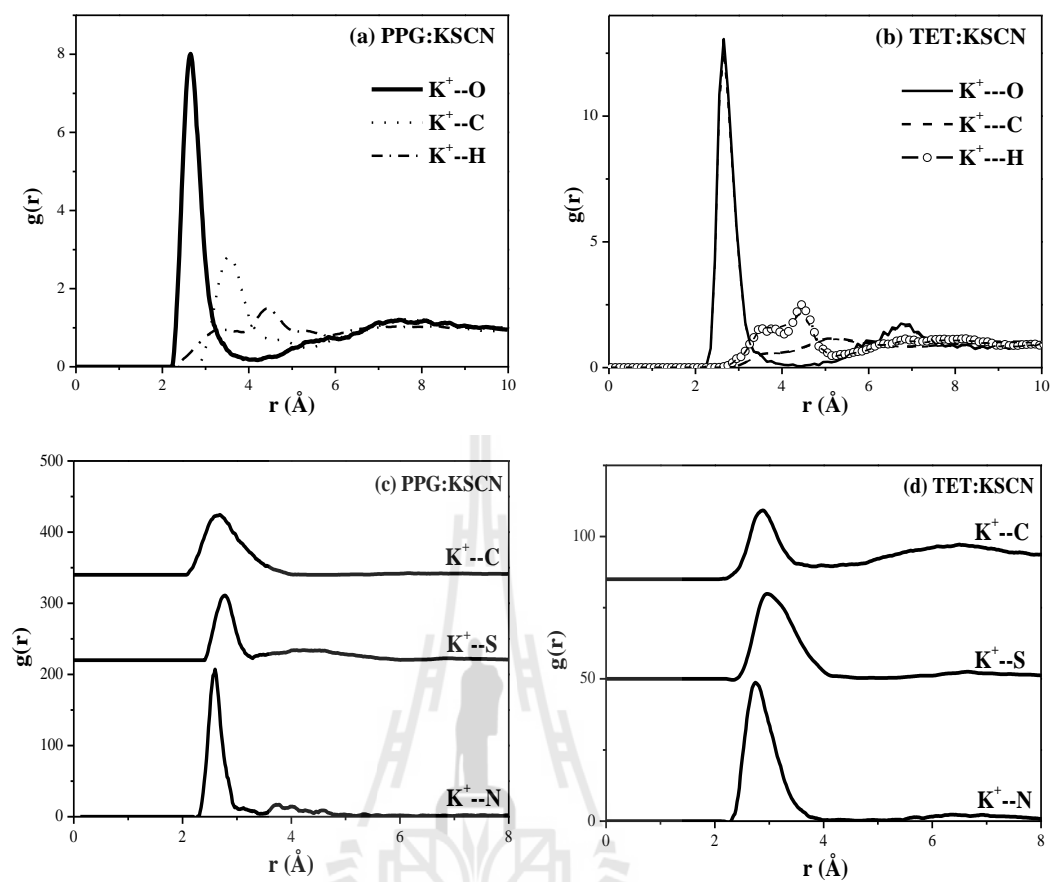
Figure 4.27 Radial distribution functions of (a) K^+-PPG, (b) K^+-TET, (c) K^+-SCN$^-$ in PPG and (d) K^+-SCN$^-$ in TET.

Table 4.11 Parameter characterizing the first peak of RDFs determined from MD of
PPG:KSCN at 300 K.

Correlation	1:20 PPG:KSCN		1:20 TET:KSCN	
	R_0 (Å)	N	R_0 (Å)	N
K^+-O_{PPG}	2.65	3.8	2.65	3.0
K^+-H_{PPG}	3.29	15.6	3.29	15.2
K^+-C_{PPG}	3.55	4.9	3.75	13.4
K^+-N_{SCN}	2.60	0.9	2.77	1.8
K^+-S_{SCN}	2.77	0.9	2.97	1.8
K^+-C_{SCN}	2.69	0.9	2.86	1.8
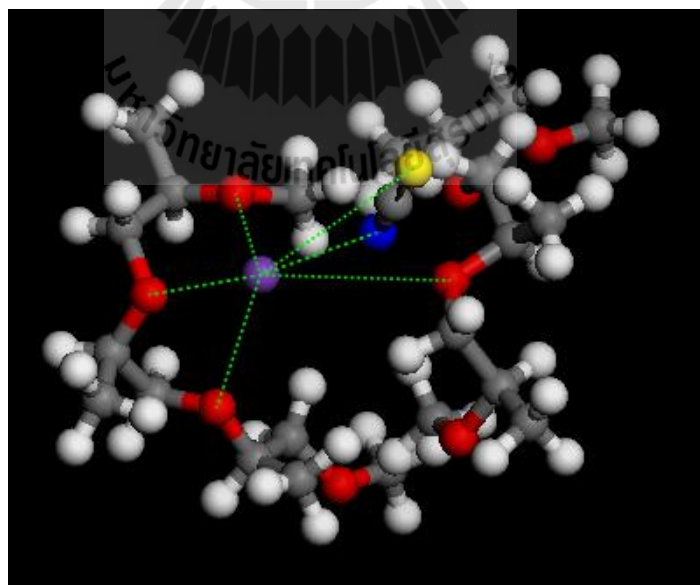
Figure 4.28 Snapshot from MD simulation of PPG:KSCN.
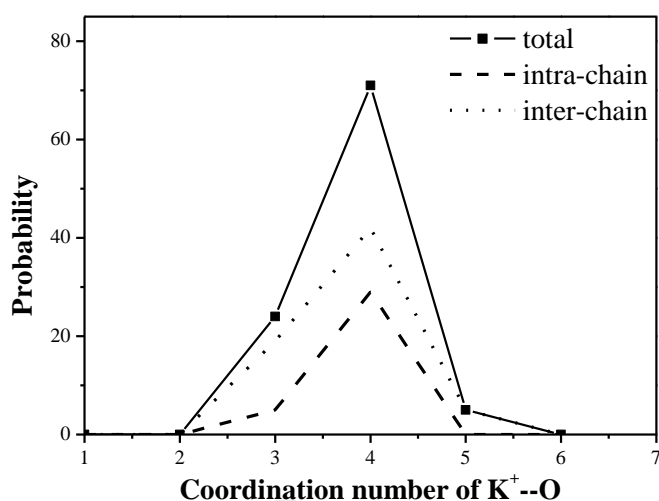
Figure 4.29 Probability of oxygen atoms coordinating a K^+ cation for 1:20 PPG:KSCN system.

4.4.4.3 Ionic conductivity

A comparison of the ionic conductivity for PPG:KSCN and TET:KSCN at room temperature with various salt concentrations is illustrated in Table 4.12 and Figure 4.30. A trend is observed in which the ionic conductivity increases with increasing salt concentration until the ratio of K^+:O is equal to 1:20 for PPG:KSCN and 1:10 for TET:KSCN. This is because increasing salt concentration provides more number of charge carriers. After these ratio, the ionic conductivity decreases at higher salt concentrations. The decrease of ionic conductivity was related to higher percentage of associated ions. A similar trend was also observed by Suthanthiraraj *et al.* (2010) and Chaodamrongsakul (2003). These studies also found that the highest ionic conductivity of PPG:AgCF$_3$SO$_3$ and PEO:KSCN were at 1:16 and 1:8 ratio, respectively. Fraction of free ion calculated by IR spectra exhibit that free ions increase with increasing salt concentration up to the maximum (1:20 for PPG:KSCN

and 1:10 for TET:KSCN). Moreover, IR spectra have the band that is attributed to the ion aggregate when salt concentration is higher than this maximum point.

From the ionic conductivity comparison of PPG:KSCN and TET:KSCN system, TET:KSCN complexes give higher ionic conductivity than that of PPG:KSCN complexes. This is related to a higher coordination number of K^+ ion with PPG ether oxygen than that in TET system. This causes a reduction of ionic mobility. The mean square displacements (MSD) from MD simulation were used to support this conclusion. Mean square displacement is a linear function of time and defined as:

$$D = \frac{1}{6} \lim_{t \to \infty} d < r(t) - r(0) >^2 / dt$$ (the brackets denote an ensemble average). From

Figure 4.31, K^+ ion in PPG diffuse slightly slower than K^+ ion in TET.

Table 4.12 Ionic conductivity of PPG:KSCN and TET:KSCN at room temperature.

K^+:O	Ionic conductivity (S cm^{-1})	
	PPG:KSCN	TET:KSCN
1:5	4.85×10^{-5}	6.45×10^{-3}
1:10	5.57×10^{-5}	7.38×10^{-3}
1:20	6.68×10^{-5}	3.19×10^{-3}
1:30	6.42×10^{-5}	2.62×10^{-3}
1:40	6.00×10^{-5}	2.01×10^{-3}
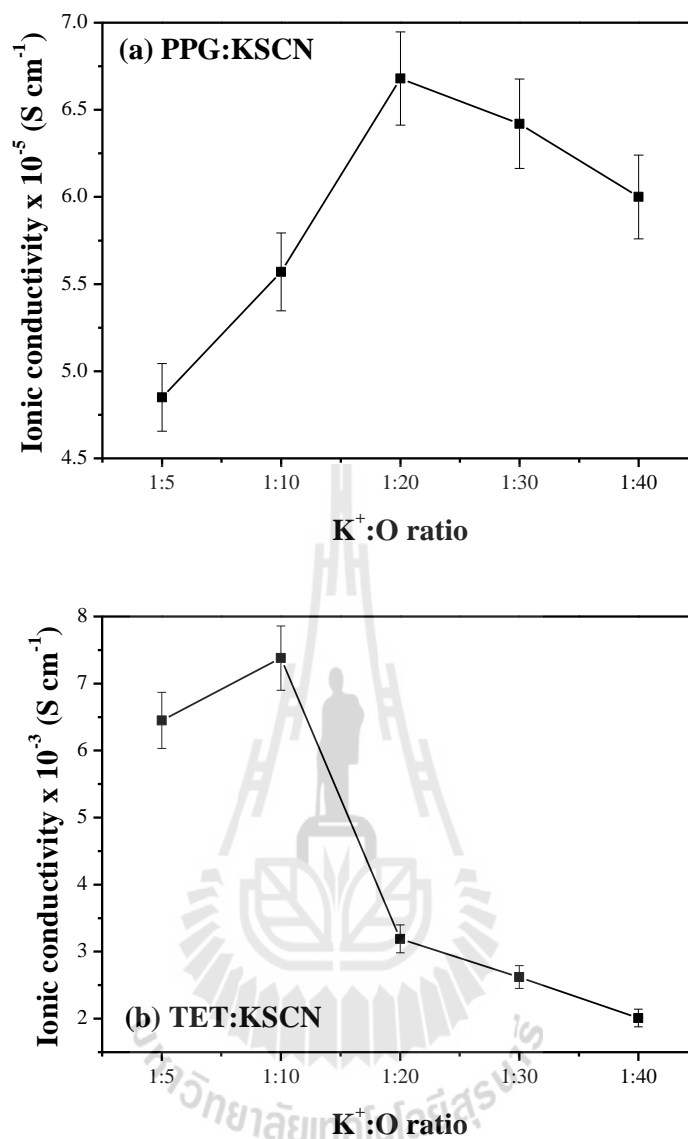
Figure 4.30 Ionic conductivity of (a) PPG:KSCN and (b) TET:KSCN complexes at various K$^+$:O ratio.
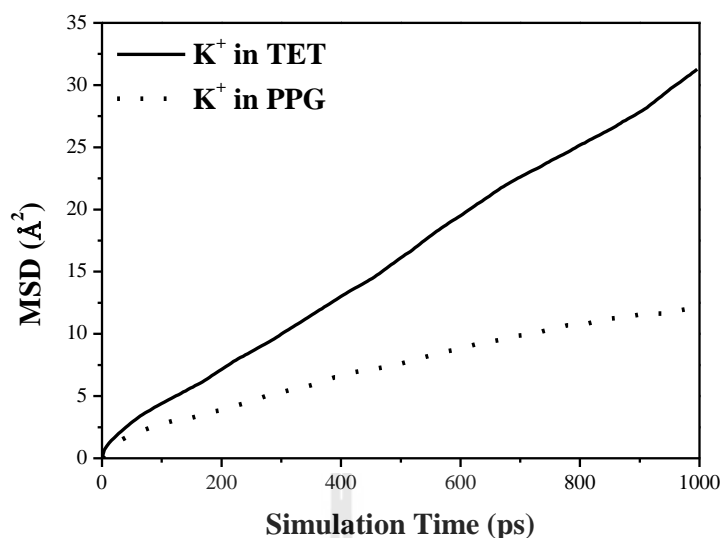
Figure 4.31 Mean square displacement of K^+ ion in PPG and TET at 300 K.

4.4.4.4 EXAFS spectra and MD-EXAFS

As in case of H_2O:KSCN, PVA:KSCN and TET:KSCN, 100 configurations of PPG:KSCN from MD trajectories were selected and extracted to use as an input for MD-EXAFS spectra calculation. In Figure 4.26, the k^2-weighted $\chi(k)$ and $\tilde{\chi}(R)$ plot derived from experimental data were compared with simulated MD-EXAFS spectra for 1:20 PPG:KSCN system. The MD-EXAFS spectra which exclude thiocyanate anion (not shown) were far from agreeable with experimental data. So, as in case of TET:KSCN, the MD-EXAFS spectra of PPG:KSCN must include thiocyanate anion to attain realistic EXAFS spectra. This phenomenon is similar to PPO:NaCF$_3$SO$_3$ system, Schantz *et al.* (Schantz *et al.*, 1988) investigated the symmetric SO_3 stretching for M:O ratio 1:16, 1:8 and 1:5. In all concentrations, the peak at 1037 cm^{-1} is corresponding to ion pair between $CF_3SO_3^-$ and Na^+. The comparison shows an overall good agreement for the phase and frequency of $\chi(k)$ oscillations and $\tilde{\chi}(R)$ plot. It is therefore convinced that the distances and coordination number of K^+-O,

K^+-N, K^+-C_{SCN} and K^+-S obtained from MD simulation were acceptable to study the atomistic solvation structure of PPG:KSCN system.
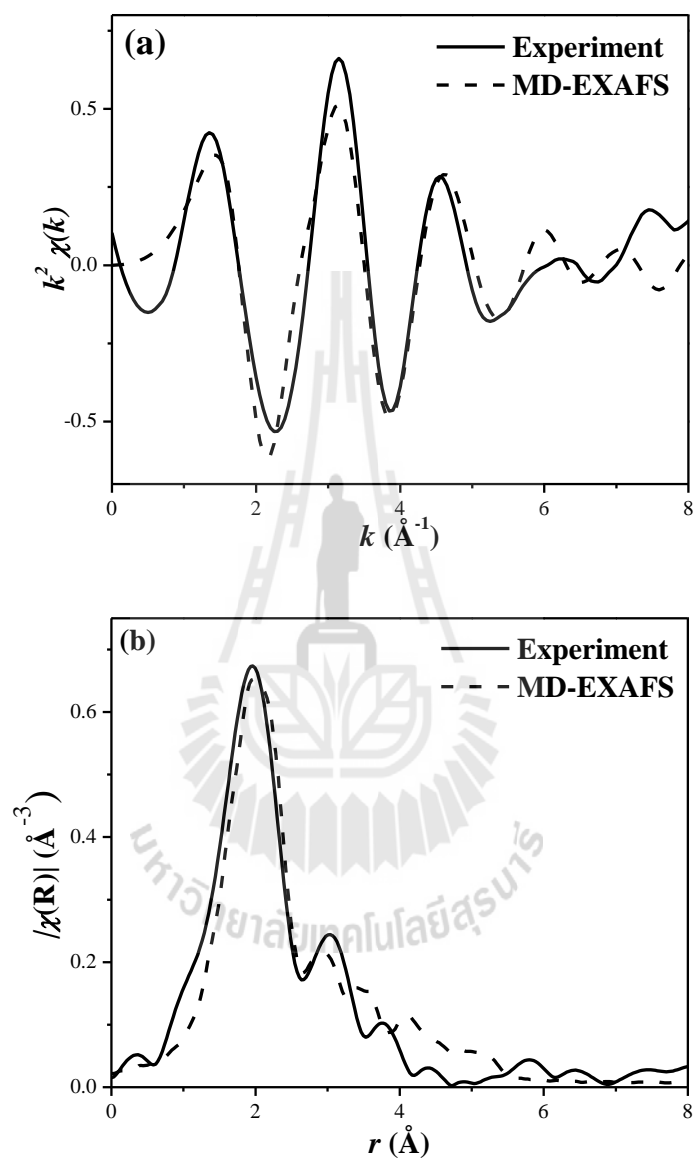
Figure 4.32 Comparison (a) $k^2\chi(k)$ and (b) $|\tilde{\chi}(R)|$ EXAFS spectral from experiment and MD-EXAFS for PPG:KSCN system.

4.5 Conclusions

In this chapter, computer simulation and experimental techniques are combined to describe and interpret the characteristics of the atomistic solvation structures of K^+ in water, poly(vinyl alcohol);PVA, tetraethylene glycol dimethyl ether (TET) and poly(propylene glycol);PPG as the model complexes for solid polymer electrolytes. Molecular simulations with an empirical potential (COMPASS forcefield) were used to calculate the RDFs and local coordination at 300 K. Those structural properties obtained from MD simulations are in good agreement with other previous works. The simulated solvation structures were used to generate the MD-EXAFS spectra for K^+ ions in water, PVA, TET and PPG. MD-EXAFS spectra were then compared with the experimental spectra. Comparison shows the consistence between the EXAFS spectra from MD simulations and those from the experiments. Thus, we suggest that MD simulation with empirical forcefield as well as EXAFS are useful techniques to study the local solvation structures of ionic aqueous solution and model compound representing polymer electrolytes. However, it should be noted that this work only employed smaller molecular systems to represent high molecular weight polymer to calculate MD-EXAFS spectra.

CHAPTER V

MONTE CARLO SIMULATION OF STATIC AND

DYNAMIC PROPERTIESOF BIDISPERSE

POLYETHYLENE OXIDE MIXTURE

The goal of the current MC simulations is to reveal the underlying features of the physical response of the polyethylene Oxide (PEO) matrix upon the insertion of low molecular weight PEO. Before presenting results regarding the bidisperse PEO system, we first focus on the features of the simulations for bulk monodisperse PEO system. The efficiency of the 2nnd simulation parameters for PEO chains, which was discussed in detail in chapter III, would be tested. Once it is verified that the essential physical properties of the PEO system are recovered properly, we will continue with the discussion of the simulation for bidisperse PEO systems.

5.1 Computational Details

For the test simulations, MC simulations for PEO chains were performed on 2nnd high coordination lattice (Rapold and Mattice, 1995; Baschnagel *et al.*, 2000) at the experimental melt density (1.06 g/cm^3) (Orwoll, 1996) using a coarse grained RIS model for unperturbed PEO chains (Doruker *et al.*, 1996). This lattice, which can be constructed by eliminating every other site from a diamond lattice, has a coordination number of 12, which provides flexibility to define a rotational state on the lattice. On

this lattice, the angle between any two axes along the sides of the unit cell was 60°, and the lattice sites were identical to the hexagonal packing of hard spheres.

Both short-range intramolecular interactions and long-range intra- and intermolecular interactions were introduced into simulations. The short-range intramolecular interactions resulting from the local chain conformation were based on the RIS model for an unperturbed chain (Abe *et al.*, 1985), which incorporates the influence of partial charges. The RIS model for PEO chains, in which all bonds are subject to a symmetric 3-fold torsion potential with the nearest neighbor interdependence, is given by the following three statistical weight matrices for three successive bonds of type C-C, C-O, and O-C.

$$
U_{C-C} = \begin{array}{c} \\ t \\ g^+ \\ g^- \end{array} \begin{array}{ccc} t & g^+ & g^- \\ \left(\begin{array}{ccc} 1 & \sigma_{O-O} & \sigma_{O-O} \\ 1 & \sigma_{O-O} & \sigma_{O-O}\omega_{C-O} \\ 1 & \sigma_{O-O}\omega_{C-O} & \sigma_{O-O} \end{array} \right) \end{array} \tag{5.1}
$$

$$
U_{C-O} = \begin{array}{c} \\ t \\ g^+ \\ g^- \end{array} \begin{array}{ccc} t & g^+ & g^- \\ \left(\begin{array}{ccc} 1 & \sigma_{C-C} & \sigma_{C-C} \\ 1 & \sigma_{C-C} & \sigma_{C-C}\omega_{C-O} \\ 1 & \sigma_{C-C}\omega_{C-O} & \sigma_{C-C} \end{array} \right) \end{array} \tag{5.2}
$$

$$
U_{O-C} = \begin{array}{c} \\ t \\ g^+ \\ g^- \end{array} \begin{array}{ccc} t & g^+ & g^- \\ \left(\begin{array}{ccc} 1 & \sigma_{C-C} & \sigma_{C-C} \\ 1 & \sigma_{C-C} & \sigma_{C-C}\omega_{C-C} \\ 1 & \sigma_{C-C}\omega_{C-C} & \sigma_{C-C} \end{array} \right) \end{array} \tag{5.3}
$$

The three accessible rotational isomeric states for each bond were t, g^+, and g^-, used in this order in the matrices. The $\sigma_{C\text{-}C}$ and $\sigma_{C\text{-}O}$ are the statistical weights for the C-C and C-O type first-order interactions, and $\omega_{C\text{-}C}$ and $\omega_{C\text{-}O}$ represent the second-order interactions. They were calculated as Boltzmann factors using the energies listed in Table 5.1. The short-range interactions determine the local chain conformation for an unperturbed chain.

Table 5.1 First- and Second-Order local interactions on the 2nnd lattice for PEO chains.

Interaction	(kJ/mol)
$E\sigma_{C\text{-}C}$	3.2
$E\sigma_{O\text{-}O}$	-2.2
$E\omega_{C\text{-}C}$	∞
$E\omega_{C\text{-}O}$	2.2

Long-range interactions result from bead-bead interaction, which is applied to all pair of beads except for the nearest and second-nearest neighbors in the same molecule. The interaction of the directly bonded beads is constant throughout the simulation and it is ignored. The interactions of the second-nearest pairs are incorporated in the RIS model and are not counted again in the long-range interactions. The long-range interactions are obtained from a discretized form of the LJ potential, in which the second virial coefficient for polymers is evaluated similar to

nonideal gas using the Mayer f function (Cho and Mattice, 1997). However, the LJ parameters for two backbone atoms of PEO are not available since the pairs of two backbone atoms are not always the same. Two different methods were used to estimate σ and ε values.

The σ value is obtained by first noting that $\acute{o}$ for propane is within 1% of $(3/2)^{1/3}\sigma_{\text{ethane}}$. Therefore, the required value of σ for a coarse-grained bead of PEO can be estimated from the data for methyl ether (CH_3OCH_3, $\sigma = 4.307$ Å) as

$$\sigma_{PEO} = (2/3)^{1/3}\sigma_{methylether} \tag{5.4}$$

from which $\sigma_{\text{PEO}} = 3.76$ Å.

The ε value is obtained by fitting the experimental bulk density of PEO at 373 K from series of simulations of free-standing PEO thin films that have different ε values. The density profiles for PEO thin films calculated for σ of 3.76 Å and ε/k_B of 154 K (k_B is the Boltzman constant) yields a cohesive film with a bulk density that most closely matches the experimental density of 1.06 g/cm^3. In Table 5.2, the discretized LJ interactions at 373 K for the first five shells are given. The first shell is strongly repulsive since the distance between two beads, 2.39 Å, is smaller than the value of σ in LJ potential. Both the second and third shells have attractive interaction, which leads to the cohesive nature of polymer and the corresponding thin film. The fourth and higher shells are attractive, but less than the third shell. Use of three shells improves the simulation efficiency with little sacrifice in accuracy.

In order to perform MC moves, the single bead (Doruker and Mattice, 1997) move algorithms is used to attempt at least once for each bead in the system. Acceptance of any move is decided according to the Metropolis criterion. The equilibration of the system is considered to be satisfied when the mean square displacement (MSD) of the centers of mass is higher than $\langle s^2 \rangle$ and the orientation autocorrelation function for the end-to-end vectors (OACF) decays to values close to 0 (Helfer *et al.*, 2003).

Table 5.2 Long-range interaction shell energy obtained from the averaging process.

Shell	Shell energy (kJ/mol)
1	8.113
2	-0.213
3	-0.339
4	-0.067
5	-0.017

5.2 Results and Discussion

5.2.1 Single Chain

The statistic and dynamic characteristics of a single isolated chain based on our simulation are presented in Figure 5.1. All slopes shown in Figure 5.1 are based on data regression. The mean square of radius of gyration, $\langle s^2 \rangle$, scales with the molecular weight to the power 1.12, close to the theoretical predication, 1.2, for the expanded chains in dilute solutions. Because the dynamic Monte Carlo is based on stochastic monomer motions without hydrodynamic interactions, instead of Zimm dynamics, Rouse dynamics is expected if the algorithm is correct (Binder and Paul, 1997). Besides, our results show that D is inversely proportional to molecular weight (MW), which is also predicted by Rouse theory.
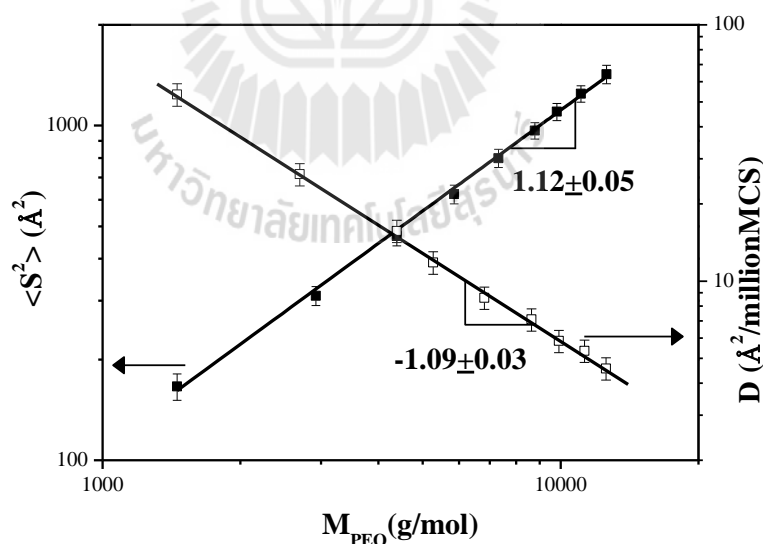
Figure 5.1 The diffusion coefficient (D) and the mean square radius of gyration $\langle s^2 \rangle$ of a single PEO chain plotted against molecular weight.

In Figure 5.2, the relaxation time (τ_{ee}), is obtained from fitting the auto correlation function of the end-to-end vectors to Equation (5.5) with τ_{ee} as the only parameter:

$$\langle R_e(t).R_e(0)\rangle \quad = \quad Nb^2 \sum_{p:odd}\frac{8}{p^2\,\pi^2}\exp\!\left(-p^2 t/\tau_{ee}\right) \tag{5.5}$$

The equation was derived from Rouse theory and has been found identical to the one derived from Reptation theory (Doi, 1986). The resulting τ_{ee} is plotted against M. The regression shows that τ scales with M to the power 2.08, which is close to the Rouse prediction, 2, but a little lower than 2.2, which is the theoretical prediction allowing the excluded volume effects. Some may still argue that Equation (5.5) is not valid for longer chains here because Rouse theory always assumes Gaussian statistics which is absent for a single chain in its good solvent, in which $\langle s^2\rangle$ scales with M to 1.2 instead of 1. Although this is a legitimate argument, approximating a diluted long chain to the Gaussian distribution was acceptable because the final scaling results are not very sensitive to this approximation as seen in Zimm theory (Doi, 1986). Therefore, this algorithm has yielded the expected dimension scaling law and the Rouse-like dynamics for chains longer than 200 g/mol.
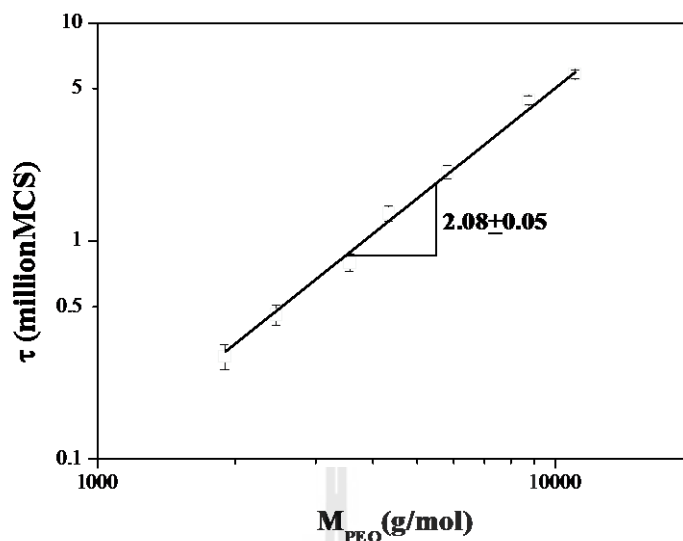
Figure 5.2 The relaxation time of end-to-end vectors versus molecular weight for single chain simulations.

5.2.2 Equilibration of PEO Melt System

Firstly, we perform a set of 10 million MCS simulations for 56 PEO chains, each having 100 coarse-grained beads, to ensure that the simulated systems reach equilibrium. The simulation temperature is at 373 K, which is well above the melting temperature of PEO chains. An insertion of 5600 coarse-grained beads into the 2nnd lattice with the periodic boundary conditions (box size = 30 unit) in all three directions meets the experimental bulk density of PEO chains ($\approx$ 1.06 g/cm^3). Equilibration can be verified by a decay of the orientation autocorrelation function (OACF) of end-to-end vectors and mean square displacement of the centers of mass (MSD). OACF and MSD profiles are shown in Figure 5.3 and Figure 5.4, respectively.
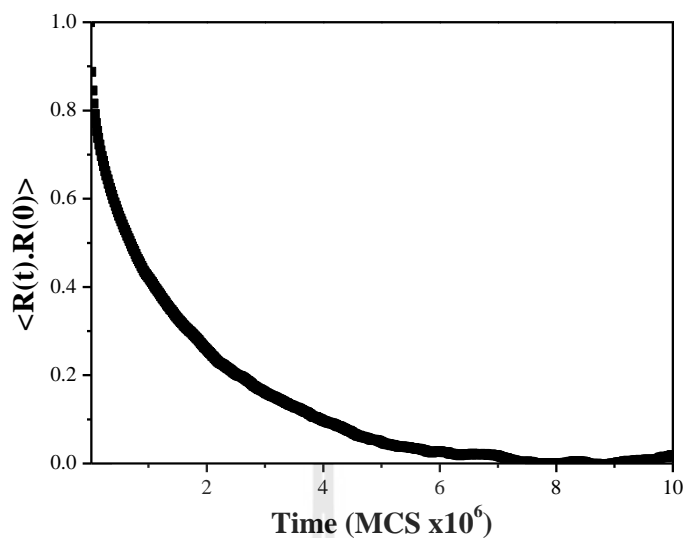
Figure 5.3 Orientation auto correlation function (OACF) of end-to-end vectors of PEO chains in test simulation. All of 56 parent chains of 100 coarse-grained beads were used.
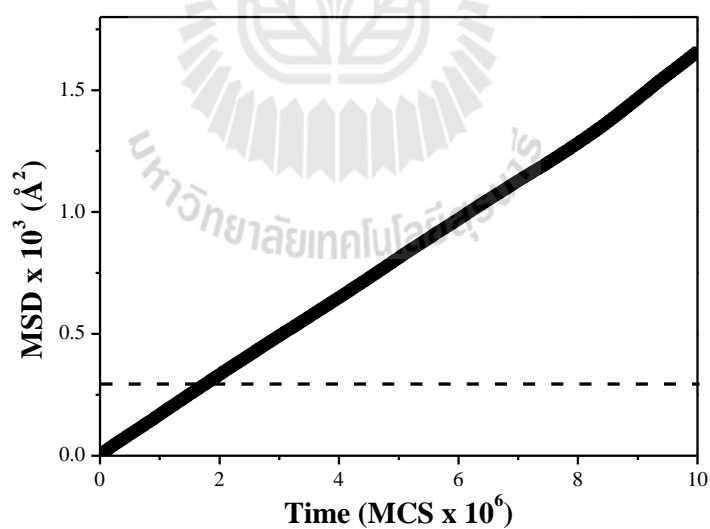
Figure 5.4 Mean-square displacement of the center of mass ($g_{cm}(t)$) of PEO chains in test simulation. All 56 parent chains of 100 coarse-grained beads were used. The value of $\langle s^2 \rangle$ is 274.1 ± 0.5 Å^2, which is represented by the horizontal dashed line.

The criterion to confirm whether equilibration has been reached is the time elapsed for OACF to come to 1/e (~0.37). The time required for OACF to fall to 0 practically means that the system is well-equilibrated and the final conformations of all chains are completely independent from the starting conformations. In this particular example in which we make a test simulation for 56 PEO parent chains, equilibrium conditions are well satisfied after 4 million MC steps. Besides, mean square displacement (MSD) of the center of mass $g_{cm}(t)$ of PEO chains has also been analyzed for the test simulation. From Figure 5.4, it can be agreed that the equilibrium condition is satisfied before 4 million MCS. It is well-confirmed that the system can reach equilibrium condition at the early stage of simulation. For subsequent simulation, at least 10 million MCS will be performed for data analysis, which is well-above the simulation time required for assuring equilibrium considerations.

5.2.3 Monodisperse PEO Chains

It is a well-known fact that $\langle s^2 \rangle$ scales with M under Θ conditions. The melt state can be also considered as analogous to the Θ-state in terms of scaling prediction in which, the dimensions of polymer chains in bulk are proportional to the changes in molecular weight (MW). Figure 5.5 shows the existence of such a well-defined behavior illustrated for sufficiently long polymer chains. The slope of log(MW) versus $\log\langle s^2 \rangle$ line is 1.07 ± 0.04. Thus, the universal scaling law is satisfied reasonably well when the chains are sufficiently long.

In order to verify the statistics of PEO chains, the ratios of mean square end-to-end distance and mean square radius of gyration, $\langle r^2 \rangle / \langle s^2 \rangle$, are plotted against MW in Figure 5.6. This expected ratio for Gaussian chains equals to 6. From Figure 5.6,

short chains are significantly non-Gaussian as the ratio indicates (Mattice *et al.*, 2004). The ratio gradually approaches 6 as the chain is getting longer at MW ~3,000 g mol^{-1}.
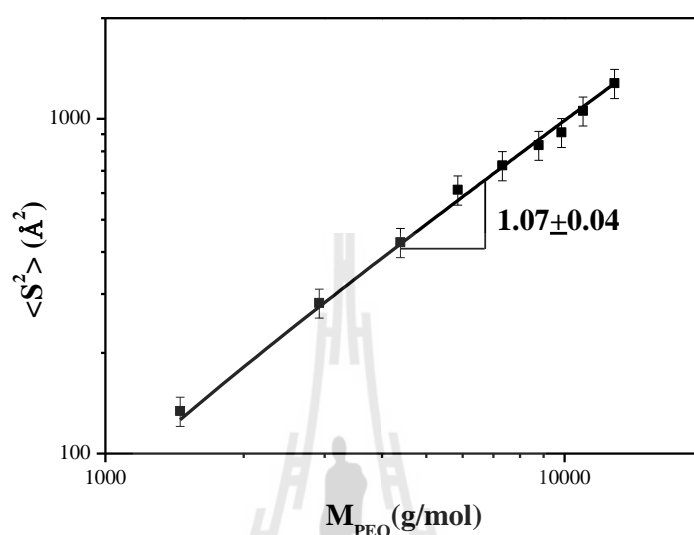
Figure 5.5 The mean square radius of gyration $\langle s^2 \rangle$ of monodisperse system plotted against molecular weight.
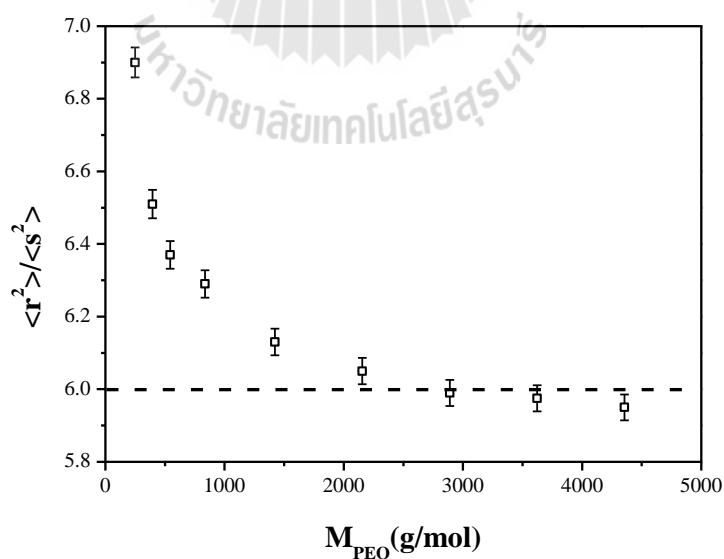
Figure 5.6 The ratios of mean square end-to-end distance and mean square radius of gyration, $\langle r^2 \rangle / \langle s^2 \rangle$, versus molecular weight.

The major purpose of our algorithm is to model the dynamic properties, especially the molecular diffusion in PEO melts, which can be extracted directly from the simulation. Figure 5.7 shows a popular plot for the mean square displacement of the center of mass from N20, N40, N60, N80 and N100 beads. The diffusion coefficient can be calculated from these curves and the results are given in Table 5.3. The translation motion of the center of mass of short chains seems to be faster than that of the long chains during the entire simulation. The high mobility of short chains are probable as the shorter chain can relax faster than the longer ones. These results are consistent with Monte Carlo simulations of multichain systems in dense cubic lattice (Ngai and Skolnick, 1991). They pointed out that as chain length increases, the self-diffusion coefficient of center of mass decreases, presumably reflecting more and more constrained motion.
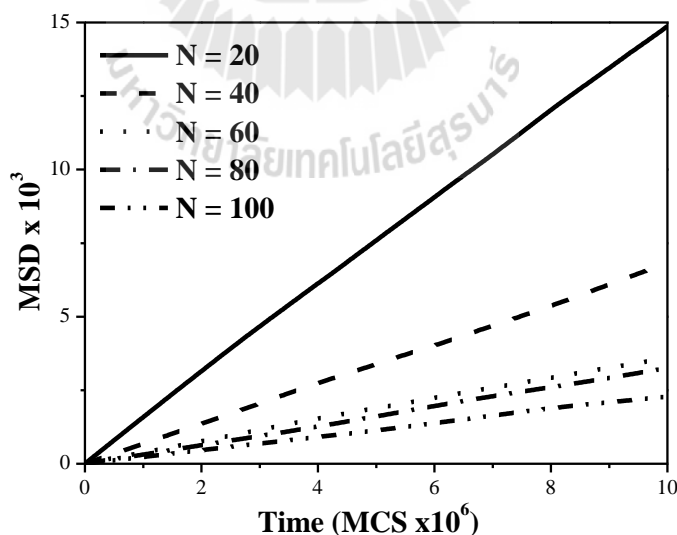

Figure 5.7 MSD of monodisperse PEO of length N=20, 40, 60, 80 and 100.

Table 5.3 Diffusion coefficients (D) of monodisperse PEO.

Chain length (N)	D (Å^2/millionMCS)
20	2.47
40	1.12
60	0.60
80	0.55
100	0.39

5.2.4 Bidisperse PEO Chains

MC simulations of probed chains (N_p) dissolved in matrix (N_m), have also been performed. All MC simulations were performed at a fixed weight fraction at $\phi_m = \phi_p = 0.5$, where ϕ_m and ϕ_p are volume fraction of probed and matrix polymers, respectively. Only the static and dynamic properties of probed chain consisting of $N_p = 100$ segments in the matrix of chains length of $N_m = 10$ up to $N_m = 75$ have been simulated.

The static properties of both probed and matrix polymer components have been checked. Figure 5.8 and Table 5.4 are results of mean square radius of gyration $\langle s^2 \rangle$ of $N_p = 100$ in matrix polymer with varied molecular weight. As expected, no systematic dimension change was found. For example, $\langle s^2 \rangle$ of matrix polymer ($N_m = 25$) are 60.28 ± 5.7 and 60.63 ± 6.1 Å for monodisperse and bidisperse system, respectively. These results are similar to MC simulation on a high coordination lattice (2nnd) of bidisperse polyethylene ($M_w = 1 \times 10^3$ and 4.5×10^3 g/mol), which exhibit

no change in chain dimension against the weight concentration of 1×10^3 g/mol (Lin *et al.*, 2006). The expected scaling law of polymer dimensions in the bidisperse system is that $<s^2>$ should be proportional to $M^{1.0}$. In Figure 5.9, a similar interesting feature was also observed here as seen in monodisperse system *i.e.* $<s^2> \sim M^{1.06}$.
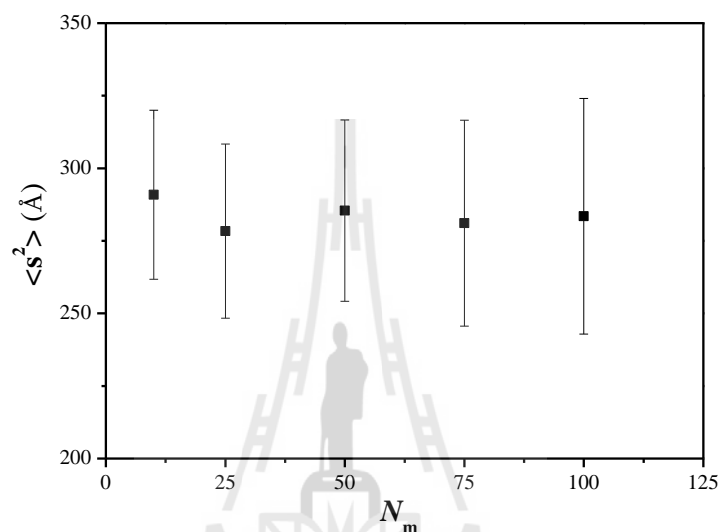
Figure 5.8 The mean square radius of gyration $\langle s^2 \rangle$ of $N_p = 100$ in the mixture against the chain length of $N_m = 10$ to 75.

Table 5.4 Mean square radius of gyration $\langle s^2 \rangle$ of bidisperse PEO at $\phi_p = 0.5$.

System	$\langle s^2 \rangle_{Np = 100} \pm$ S.D.
$N_m = 10$	290.9 ± 29.1
$N_m = 25$	278.4 ± 30.0
$N_m = 50$	285.4 ± 31.2
$N_m = 75$	281.1 ± 35.5
$N_p = 100$	283.5 ± 40.6
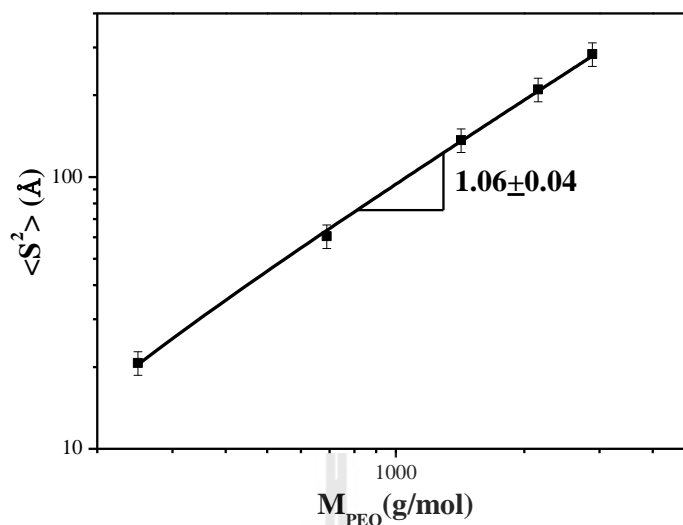
Figure 5.9 The mean square radius of gyration $\langle s^2 \rangle$ of bidisperse system plotted against molecular weight.

To study dynamic properties of bidisperse PEO, the mean square displacement (MSD) of N_p=100 in N_m=10-75 are ploted in Figure 5.10. Starting from the monodisperse with $N_p = N_m$, we can consider what happens if N_m is reduced such that $N_m < N_p$. The shorter matrix chains would relax faster than the probed chain, and therefore the dynamic constraints imposed on the probed chain should be reduced. In other word, part of the dynamical constraints in N_p is mitigated in a matrix with $N_m < N_p$. This behavior can be seen in Figure 5.11 which show probed chain in bidisperse system which relax faster than that in monodisperse system. Accordingly, MSD plot show the faster translation motion of probed chain in short matrix chain than that of probed chain in monodisperse system. If the matrix chain is sufficiently large nearly to the probe chain, the MSD of probed chain seem to be close to MSD of monodisperse. A similar behavior was also observed in dynamics of probed chain in matrix of different degrees of polymerization (Ngai and Skolnick, 1991). From the

published results, in binary blend system which increasing chain length of matrix chain, the matrix chain relaxation is shifted to longer times (Figure 5.12), consistent with the MSD plot which show slower matrix chain mobility in bidisperse system compared to that in monodisperse system (Figure 5.13).
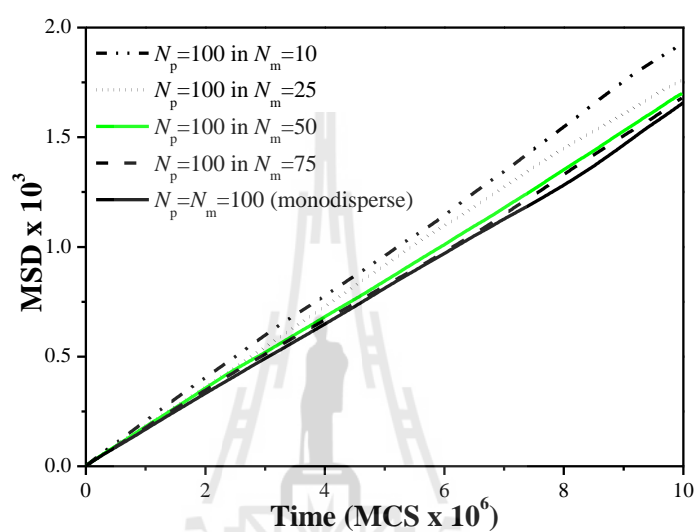
Figure 5.10 Mean square displacement of N_p=100 in N_m=10-75.
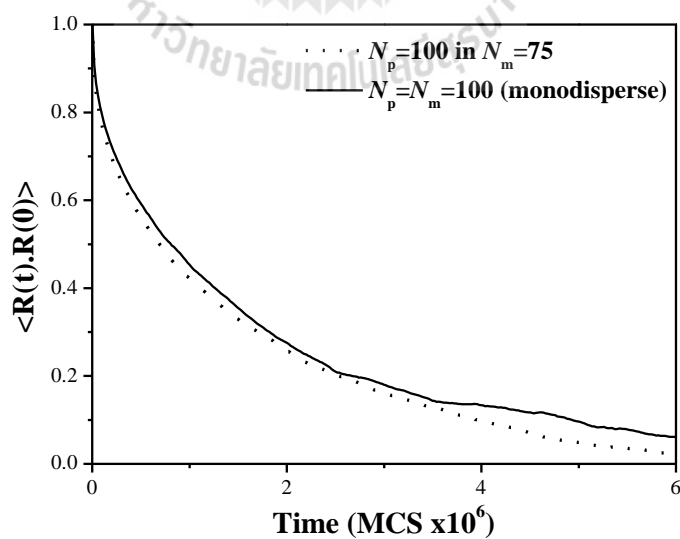
Figure 5.11 Orientation auto correlation function (OACF) of the end-to-end vectors of N_p=100 in mono- and bi-disperse system.
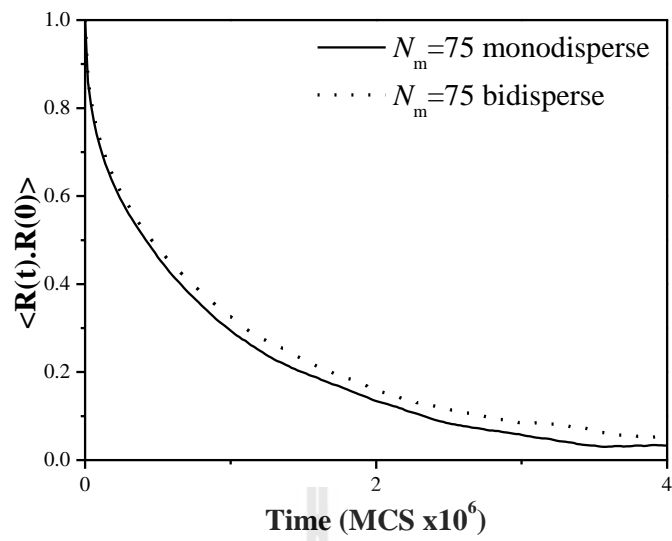
Figure 5.12 Orientation auto correlation function (OACF) of the end-to-end vectors of N_m=75 in mono- and bi-disperse system.
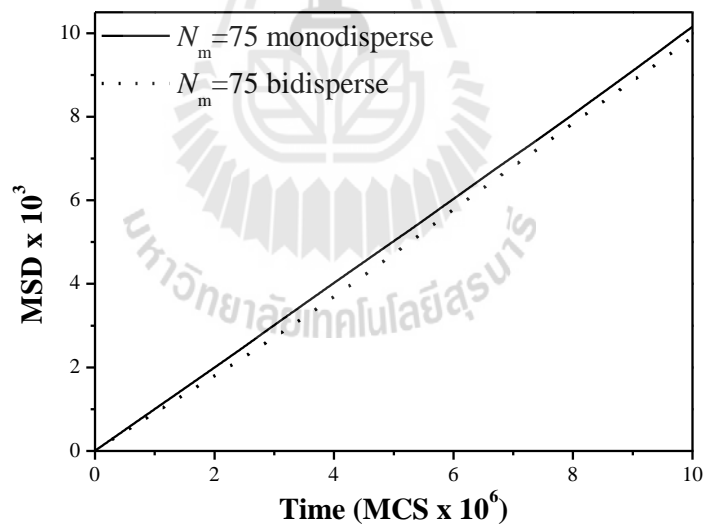
Figure 5.13 Mean square displacement of N_m=75 in mono- and bi-disperse system.

To verify that the system has not segregated, the intermolecular pair correlation function (PCF) is evaluated the various systems included in this study. This PCF function gives the probability of finding a particle A at a specified distance from another particle A on the high coordination lattice defined by Equation (5.6).

$$g_{AA}(i) \quad = \quad \frac{\langle n_{AA}(i) \rangle}{(10i^2+2)V_A}$$ (5.6)

In Equation (5.6), $n_{AA}(i)$ is the number occupancy of A in the ith shell from another A particle and V_A is the volume fraction of A in the entire system. Beads on the same chain are ignored in the evaluation of the intermolecular PCF.

In bidisperse system, intermolecular PCF as a function of shell number, which indicates the distance away from a given bead, is shown in Figure 5.14. It can be suggest that short chain (N_m=10) stay closer to longer chain (N_p=100) than the long matrix chain (N_m =75). Therefore, simulation provides no evidence for segregation of the bidisperse system. All of results (MSD, OACF and PCF) indicates that insertion of short chain enhance the long probed chain to move and relax faster than that of monodisperse system and no phase separate is observed in bidisperse system. These results may be related to an increased ionic conductivity of plasticized polymer electrolytes when adding low molecular weight renders mobility of high molecular weight.
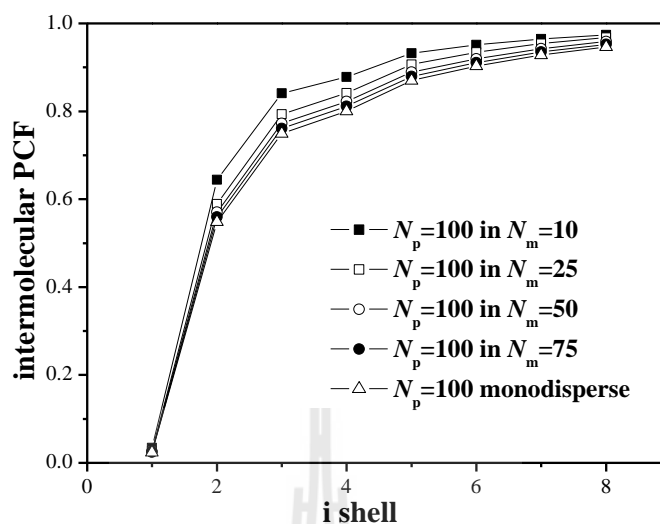
Figure 5.14 Five types of intermolecular pair correlation functions (PCF) as a function of shell number.

5.3 Conclusions

In this chapter, Monte Carlo simulation of coarse-grained PEO model on a high coordination lattice was used in simulating bidisperse PEO mixture. Static and dynamic properties were studied. In monodisperse system, dimensions of PEO chains in bulk ($\log\langle s^2 \rangle$) are proportional to the change in molecular weight ($\log$(MW)) and consistent with the universal scaling law. In bidisperse system, there is no systemic dimension change of both probed and matrix components. MSD results show the probed chain in bidisperse system with shorter matrix chains move faster than the probed chain in monodisperse system.
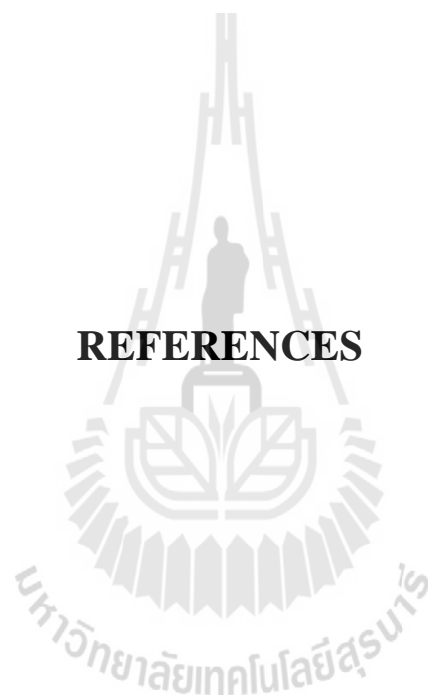
REFERENCES

REFERENCES

Abe, A. and Mark, J. E. (1976). Conformational energies and the random-coil dimensions and dipole moments of the polyoxides $CH_3O[(CH_2)_yO]_xCH_3$. **Journal of the American Chemical Society**. 98: 6468-6476.

Abe, A., Tasaki, K. and Mark, J. E. (1985). Rotational Isomeric State Analysis of Poly(oxyethylene). Conformational Energies and the Random-Coil Configuration. **Polymer Journal**. 17: 883.

Abraham, K. M. and Alamgir, M. (1993). Ambient temperature rechargeable polymer-electrolyte batteries. **Journal of Power Sources**. 43: 195-208.

Acosta, J. L. and Morales, E. (1996). Structural, morphological and electrical characterization of polymer electrolytes based on PEO/PPO blends. **Solid State Ionics**. 85: 85-90.

Ahlstrom, P., Borodin, O., Wahnstrom, G., Wensink, E. J. W., Carlsson, P. and Smith, G. D. (2000). Molecular-dynamics simulation of structural and conformational properties of poly(propylene oxide). **The Journal of Chemical Physics**. 112: 10669-10679.

Allcock, H. R., Austin, P. E., Neenan, T. X., Sisko, J. T., Blonsky, P. M. and Shriver, D. F. (1986). Polyphosphazenes with etheric side groups: prospective biomedical and solid electrolyte polymers. **Macromolecules**. 19: 1508-1512.

Allen, M. P. (2004). **Introduction to molecular dynamics simulation** [On-line]. Available: http://www.fz-juelich.de/nic-series/volume23/allen.pdf.

Allen, M. P., Tildesley, D. J. (1987). **Computer Simulation of Liquids**. Oxford: Oxford University Press.

Andrea Di, C. (1996). Short-range order in solid and liquid KBr probed by EXAFS. **Journal of Physics: Condensed Matter**. 8: 10779.

Angell, C. A. (1983). Fast ion motion in glassy and amorphous materials. **Solid State Ionics**. 9-10: 3-16.

Angell, C. A., Liu, C. and Sanchez, E. (1993). Rubbery solid electrolytes with dominant cationic transport and high ambient conductivity. **Nature**. 362: 137-139.

Aono, H., Imanaka, N. and Adachi, G.-y. (1994). High Li$^+$ Conducting Ceramics. **Accounts of Chemical Research**. 27: 265-270.

Armand, M. B. (1986). Polymer Electrolytes. **Annual Review of Materials Science**. 16: 245-261.

Astrup, E. E. (1979). An Investigation of the Molecular Structure and Conformation of 1,2-Dimethoxyethane, CH_3-O-CH_2-CH_2-O-CH_3, in the Gas Phase. **Acta Chemica Scandinavica**. A33: 655-664.

Ballard, D. G. H., Cheshire, P., Mann, T. S. and Przeworski, J. E. (1990). Ionic conductivity in organic solids derived from amorphous macromolecules. **Macromolecules**. 23: 1256-1264.

Bandara, H. M. N., Schlindwein, W. S., Latham, R. J. and Linford, R. G. (1994). Comparison of the cation environment in polymer electrolytes based on poly(ethylene oxide) and transition-metal bromides. **Journal of the Chemical Society, Faraday Transactions**. 90: 3549-3553.

Bange, K. and Gambke, T. (1990). Electrochromic Materials for optical switching devices. **Advanced Materials**. 2: 10-16.

Bannister, D. J., Davies, G. R., Ward, I. M. and McIntyre, J. E. (1984). Ionic conductivities of poly(methoxy polyethylene glycol monomethacrylate) complexes with $LiSO_3CH_3$. **Polymer**. 25: 1600-1602.

Barton, A. (1991). **CRC handbook of solubility parameters and other cohesion parameters (2nd ed)**. CRC Press.

Baschnagel, J., Binder, K., Doruker, P., Gusev, A., Hahn, O., Kremer, K., Mattice, W., Müller-Plathe, F., Murat, M., Paul, W., Santos, S., Suter, U. and Tries, V. (2000). **Advances in Polymer Science**. Vol. 152, **Viscoelasticity, Atomistic Models, Statistical Chemistry**. pp. 41-156. Heidelberg: Springer Berlin.

Bernson, A. and Lindgren, J. (1993). Free ions and ion pairing/clustering in the system $LiCF_3SO_3$---PPO_n. **Solid State Ionics**. 60: 37-41.

Bernson, A., Lindgren, J., Huang, W. and Frech, R. (1995). Coordination and conformation in PEO, PEGM and PEG systems containing lithium or lanthanum triflate. **Polymer**. 36: 4471-4478.

Berthier, C., Gorecki, W., Minier, M., Armand, M. B., Chabagno, J. M. and Rigaud, P. (1983). Microscopic investigation of ionic conductivity in alkali metal salts-poly(ethylene oxide) adducts. **Solid State Ionics**. 11: 91-95.

Bhargav, P. B., Mohan, V. M., Sharma, A. K. and Rao, V. V. R. N. (2009). Investigations on electrical properties of (PVA:NaF) polymer electrolytes for electrochemical cell applications. **Current Applied Physics**. 9: 165-171.

Bhattacharja, S., Smoot, S. W. and Whitmore, D. H. (1986). Cation and anion diffusion in the amorphous phase of the polymer electrolyte (PEO)$_8$ LiCF$_3$SO$_3$. **Solid State Ionics**. 18-19: 306-314.

Binder, K. (1995). **Monte Carlo and Molecular Dynamics simulations in polymer science**. Oxford: Oxford University Press.

Binder, K. and Paul, W. (1997). Monte Carlo simulations of polymer dynamics: Recent advances. **Journal of Polymer Science Part B: Polymer Physics**. 35: 1-31.

Bird, R. B. (1977). **Dynamics of polymeric liquids**. New York: Wiley.

Blonsky, P. M., Shriver, D. F., Austin, P. and Allcock, H. R. (1984). Polyphosphazene solid electrolytes. **Journal of the American Chemical Society**. 106: 6854-6855.

Blonsky, P. M., Shriver, D. F., Austin, P. and Allcock, H. R. (1986). Complex formation and ionic conductivity of polyphosphazene solid electrolytes. **Solid State Ionics**. 18-19: 258-264.

Bonino, F., Ottaviani, M., Scrosati, B. and Pistoia, G. (1988). A Polymeric Electrolyte Rechargeable Lithium Battery. **Journal of The Electrochemical Society**. 135: 12-15.

Borodin, O. and Smith, G. D. (1998). Molecular Dynamics Simulations of Poly(ethylene oxide)/LiI Melts. 1. Structural and Conformational Properties. **Macromolecules**. 31: 8396-8406.

Botti, A., Pagnotta, S. E., Bruni, F. and Ricci, M. A. (2009). Solvation of KSCN in Water. **The Journal of Physical Chemistry B**. 113: 10014-10021.

Boukamp, B. A. and Huggins, R. A. (1978). Fast ionic conductivity in lithium nitride. **Materials Research Bulletin**. 13: 23-32.

Bruce, P. G. (1995). **Solid State electrochemistry**. United Kingdom: Cambridge University Press.

Bruce, P. G. and Vincent, C. A. (1993). Polymer electrolytes. **Journal of the Chemical Society, Faraday Transactions**. 89: 3187-3203.

Chadwick, A. V., Strange, J. H. and Worboys, M. R. (1983). Ionic transport in polyether electrolytes. **Solid State Ionics**. 9-10: 1155-1160.

Chandra, A. and Chandra, S. (1994). Mixed-anion effect in polyethylene-oxide-based sodium-ion-conducting polymer electrolytes. **Journal of Physics D: Applied Physics**. 27: 2171-2179.

Chandrasekaran, R. M., I. R. Vasanthi, R. and Selladurai, S. (2001). **Bulletin of Electrochemistry**. 17: 249.

Chaodamrongsakul, J. (2003). **Structures and Properties of Solid Polymer Electrolytes: Poly(ethylene oxide)/ Poly(ethylene glycol)/Salts Systems**. M. Sc. Thesis, Suranaree University of Technology, Thailand.

Chatani, Y. and Okamura, S. (1987). Crystal structure of poly(ethylene oxide)--sodium iodide complex. **Polymer**. 28: 1815-1820.

Chiang, C. K., Davis, G. T., Harding, C. A. and Takahashi, T. (1985). Polyethylenimine-sodium iodide complexes. **Macromolecules**. 18: 825-827.

Chintapalli, S. (1996). **Structural characterization of polymer-salt complexes and the role of plasticizers in ionic transport**. Ph. D. Dissertation, University of Oklahoma Graduate College, USA.

Chintapalli, S. and Frech, R. (1996). Effect of Plasticizers on Ionic Association and Conductivity in the $(PEO)_9LiCF_3SO_3$ System. **Macromolecules**. 29: 3499-3506.

Cho, J. and Mattice, W. L. (1997). Estimation of Long-Range Interaction in Coarse-Grained Rotational Isomeric State Polyethylene Chains on a High Coordination Lattice. **Macromolecules**. 30: 637-644.

Clancy, S., Shriver, D. F. and Ochrymowycz, L. A. (1986). Preparation and characterization of polymeric solid electrolytes from poly(alkylene sulfides) and silver salts. **Macromolecules**. 19: 606-611.

Cohen, M. H. and Turnbull, D. (1959). Molecular Transport in Liquids and Glasses. **The Journal of Chemical Physics**. 31: 1164-1169.

Colboum, E. A. (1994). **Computer simulation of polymers**. Longman Scientific & Technical.

Cole, K. S. and Cole, R. H. (1941). Dispersion and Absorption in Dielectrics I. Alternating Current Characteristics. **The Journal of Chemical Physics**. 9: 341-351.

Coleman, M. M. and Painter, P. C. (1995). Hydrogen bonded polymer blends. **Progress in Polymer Science**. 20: 1-59.

Cowie, J. M. G. and Cree, S. H. (1989). Electrolytes Dissolved in Polymers. **Annual Review of Physical Chemistry**. 40: 85-113.

Curtiss, L. A. and Gordon, M. S. (2004). **Computational materials chemistry: Methods and applications**. London: Kluwer.

D'Angelo, P., Di Nola, A., Filipponi, A., Pavel, N. V. and Roccatano, D. (1994). An extended x-ray absorption fine structure study of aqueous solutions by employing molecular dynamics simulations. **The Journal of Chemical Physics**. 100: 985-994.

D'Angelo, P., Di Nola, A., Mangoni, M. and Pavel, N. V. (1996). An extended x-ray absorption fine structure study by employing molecular dynamics simulations: Bromide ion in methanolic solution. **The Journal of Chemical Physics**. 104: 1779-1790.

D'Angelo, P., Nola, A. D., Giglio, E., Mangoni, M. and Pavel, N. V. (1995). EXAFS Study of Micellar Aggregates of Bile Acid Rubidium Salts. **The Journal of Physical Chemistry**. 99: 5471-5480.

D'Angelo, P. and Pavel, N. V. (1999). Evidence of three-body correlation functions in Rb^+ and Sr^{2+} acetonitrile solutions. **The Journal of Chemical Physics**. 111: 5107-5115.

Dang, L. X., Schenter, G. K., Glezakou, V.-A. and Fulton, J. L. (2006). Molecular Simulation Analysis and X-ray Absorption Measurement of Ca^{2+}, K^+ and Cl^- Ions in Solution. **The Journal of Physical Chemistry B**. 110: 23644-23654.

Davison, W. H. T. (1955). Infrared spectra and crystallinity. Part III. Poly(ethylene glycol). **Journal of the Chemical Society (Resumed)**. 3270-3274.

de Gennes, P. G. (1979). **Scaling concepts in polymer physics**. New York: Cornell University Press.

De La Rosa, A., Heux, L., Cavaillé, J. Y. and Mazeau, K. (2002). Molecular modeling of the mobility of poly(allyl alcohol), PAA, and poly(vinyl alcohol), PVA. **Polymer**. 43: 5665-5677.

Decha, P. (2002). **Effect of adding poly(propylene oxide) on structures and properties of poly(ethylene oxide)/salt solid electrolytes**. M. Sc. Thesis, Suranaree University of Technology, Thailand.

Dhumal, N. R. and Gejji, S. P. (2006a). Theoretical studies in local coordination and vibrational spectra of $M^+CH_3O(CH_2CH_2O)_nCH_3$ (n = 2-7) complexes (M = Na, K, Mg and Ca). **Chemical Physics**. 323: 595-605.

Dhumal, N. R. and Gejji, S. P. (2006b). Theoretical studies on blue versus red shifts in diglyme-M^+-X^- (M=Li, Na, K and X=BF_4, ClO_4, SCN). **Journal of Molecular Structure: THEOCHEM**. 758: 233-240.

Di Cicco, A., Minicucci, M. and Filipponi, A. (1997). New Advances in the Study of Local Structure of Molten Binary Salts. **Physical Review Letters**. 78: 460.

Dias, F. B., Plomp, L. and Veldhuis, J. B. J. (2000). Trends in polymer electrolytes for secondary lithium batteries. **Journal of Power Sources**. 88: 169-191.

Doi, M. and Edwards, S. F. (1986). **The theory of polymer dynamic**. Clarendon, Oxford.

Dong, H., Hyun, J.-K., Rhodes, C. P., Frech, R. and Wheeler, R. A. (2002). Molecular Dynamics Simulations and Vibrational Spectroscopic Studies of Local Structure in Tetraglyme:Sodium Triflate ($CH_3O(CH_2CH_2O)_4CH_3$:$NaCF_3SO_3$) Solutions. **The Journal of Physical Chemistry B**. 106: 4878-4885.

Doruker, P. and Mattice, W. L. (1997). Reverse Mapping of Coarse-Grained Polyethylene Chains from the Second Nearest Neighbor Diamond Lattice to an Atomistic Model in Continuous Space. **Macromolecules**. 30: 5520-5526.

Doruker, P. and Mattice, W. L. (1998). Simulation of Polyethylene Thin Films on a High Coordination Lattice. **Macromolecules**. 31: 1418-1426.

Doruker, P., Rapold, R. F. and Mattice, W. L. (1996). Rotational isomeric state models for polyoxyethylene and polythiaethylene on a high coordination lattice. **The Journal of Chemical Physics**. 104: 8742-8749.

Dupon, R., Papke, B. L., Ratner, M. A., Whitmore, D. H. and Shriver, D. F. (1982). Influence of ion pairing on cation transport in the polymer electrolytes formed by poly(ethylene oxide) with sodium tetrafluoroborate and sodium tetrahydroborate. **Journal of the American Chemical Society**. 104: 6247-6251.

Faralli, C., Pagliai, M., Cardini, G. and Schettino, V. (2007). The solvation dynamics of Na^+ and K^+ ions in liquid methanol. **Theoretical Chemistry Accounts: Theory, Computation, and Modeling (Theoretica Chimica Acta)**. 118: 417-423.

Fauteux, D., Prud'Homme, J. and Harvey, P. E. (1988). Electrochemical stability and ionic conductivity of some polymer-lix based electrolytes. **Solid State Ionics**. 28-30: 923-928.

Fenton, D. E., Parker, J. M. and Wright, P. V. (1973). Complexes of alkali metal ions with poly(ethylene oxide). **Polymer**. 14: 589-589.

Ferry, J. D. (1980). **Viscoelastic properties of polymers**. New York: Wiley.

Filipponi, A. and Di Cicco, A. (1995). Short-range order in crystalline, amorphous, liquid, and supercooled germanium probed by x-ray-absorption spectroscopy. **Physical Review B**. 51: 12322.

Flory, P. J. (1988). **The Statistical Mechanics of Chain Molecules**. New York: Hanser.

Frech, R. and Huang, W. (1994). Polymer conformation and ionic association in complexes of lithium, sodium and potassium triflate with poly (ethylene oxide) oligomers. **Solid State Ionics**. 72: 103-107.

Frech, R., Manning, J., Teeters, D. and Black, B. E. (1988). Vibrational spectroscopic study of a low frequency polymer backbone mode in poly(propylene oxide)-sodium thiocyanate complexes. **Solid State Ionics**. 28-30: 954-957.

Fulcher, G. S. (1925). Analysis of recent measurements of the viscosity of glasses. **Journal of the American Ceramic Society**. 8: 339-355.

Fulton, J. L., Heald, S. M., Badyal, Y. S. and Simonson, J. M. (2003). Understanding the effects of concentration on the solvation structure of Ca^{2+} in aqueous solution. I: the perspective on local structure from EXAFS and XANES. **The Journal of Physical Chemistry A**. 107: 4688-4696.

Gabano, F. (1983). **Lithium batteries**. Academic Press, London.

Gibbs, J. H. and DiMarzio, E. A. (1958). Nature of the glass transition and the glassy state. **The Journal of Chemical Physics**. 28: 373-383.

Glezakou, V.-A., Chen, Y., Fulton, J., Schenter, G. and Dang, L. (2006). Electronic structure, statistical mechanical simulations, and EXAFS spectroscopy of aqueous potassium. **Theoretical Chemistry Accounts: Theory, Computation, and Modeling (Theoretica Chimica Acta)**. 115: 86-99.

Goldstein, M. (1973). Viscous liquids and the glass transition. IV. Thermodynamic equations and the transition. **The Journal of Physical Chemistry**. 77: 667-673.

Goodenough, J. B., Hong, H. Y. P. and Kafalas, J. A. (1976). Fast Na^+-ion transport in skeleton structures. **Materials Research Bulletin**. 11: 203-220.

Gorecki, W., Andreani, R., Berthier, C., Armand, M., Mali, M., Roos, J. and Brinkmann, D. (1986). NMR, DSC, and conductivity study of a poly(ethylene oxide) complex electrolyte : PEO(LiClO$_4$)$_x$. **Solid State Ionics**. 18-19: 295-299.

Gray, F. (1991). **Solid Polymer Electrolytes : Fundamentals and Technological Applications** New York: VCH.

Gray, F. M. (1997). **Polymer Electrolytes**. Scotland, UK: The Royal Society of Chemistry.

Greenbaum, S. G., Adamic, K. J., Pak, Y. S., Wintersgill, M. C. and Fontanella, J. J. (1988). NMR, DSC and electrical conductivity studies of MEEP complexed with NaCF$_3$SO$_3$. **Solid State Ionics**. 28-30: 1042-1046.

Grest, G. S. and Cohen, M. H. (1980). Liquid-glass transition: Dependence of the glass transition on heating and cooling rates. **Physical Review B**. 21: 4113.

Guillaume, F. (2005). Combining extended x-ray absorption fine structure with numerical simulations for disordered systems. **Journal of Physics: Condensed Matter**. 17: S145.

Hagenmuller, P. and Gool, W. V. (1978). **Solid electrolytes, general principles, characterization, materials, applications**. Academic Press,New York.

Haile, J. M. (1997). **Molecular dynamics simulation**. John Wiley & Sons, Inc.

Haliloglu, T. and Mattice, W. L. (1998). Mapping of rotational isomeric state chains with asymmetric torsional potential energy functions on a high coordination lattice: Application to polypropylene. **The Journal of Chemical Physics**. 108: 6989-6995.

Hardy, L. C. and Shriver, D. F. (1985). Preparation and electrical response of solid polymer electrolytes with only one mobile species. **Journal of the American Chemical Society**. 107: 3823-3828.

Helfer, C. A., Xu, G., Mattice, W. L. and Pugh, C. (2003). Monte Carlo Simulations Investigating the Threading of Cyclic Poly(ethylene oxide) by Linear Chains in the Melt. **Macromolecules**. 36: 10071-10078.

Himba, T. (1983). Structural aspects of poly(ethylene oxide) salt complexes. **Solid State Ionics**. 9-10: 1101-1105.

Hoffmann, M. M., Darab, J. G., Palmer, B. J. and Fulton, J. L. (1999). A Transition in the Ni^{2+} Complex Structure from Six- to Four-Coordinate upon Formation of Ion Pair Species in Supercritical Water: An X-ray Absorption Fine Structure, Near-Infrared, and Molecular Dynamics Study. **The Journal of Physical Chemistry A**. 103: 8471-8482.

Hyun, J.-K., Dong, H., Rhodes, C. P., Frech, R. and Wheeler, R. A. (2001). Molecular Dynamics Simulations and Spectroscopic Studies of Amorphous Tetraglyme $(CH_3O(CH_2CH_2O)_4CH_3)$ and Tetraglyme:$LiCF_3SO_3$ Structures. **The Journal of Physical Chemistry B**. 105: 3329-3337.

Imberti, S., Botti, A., Bruni, F., Cappa, G., Ricci, M. A. and Soper, A. K. (2005). Ions in water: The microscopic structure of concentrated hydroxide solutions. **The Journal of Chemical Physics**. 122: 194509-194509.

Inomata, K. and Abe, A. (1992). Conformation of 1,2-dimethoxyethane in the gas phase: a rotational isomeric state simulation of NMR vicinal coupling constants. **The Journal of Physical Chemistry**. 96: 7934-7937.

Ito, Y., Kanehori, K., Miyauchi, K. and Kudo, T. (1987). Ionic conductivity of electrolytes formed from PEO-LiCF$_3$SO$_3$ complex low molecular weight poly(ethylene glycol). **Journal of Materials Science**. 22: 1845-1849.

Iwatsuki, S., Kubo, M. and Ohtake, M. (1992). A new polymer electrolyte composed of poly(n-vinylacetamide), poly(ethylene glycol), and lithium trifluoromethanesulfonate. **Chemistry Letters**. 21: 519.

Jaffe, R. L., Smith, G. D. and Yoon, D. Y. (1993). Conformation of 1,2-dimethoxyethane from ab initio electronic structure calculations. **The Journal of Physical Chemistry**. 97: 12745-12751.

Jeffrey, G. A. (1997). **In An Introduction to Hydrogen Bonding**. Oxford University Press: New York.

Johansson, P. **Conformations and Vibrations in Polymer Electrolytes** [On-line]. Available: http://fy.chalmers.se/~patrikj/thesis.htm.

Jones, G. K., McGhie, A. R. and Farrington, G. C. (1991). Studies of the stability of poly(ethylene oxide) and PEO-based solid electrolytes using thermogravimetry-mass spectrometry. **Macromolecules**. 24: 3285-3290.

Kameda, Y., Takahashi, R., Usuki, T. and Uemura, O. (1994). Hydration Structure of SCN− in Concentrated Aqueous Sodium Thiocyanate Solutions. **Bulletin of the Chemical Society of Japan**. 67: 956-963.

Kanbara, T., Inami, M. and Yamamoto, T. (1991). New solid-state electric double-layer capacitor using poly(vinyl alcohol)-based polymer solid electrolyte. **Journal of Power Sources**. 36: 87-93.

Karlsson, G. (2002). **Diffusion in Poly(vinyl alcohol) and polyethylene as determined by computaional simulation and modeling**. Royal Institute of technology, Sweden.

Kelly, I. E., Owen, J. R. and Steele, B. C. H. (1985). Poly(ethylene oxide) electrolytes for operation at near room temperature. **Journal of Power Sources**. 14: 13-21.

Kennedy, J. H., Sahami, S., Shea, S. W. and Zhang, Z. (1986). Preparation and conductivity measurements of SiS_2---Li_2S glasses doped with LiBr and LiCl. **Solid State Ionics**. 18-19: 368-371.

Keski-Rahkomen and Krause, M. O. (1974). **At Data Nucl**. Table, 14: 140.

Killis, A., Le Nest, J. F., Gandini, A. and Cheradame, H. (1984). Ionic conductivity of polyether-polyurethane networks containing alkali metal salts. An analysis of the concentration effect. *Macromolecules*. 17: 63-66.

Killis, A., Le Nest, J. F., Gandini, A., Cheradame, H. and Cohen-Addad, J. P. (1984). Correlation among transport properties in ionically conducting cross-linked networks. **Solid State Ionics**. 14: 231-237.

Kotelyanskii, M. and Theodorou, D. N. (2004). **Simulation methods for polymers**. New York: Marcel Dekker.

Latham, R. J., Linford, R. G., Pynenburg, R. A. J., Schlindwein, W. S. and Farrington, G. C. (1993). Plasticiser-induced local structure in polymer electrolytes. **Journal of the Chemical Society, Faraday Transactions**. 89: 349-354.

Latham, R. J., Linford, R. G. and Schlindwein, W. S. (1989). Cation-oxygen geometry in polymer electrolytes: interpretation of EXAFS results. **Faraday Discussions of the Chemical Society**. 88: 103-111.

Le Nest, J. F., Gandini, A., Cheradame, H. and Cohen-Addad, J. P. (1988). Influence of lithium perchlorate on the properties of polyether networks: specific volume and glass transition temperature. **Macromolecules**. 21: 1117-1120.

Lee, Y. L. and Crist, B. (1986). Phase behavior and conductivity in poly(ethylene oxide)--sodium thiocyanate systems. **Journal of Applied Physics**. 60: 2683-2689.

Lennard-Jones, J. E. (1931). Cohesion. **Proceedings of the Physical Society**. 43: 461.

Lightfoot, P., Mehta, M. A. and Bruce, P. G. (1992). Structure of the poly(ethylene oxide)-sodium perchlorate complex PEO_3-$NaClO_4$ from powder X-ray diffraction data. **Journal of Materials Chemistry**. 2: 379-381.

Lightfoot, P., Mehta, M. A. and Bruce, P. G. (1993). Crystal Structure of the Polymer Electrolyte Poly(ethylene oxide)$_3$:$LiCF_3SO_3$. **Science**. 262: 883-885.

Lightfoot, P., Nowinski, J. L. and Bruce, P. G. (1994). Crystal Structures of the Polymer Electrolytes Poly(ethylene oxide)$_4$:MSCN (M = NH_4, K). **Journal of the American Chemical Society**. 116: 7469-7470.

Lin, H., Mattice, W. L. and Von Meerwall, E. D. (2006). Dynamics of polyethylene melts studied by Monte Carlo simulations on a high coordination lattice. **Journal of Polymer Science Part B: Polymer Physics**. 44: 2556-2571.

Linford, R. G. (1995). EXAFS studies of polymer electrolytes. **Chemical Society Reviews**. 24: 267-277.

Londono, J. D., Annis, B. K., Habenschuss, A., Borodin, O., Smith, G. D., Turner, J. Z. and Soper, A. K. (1997). Cation Environment in Molten Lithium Iodide Doped Poly(ethylene oxide). **Macromolecules**. 30: 7151-7157.

MacCallum, J. and Vincent, C. (1987). **Polymer electrolyte reviews-I**. Elsevier Applied Science, New York.

MacCallum, J. and Vincent, C. (1989). **Polymer electrolyte reviews-II**. Elsevier Applied Science, New York.

MacDonald, J. R. (1973). Theory of space-charge polarization and electrode-discharge effects. **The Journal of Chemical Physics**. 58: 4982-5001.

Marcus, Y. (1988). Ionic radii in aqueous solutions. **Chemical Reviews**. 88: 1475-1498.

Mason, P. E., Neilson, G. W., Dempsey, C. E., Barnes, A. C. and Cruickshank, J. M. (2003). The hydration structure of guanidinium and thiocyanate ions: Implications for protein stability in aqueous solution. **Proceedings of the National Academy of Sciences of the United States of America**. 100: 4557-4561.

Mathiowetz, A. M. (1994). Dynamic and Stochastic Protein Simulations. [On-line]. Available: http://www.wag.caltech.edu/publications/theses/alan/thesis.html.

Mattice, W. L., Helfer, C. A. and Sokolov, A. P. (2004). Persistence Length and Finite Chain Length Effect on Characteristic Ratios. **Macromolecules**. 37: 4711-4717.

Mattice, W. L. and Suter, U. W. (1994). **Conformational theory of large molecules: The rotational isomeric state model in macromolecular systems**. New York: Wiley.

Mendolia, M. S., Farrington, G. C. (1995). **High-Conductivity, Solid Polymeric Electrolytes. Materials Chemistry: An Emerging Discipline (108)**. American Chemical Society.

Mercier, R., Malugani, J.-P., Fahys, B. and Robert, G. (1981). Superionic conduction in Li2S - P2S5 - LiI - glasses. **Solid State Ionics**. 5: 663-666.

Merkling, P. J., Ayala, R., Martinez, J. M., Pappalardo, R. R. and Marcos, E. S. (2003). Interplay of computer simulations and x-ray absorption spectra in the study of the bromide hydration structure. **The Journal of Chemical Physics**. 119: 6647-6654.

Metropolis, N., Rosenbluth, A. W., Rosenbluth, M. N., Teller, A. H. and Teller, E. (1953). Equation of State Calculations by Fast Computing Machines. **The Journal of Chemical Physics**. 21: 1087-1092.

Mohamad, A. A., Mohamed, N. S., Yahya, M. Z. A., Othman, R., Ramesh, S., Alias, Y. and Arof, A. K. (2003). Ionic conductivity studies of poly(vinyl alcohol) alkaline solid polymer electrolyte and its use in nickel-zinc cells. **Solid State Ionics**. 156: 171-177.

Moon, S. D., Kang, Y. S. and Lee, D. J. (2007). Monte Carlo Simulation of the Molecular Properties of Poly(vinyl chloride) and Poly(vinyl alcohol) Melts. **Macromolecular Research**. 15: 491-497.

Newville, M., Ravel, B., Haskel, D., Rehr, J. J., Stern, E. A. and Yacoby, Y. (1995). Analysis of multiple-scattering XAFS data using theoretical standards. **Physica B: Condensed Matter**. 208-209: 154-156.

Ngai, K. L. and Skolnick, J. (1991). Correspondence between the Coupling Model Predictions and Computer Simulations: Diffusion of a Prob Polymer in a matrix Having Different Degree of Polymerization. **Macromolecules**. 24: 1561.

Nicholson, P., Whittingham, M., Farrington, G., Smeltzer, W. W. and Thomas, J. (1992). **Solid State Ionics-91**. North-Holland, Amsterdam.

Oláh, J., Alsenoy, C. V. and Veszprémi, T. (2004). NaSCN: Striking Differences between Its Gas-Phase and Crystal-Phase Structure: A Theoretical Study. **The Journal of Physical Chemistry A**. 108: 8400-8406.

Orwoll, R. A. (1996). **In physical properties of polymers handbook**. Mark, J.E ed., Woodbury:American Institute of Physics.

Owens, B. B. and Argue, G. R. (1967). High-Conductivity Solid Electrolytes: MAg4I5., **Science**. 157: 308-310.

Palmer, B. J., Pfund, D. M. and Fulton, J. L. (1996). Direct Modeling of EXAFS Spectra from Molecular Dynamics Simulations. **The Journal of Physical Chemistry**. 100: 13393-13398.

Papke, B. L., Ratner, M. A. and Shriver, D. F. (1981). Vibrational spectroscopy and structure of polymer electrolytes, poly(ethylene oxide) complexes of alkali metal salts. **Journal of Physics and Chemistry of Solids**. 42: 493-500.

Papke, B. L., Ratner, M. A. and Shriver, D. F. (1982a). Vibrational Spectroscopic Determination of Structure and Ion Pairing in Complexes of Poly(ethylene oxide) with Lithium Salts. **Journal of The Electrochemical Society**. 129: 1434-1438.

Papke, B. L., Ratner, M. A. and Shriver, D. F. (1982b). Conformation and Ion-Transport Models for the Structure and Ionic Conductivity in Complexes of Polyethers with Alkali Metal Salts. **Journal of The Electrochemical Society**. 129: 1694-1701.

Parker, J. M., Wright, P. V. and Lee, C. C. (1981). A double helical model for some alkali metal ion-poly(ethylene oxide) complexes. **Polymer**. 22: 1305-1307.

Preechatiwong, W. and Schultz, J. M. (1996). Electrical conductivity of poly(ethylene oxide)--alkali metal salt systems and effects of mixed salts and mixed molecular weights. **Polymer**. 37: 5109-5116.

Quartarone, E., Mustarelli, P. and Magistris, A. (1998). PEO-based composite polymer electrolytes. **Solid State Ionics**. 110: 1-14.

Rapaport, D. C. (1995). **The art of molecular dynamics simulation**. Cambridge University Press.

Rapold, R. F. and Mattice, W. L. (1995). New high-coordination lattice model for rotational isomeric state polymer chains. **Journal of the Chemical Society, Faraday Transactions**. 91: 2435-2441.

Ratner, M. A. and Shriver, D. F. (1988). Ion transport in solvent-free polymers. **Chemical Reviews**. 88: 109-124.

Ravel, B. and Newville, M. (2005). ATHENA, ARTEMIS, HEPHAESTUS: data analysis for X-ray absorption spectroscopy using IFEFFIT. **Journal of Synchrotron Radiation**. 12: 537-541.

Rehr, J. J. and Albers, R. C. (2000). Theoretical approaches to x-ray absorption fine structure. **Reviews of Modern Physics**. 72: 621.

Rempe, S. B., Asthagiri, D. and Pratt, L. R. (2004). Inner shell definition and absolute hydration free energy of $K^+_{(aq)}$ on the basis of quasi-chemical theory and ab initio molecular dynamics. **Physical Chemistry Chemical Physics**. 6: 1966-1969.

Rhodes, C. P. and Frech, R. (1999). Cation-anion and cation-polymer interactions in (PEO)$_n$NaCF$_3$SO$_3$ (n=1-80). **Solid State Ionics**. 121: 91-99.

Rhodes, C. P. and Frech, R. (2001). Vibrational Study of the Polymer Electrolyte Poly(ethylene oxide)$_6$:LiAsF$_6$. **Macromolecules**. 34: 1365-1368.

Rickert, H. (1978). Solid Ionic Conductors: Principles and Applications. **Angewandte Chemie International Edition in English**. 17: 37-46.

Robitaille, C., Marques, S., Boils, D. and Prud'homme, J. (1987). Thermal properties of poly(ethylene oxide) complexed with sodium thiocyanate and potassium thiocyanate. **Macromolecules**. 20: 3023-3034.

Robitaille, C. and Prud'homme, J. (1983). Thermal and mechanical properties of a poly(ethylene oxide-b-isoprene-b-ethylene oxide) block polymer complexed with sodium thiocyanate. **Macromolecules**. 16: 665-671.

Robitaille, C. D. and Fauteux, D. (1986). Phase Diagrams and Conductivity Characterization of Some PEO-LiX Electrolytes. **Journal of The Electrochemical Society**. 133: 315-325.

Roccatano, D., Berendsen, H. J. C. and D'Angelo, P. (1998). Assessment of the validity of intermolecular potential models used in molecular dynamics simulations by extended x-ray absorption fine structure spectroscopy: A case study of Sr^{2+} in methanol solution. **The Journal of Chemical Physics**. 108: 9487-9497.

Rossinsky, E., Tarmyshov, K. B., Böhm, M. C. and Müller-Plathe, F. (2009). Properties of Polyvinyl Alcohol Oligomers: A Molecular Dynamics Study. **Macromolecular Theory and Simulations**. 18: 545-552.

Sato, H., Kusumoto, Y. (1978). Highly symmetric structure of alkali metal complexes of 18-crown-6 and 15-crown-5 in liquid and crystalline states as revealed by raman spectra., **Chemistry Letter**. 635-638.

Schantz, S., Sandahl, J., Börjesson, L., Torell, L. M. and Stevens, J. R. (1988). Ion pairing in polymer electrolytes; A comparative Raman study of $NaCF_3SO_3$ complexed in poly(propylene-glycol) and dissolved in acetonitrile. **Solid State Ionics**. 28-30: 1047-1053.

Schantz, S. and Torell, L. M. (1993). Evidence of dissolved ions and ion pairs in dilute poly (propylene oxide)-salt solutions. **Solid State Ionics**. 60: 47-53.

Schlindwein, W., Pynenburg, R., Latham, R. and Linford, R. (1995). EXAFS studies on cobalt polymer electrolytes. **Nuclear Instruments and Methods in Physics Research Section B: Beam Interactions with Materials and Atoms**. 97: 292-294.

Scrosati, B. (1993). **Applications of Electroactive Polymers**. Chapman and Hall, London.

Sheldon, M. H., Glasse, M. D., Latham, R. J. and Linford, R. G. (1989). The effect of plasticiser on zinc polymer electrolytes. **Solid State Ionics**. 34: 135-138.

Smith, R. P. (1964). Excluded Volume Effect in Polymer Chains. II. Properties of Restricted Chains on a Diamond Lattice. **The Journal of Chemical Physics**. 40: 2693-2699.

Song, J. Y., Wang, Y. Y. and Wan, C. C. (1999). Review of gel-type polymer electrolytes for lithium-ion batteries. **Journal of Power Sources**. 77: 183-197.

Spindler, R. and Shriver, D. F. (1986). Physical and spectroscopic properties of ternary polymer electrolytes composed of poly(vinylpyrrolidinone), polyethylene glycol, and lithium trifluoromethanesulfonate. **Macromolecules**. 19: 347-350.

Spindler, R. and Shriver, D. F. (1988). Investigations of a siloxane-based polymer electrolyte employing carbon-13, silicon-29, lithium-7, and sodium-23 solid-state NMR spectroscopy. **Journal of the American Chemical Society**. 110: 3036-3043.

Stainer, M., Hardy, L. C., Whitmore, D. H. and Shriver, D. F. (1984). Stoichiometry of Formation and Conductivity Response of Amorphous and Crystalline Complexes Formed Between Poly(ethylene oxide) and Ammonium Salts:$PEO_x.NH_4SCN$ and $PEO_x.NH_4SO_3CF_3$. **Journal of The Electrochemical Society**. 131: 784-790.

Suthanthiraraj, S., Kumar, R. and Paul, B. (2010). Vibrational spectroscopic and electrochemical characteristics of poly (propylene glycol)-silver triflate polymer electrolyte system. **Ionics**. 16: 145-151.

Takahashi, T., Ikeda, S. and Yamamoto, O. (1972). Solid-State Ionics---Solids with High Ionic Conductivity in the Systems Silver Iodide-Silver Oxyacid Salts. **Journal of The Electrochemical Society**. 119: 477-482.

Takeoka, S., Horiuchi, K., Yamagata, S. and Tsuchida, E. (1991). Sodium ion conduction of perfluorosulfonate ionomer/poly(oxyethylene) composite films. **Macromolecules**. 24: 2003-2006.

Tao, P. (1997). **An Introducion to computational physics**. Cambridge: Cambridge University Press.

Tatsumisago, M., Shinkuma, Y. and Minami, T. (1991). Stabilization of superionic [alpha]-Agl at room temperature in a glass matrix. **Nature**. 354: 217-218.

Teeters, D. and Frech, R. (1986). Temperature-dependent spectroscopic studies of poly(propylene oxide) and poly(propylene oxide)-inorganic salt complexes. **Solid State Ionics**. 18-19: 271-276.

Thorpe, M. F. and Schroll, W. K. (1981). Statistics of polymer chains embedded on a diamond lattice. I. Exact results for the lattice version of the freely rotating chain. **The Journal of Chemical Physics**. 75: 5143-5148.

v. Alpen, U., Rabenau, A. and Talat, G. H. (1977). Ionic conductivity in Li_3N single crystals. **Applied Physics Letters**. 30: 621-623.

Vargas, R. A., Zapata, V. H., Matallana, E. and Vargas, M. A. (2001). More thermal studies on the $PVOH/H_3PO_2/H_2O$ solid proton conductor gels. **Electrochimica Acta**. 46: 1699-1702.

Vashishta, P., Mundy, J. N., Shenoy, G. K., (eds) (1979). **Fast ion transport in solids.** Elsevier Applied Science, North Holland, New York.

Verdier, P. H. and Stockmayer, W. H. (1962). Monte Carlo Calculations on the Dynamics of Polymers in Dilute Solution. **The Journal of Chemical Physics**. 36: 227-235.

Vincent, C., Bonino, F., Lazzari, M. and Scrosati, B. (1983). **Modern batteries**. Edward Arnold, London.

Vincze, Á., Jedlovszky, P. and Horvai, G. (2001). The L/L interface and adsorption of SCN^- anions as studied by different molecular simulation techniques. **Analytical Sciences**. 17: i317.

Visco, S. J., Liu, M., Doeff, M. M., Ma, Y. P., Lampert, C. and De Jonghe, L. C. (1993). Polyorganodisulfide electrodes for solid-state batteries and electrochromic devices. **Solid State Ionics**. 60: 175-187.

Wada, H., Menetrier, M., Levasseur, A. and Hagenmuller, P. (1983). Preparation and ionic conductivity of new B_2S_3-Li_2S-LiI glasses. **Materials Research Bulletin**. 18: 189-193.

Watanabe, M., Itoh, M., Sanui, K. and Ogata, N. (1987). Carrier transport and generation processes in polymer electrolytes based on poly(ethylene oxide) networks. **Macromolecules**. 20: 569-573.

Watanabe, M., Nagano, S., Sanui, K. and Ogata, N. (1986). Ion conduction mechanism in network polymers from poly(ethylene oxide) and poly(propylene oxide) containing lithium perchlorate. **Solid State Ionics**. 18-19: 338-342.

Watanabe, M., Oohashi, S., Sanui, K., Ogata, N., Kobayashi, T. and Ohtaki, Z. (1985). Morphology and ionic conductivity of polymer complexes formed by segmented polyether poly(urethane urea) and lithium perchlorate. **Macromolecules**. 18: 1945-1950.

Whittingham, M. S. and Huggins, R. A. (1971). Measurement of Sodium Ion Transport in Beta Alumina Using Reversible Solid Electrodes. **The Journal of Chemical Physics**. 54: 414-416.

Wikipedia (2008). **Molecular Dynamics** [On-line]. Available: http://en.wikipedia.org/wiki/Molecular_dynamics.

Wolf, R. M. and Suter, U. W. (1984). Conformational characteristics of poly(vinyl alcohol). **Macromolecules**. 17: 669-677.

Wright, P. V. (1976). An anomalous transition to a lower activation energy for dc electrical conduction above the glass-transition temperature. **Journal of Polymer Science: Polymer Physics Edition**. 14: 955-957.

Xia, D. W., Soltz, D. and Smid, J. (1984). Conductivities of solid polymer electrolyte complexes of alkali salts with polymers of methoxypolyethyleneglycol methacrylates. **Solid State Ionics**. 14: 221-224.

Xu, M., Eyring, E. M. and Petrucci, S. (1996). Anion solvation effects in polymer-electrolytes: NaSCN and LiSCN in PEO-400 and in PEG-400. **Solid State Ionics**. 83: 293-300.

Yang, C.-C. (2004). Chemical composition and XRD analyses for alkaline composite PVA polymer electrolyte. **Materials Letters**. 58: 33-38.

Zhang, H. and Wang, J. (2009). Vibrational spectroscopic study of ionic association in poly(ethylene oxide)-NH$_4$SCN polymer electrolytes. **Spectrochimica Acta Part A: Molecular and Biomolecular Spectroscopy**. 71: 1927-1931.

Zhang, H., Xuan, X., Wang, J. and Wang, H. (2003). FT-IR investigations of ion association in PEO-MSCN (M=Na, K) polymer electrolytes. **Solid State Ionics**. 164: 73-79.

APPENDICES

MONTE CARLO SIMULATION STUDIES OF STATICS AND DYNAMICS OF BIDISPERSE POLYETHYLENE OXIDE MODELS

Jittima Chaodamrongsakul[1-2], Wantana Klysuban[3], Visit Vao-soongnern[1-2]∗

[1]Laboratory of Computational and Applied Polymer Science (LCAPS). [2]School of Chemistry, Institute of Science, Suranaree University of Technology, [3]Synchrotron Light Research Institute (Public Organization),Nakhon Ratchasima, Thailand.

A new Monte Carlo (MC) simulations for dense melts of coarse-grained polymers on a high-coordination lattice has been developed for predicting static and dynamics properties of mono- and bi-disperse poly(ethylene oxide) (PEO). This work presents a recently developed strategy that has used a method where an atomistic chain is mapped onto a coarse-grained model. Polyethylene oxide (PEO) model which each bead represents series of linked vectors connecting the CH_2CH_2 and CH_2O units was constructed. Both short-range interactions based on the rotational isomeric state model and long-range interactions from a discretized form of the Lennard-Jones (LJ) potential energy function are included. The simulations were performed at 373 K for bidisperse (1.4K/8.7K) PEO melt in the Rouse regime (unentangled). The equilibration of the system is considered to be satisfied when the mean square displacement (MSD) of the center of mass is higher than mean-square radius of gyration ($\langle s^2 \rangle$) and the orientation autocorrelation function for the end-to-end vector (OACF) decays to values close to zero. The internal relaxation modes fit the KWW relationship very well. There is no systematic change of $\langle s^2 \rangle$ as the concentration varies in the mixture. Thus, the mixture can be regarded as the Θ solution of each species. For the long-chain component in the mixture, the tube dilation concept has been visualized through the short-time diffusion of monomers at different concentration.
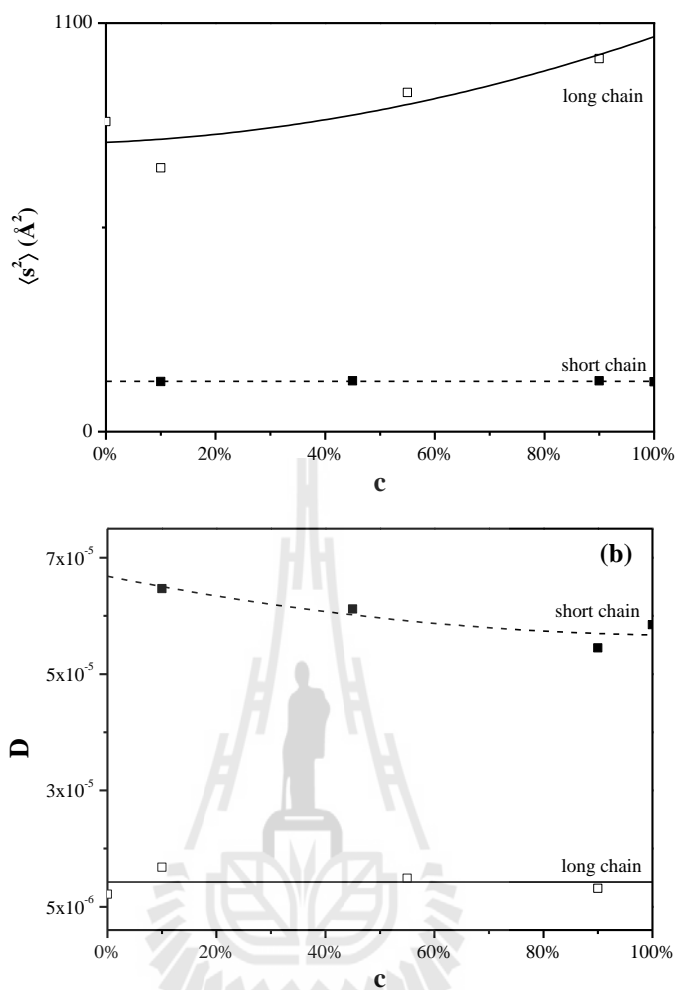
Figure 1 (a) Mean-square radius of gyration $\langle s^2 \rangle$ and (b) diffusion coefficient D of long chain (8.7K) and short chain (1.4K) components in the mixture against the weight concentration of the short chain.

The Asian Consortium on Computational Materials Science
(ACCMS-5) 9-11 September 2009

Molecular Dynamic Simulation and Extended X-Ray Absorption Fine Structure (EXAFS) Spectroscopy Studies of Cation Local Structure of Tetraglyme/Potassium Thiocyanate Electrolytes

J. Chaodamrongsakul[1], W. Klysubun[2], V. Vao-soongnern[1]

[1] Laboratory of Computational and Applied Polymer Science (LCAPS),

School of Chemistry, Institute of Science, Suranaree University of Technology

[2] Synchrotron Light Research Institute (Public Organization), Nakhon Ratchasima, Thailand,

Tel: +66-044-224187, E-mail address: visit@sut.ac.th

Solid polymer electrolytes (SPEs) are of great interest in the context of developing a variety of modern electrochemical applications. The wide range of technological applications of SPEs has spurred attempts to understand the mechanism of ionic transport in polymer electrolytes. The local structures around the potassium species of tetraglyme [$CH_3O(CH_2CH_2O)_4CH_3$, a 4-mers model compound for poly(ethylene oxide)] were characterized using a combination of Extended X-Ray Absorption Fine Structure (EXAFS), acquired on BL-8 at Synchrotron Light Research Institute (Public Organization), and Molecular Dynamic (MD) simulation which give information such as coordination number and distance of neighbours around potassium ion (K^+). Radial distribution functions (RDFs) between K^+ and all tetraglyme atoms (O, C, H) were determined. Each K^+ is coordinated by ~2.6 oxygens (K^+-O distance ≤ 4.05 Å), ~1.5 sulfurs (K^+-S ≤ 3.55 Å), and ~1.5 nitrogens (K^+-N ≤ 3.65 Å).

References

1. Chintapalli S. And Frech R. *Polymer* **1997**, 38, 6189.
2. Dang L. X. *et al. J. Phys. Chem. B*. **2006**, 110, 23644.
3. Glezakou V.-A. *et al. Theor. Chem. Acc.* **2006**, 115, 86.

Preferred type of talk (Oral, Poster): **Oral**

Preferred conference session: **Session: 13 Modelling of materials for future energy**

การประยุกต์ใช้การดูดกลืนรังสีเอ็กซ์และการจำลองแบบโมเลกุลาร์ไดนามิกส์เพื่อศึกษาโครงสร้าง

ระดับอะตอมและการเคลื่อนที่ของไอออน ระบบ Tetraglyme/KSCN อิเล็กโทรไลต์

**APPLICATION OF X-RAY ABSORPTION SPECTROSCOPY AND
MOLECULAR DYNAMIC SIMULATION TO STUDY THE ATOMISTIC
NANOSTRUCTURE AND IONIC MOBILITY OF TETRAGLYME/KSCN
SOLID ELECTROLYTES**

<u>จิตติมา เชาว์ดำรงสกุล</u>[1,2], วันทนา คล้ายสุบรรณ์[3], วิสิษฐ์ แววสูงเนิน[1,2]*

<u>**Jittima Chaodamrongsakul**</u>**[1,2], Wantana Klysubun[3], Visit Vao-soongnern[1,2]***

Laboratory of Computational and Applied Polymer Science (LCAPS)[1],
School of Chemistry[2], Institute of Science, Suranaree University of Technology,
National Synchrotron Research Center[3], Nakhon Ratchasima, Thailand

E-mail: visit@sut.ac.th, Phone: 04-4224-637, Fax: 04-4224-185

บทคัดย่อ: พอลิเมอร์อิเล็กโทรไลต์ชนิดแข็งกำลังเป็นที่น่าสนใจในการพัฒนาเป็นวัสดุเก็บพลังงานชนิดใหม่ โดยปกติแล้ว SPEs ประกอบด้วยเกลือ (KSCN) ซึ่งทำหน้าที่เป็นไอออนที่เคลื่อนไหวได้และพอลิเมอร์ซึ่งทำหน้าที่เป็นตัวทำละลาย เนื่องจากข้อจำกัดในการนำไฟฟ้าที่อุณหภูมิห้องของพอลิเมอร์อิเล็กโทรไลต์ ทำให้มีความจำเป็นอย่างยิ่งที่จะต้องทำความเข้าใจเกี่ยวกับกลไกการนำไฟฟ้าในวัสดุ SPEs งานวิจัยนี้ได้ทำการศึกษาโครงสร้างล้อมรอบไอออนโพแทสเซียมใน tetraglyme [CH$_3$O(CH$_2$CH$_2$O)$_4$CH$_3$ (Tetraethylene glycol dimethyl ether) เป็นโมเดลเริ่มต้นในการศึกษาสำหรับพอลิเอธิลีนออกไซด์] ด้วยเทคนิค EXAFS และการจำลองโมเลกูลาร์ไดนามิกส์ (MD) ซึ่งได้ข้อมูลเกี่ยวกับเลขโคออร์ดิเนชันและระยะห่างระหว่างโพแทสเซียมไอออนกับอะตอมข้างเคียง นอกจากนี้ข้อมูลที่ได้จากทั้งสองเทคนิคสามารถนำมาใช้อธิบายการเปลี่ยนแปลงค่าการนำไฟฟ้าที่เกิดขึ้นต่ออัตราส่วน O:K$^+$ ที่เปลี่ยนแปลงไป และใช้อธิบายกลไกการเคลื่อนที่ที่เป็นไปได้ของไอออน จากการวิเคราะห์ Radial distribution functions (RDFs) ระหว่าง K$^+$ และอะตอมข้างเคียงพบว่า K$^+$ ล้อมรอบด้วย ~2.6 ออกซิเจนอะตอม ~1.5 ซัลเฟอร์อะตอม และ~1.5 ไนโตรเจนอะตอม นอกจากนี้ได้ทำการหาไอออนในระยะ 6 Å ที่ล้อมรอบ K$^+$ เพื่อใช้เป็นข้อมูลสำหรับโปรแกรม FEFF6 และคำนวณสเปกตรัม EXAFS เพื่อใช้เปรียบเทียบกับสเปกตรัม EXAFS ที่ได้จากการทดลอง

Abstract: Solid polymer electrolytes (SPEs) are of great interest in the context of developing a variety of modern energy storage materials. Conventionally, SPEs consist of a salt (KSCN) and polymer host. The KSCN salt supplies mobile ions and polymer plays a role of solvent. The limited room temperature conductivity polymer electrolytes are still a barrier in many applications. Therefore, it is indispensable for understanding of the ion conduction mechanism in such SPEs. The local structures around the potassium species of tetraglyme [CH$_3$O(CH$_2$CH$_2$O)$_4$CH$_3$ (Tetraethylene

glycol dimethyl ether), a 4-mers model compound for poly(ethylene oxide)] were characterized using a combination of Extended X-Ray Absorption Fine Structure (EXAFS), acquired on BL-8 at Synchrotron Light Research Institute (Public Organization), and Molecular Dynamic (MD) simulation which give information such as coordination number and distance of neighbors around potassium ion (K^+) In additionally, provide more understanding for an explanation of the change in ionic conductivity as a function of $O:K^+$ ratio and a possible mechanism of ion movement of these SPE materials. Radial distribution functions (RDFs) between K^+ and neighbors atoms (O, C, H, S, N) were determined. Each K^+ is coordinated by ~2.6 oxygens (K^+-O distance ≤ 4.05 Å), ~1.5 sulfurs (K^+-S ≤ 3.55 Å), and ~1.5 nitrogens (K^+-N ≤ 3.65 Å). Furthermore, for each configuration taken from the trajectory, a cluster was obtained by extracting all species that fell within 6 Å radius of the K^+ ion. The cluster was then used as an input to the program FEFF6, which calculates the EXAFS spectrum $\mu(E)$ for the K^+ ion and then the average spectrum, was compared to the EXAFS spectrum.

Asian Conference on Electrochemical Power Sources 5 (ACEPS-5)
17-20 September 2010

Molecular Simulation Analysis and X-Ray Absorption Measurement of K^{+} Ion in Aqueous Solution and Poly(Vinyl Alcohol) Based Polymer Electrolytes

J. Chaodamrongsakul[a], W. Klysubun[b], V. Vao-soongnern[a]
[a] Laboratory of Computational and Applied Polymer Science (LCAPS),
School of Chemistry, Institute of Science, Suranaree University of Technology
[b] Synchrotron Light Research Institute (Public Organization), Nakhon Ratchasima, Thailand
Corresponding Author: jittima_chao@hotmail.com, Tel: +66 4422 4187

Molecular Dynamic (MD) simulation and Extended X-ray Absorption Fine Structure (EXAFS) spectroscopy were combined to determine the solvation structures of K^+/H_2O and K^+/PVA systems. The local structures of K^+/H_2O was studied as the first step toward understanding more complicated K^+/PVA system. The radial distribution functions (RDFs) calculated from MD simulations by using COMPASS forcefield at 300 K provided the structural parameters: the distance between K^+ and water molecules (K^+-O and K^+-H) as well as the coordination numbers (N_O and N_H are the numbers of oxygen atoms and hydrogen atoms, respectively). For the K^+/H_2O system, the average K^+-O and K^+-H distance and N_O and N_H for the first coordination shell are 2.65 Å, 3.31 Å, 5.7 and 17.6, respectively. In this work, 50 independent configurations from MD simulations were selected to generate the MD-EXAFS spectra which were found to be in very good agreement with the EXAFS spectra obtained from experiment. However, it should be noted that hydrogen atoms can affected on the MD-EXAFS signals. Excluding all hydrogen atoms in the calculation for the K^+/H_2O system gave the better MD-EXAFS spectra as compare to the experimental one. As mention above can be confirm that MD simulation is the useful technique to study local solvation structures of K^+/H_2O. In this work MD simulation also employed to study the complicated K^+/PVA system to explain the local solvation structure of PVA unit around K^+ ion. The RDFs showed that the first solvation around K^+ is the oxygen atoms from PVA with the average K^+-O distance and N_O are 2.55 Å and 4.9, respectively. The comparison between MD-EXAFS (excluded all hydrogen in PVA structure) and EXAFS spectra obtained from experiment showed overall agree well for both the frequency and the amplitude of the oscillations over the full k range from 2 to 7 Å. The matching of the frequency of the oscillations means that the K^+-O distances are nearly the same between the experiment and the simulation. However, the EXAFS spectra obtained from the experiment showed the broader peak compared to the MD-EXAFS spectra due to the higher orderity in the simulation system.

CURRICULUM VITAE

JITTIMA CHAODAMRONGSAKUL

Born: March 14, 1978, Nakhon Ratchasima

Citizenship: Thailand

Education

1996-1999   B.Sc. Chemistry

             Burapha University, Chonburi, Thailand

2000-2003   M.Sc. Chemistry

             Suranaree University of Technology, Nakhon Ratchasima, Thailand

Presentation

1. Oral presentation at Fourth International Workshop for Far East Asian Young Rheologists (IWFEAYR-4), 21-23 January 2009, Suranaree University of Technology, Thailand.

2. Poster presentation at Asian Consortium on Computational Materials Science (ACCMS-5), 9-11 September 2009, Hanoi, Vietnam.

3. Poster presentation at 5th Asia Conference on Electrochemical Power Sources" (ACEPS-5), 17-20 September 2010, National University of Singapore, Singapore.